1-10-2024

INTEGRATED COMPUTER-AIDED DESIGN, EXPERIMENTATION, AND OPTIMIZATION APPROACH FOR PEROVSKITES AND PETROLEUM PACKAGING PROCESSES

Swapana Subbarao Jerpoth
Rowan University

INTEGRATED COMPUTER-AIDED DESIGN EXPERIMENTATION, AND OPTIMIZATION APPROACH FOR PEROVSKITES AND PETROLEUM PACKAGING PROCESSES

by

Swapana S. Jerpoth

A Dissertation

Submitted to the
Department of Chemical Engineering
College of Engineering
In partial fulfillment of the requirement
For the degree of
Doctor of Philosophy
at
Rowan University
September 29, 2023

Dissertation Chair: Kirti M. Yenkie, Ph.D., Associate Professor, Department of Chemical Engineering, Rowan University
Dissertation Co-Chair: Robert P. Hesketh, Ph.D., Professor, Department of Chemical Engineering, Rowan University

Committee Members:
C. Stewart Slater, Ph.D., Professor Emeritus and Founding Chair, Department of Chemical Engineering, Rowan University
Mariano J. Savelski, Ph.D., Professor, Department of Chemical Engineering and Vice Provost for Faculty Affairs, Rowan University
Wenzhao Wu, Ph.D., Researcher, ExxonMobil USA

Dedications

I dedicate this work to my parents, Subbarao and Anupama Jerpoth, and my brother, Venkatesh Jerpoth, whose firm support has been my pillar throughout my academic journey. A special dedication to Raj Kashala for consistently encouraging and supporting my dreams.

Acknowledgments

I want to express my sincerest gratitude to my advisor, Dr. Kirti M. Yenkie and my co-advisor Dr. Robert P. Hesketh for their immense support and guidance throughout my studies. I would like to thank Dr. C. Stewart Slater, Dr. Mariano J. Savelski, and Dr. Wenzhao Wu, for serving on my dissertation committee. A special thank you to my fellow graduate students: Emmanuel Aboagye, Fred Ghanem, Austin Lehr, Jake Stengel and Barnabas Gao, for their invaluable input during my time as a Ph.D. student. A heartfelt thank you to my undergraduate students Sean Curtis, David Theuma, Michael Fracchiolla, Steven Roth, Jacob Martin, and Marissa Martine for a mutually enriching learning experience through our collaborative efforts in engineering clinics. I would like to express my gratitude to the U.S Environmental Protection Agency, specifically the Pollution Prevention Grant Program, for their financial support in this project. I also deeply appreciate the ongoing support and valuable feedback from our industrial collaborators. A big thank you to Association for Women in Science Philadelphia Chapter (AWIS-PHL) and National Science Foundation (NSF) for generously supporting my conference travels to American Institute of Chemical Engineers (AIChE) Annual Meeting, 2022 and Foundations of Process/Product Analytics and Machine Learning (FOPAM), 2023. I extend my heartfelt thanks to Society of Tribologists and Lubrication Engineers (STLE) for choosing me as a recipient of the 2022 scholarship award.

Abstract

Swapana Subbarao Jerpoth
INTEGRATED COMPUTER-AIDED DESIGN, EXPERIMENTATION AND OPTIMIZATION APPROACH FOR PEROVSKITES AND PETROLEUM PACKAGING PROCESSES
2023-2024
Kirti M. Yenkie, PhD.
Robert P. Hesketh, Ph.D.
Doctor of Philosophy in Chemical Engineering

According to the World Economic Forum report, the U.S. currently has an energy efficiency of just 30%, thus illustrating the potential scope and need for efficiency enhancement and waste minimization. In the U.S. energy sector, petroleum and solar energy are the two key pillars that have the potential to create research opportunities for transition to a cleaner, greener, and sustainable future. In this research endeavor, the focus is on two pivotal areas: (i) Computer-aided perovskite solar cell synthesis; and (ii) Optimization of flow processes through multiproduct petroleum pipelines. In the area of perovskite synthesis, the emphasis is on the enhancement of structural stability, lower costs, and sustainability. Utilizing modeling and optimization methods for computer-aided molecular design (CAMD), efficient, sustainable, less toxic, and economically viable alternatives to conventional lead-based perovskites are obtained.

In the second area of optimization of flow processes through multiproduct petroleum pipelines, an actual industrial-scale operation for packaging multiple lube-oil blends is studied. Through an integrated approach of experimental characterization, process design, procedural improvements, testing protocols, control mechanisms, mathematical modeling, and optimization, the limitations of traditional packaging operations are identified, and innovative operational paradigms and strategies are developed by incorporating methods from process systems engineering and data-driven approaches.

Table of Contents

Table of Contents (Continued)

Table of Contents (Continued)

Table of Contents (Continued)

List of Figures

List of Figures (Continued)

Figure Page

List of Figures (Continued)

Figure Page

List of Figures (Continued)

Figure Page

List of Tables

Table Page

Chapter 1

Introduction

1.1 Motivation

The resources on our planet, necessary to maintain our present rate of consumption, are not infinite or even plentiful enough to last through several generations [1], [2]. The products and processes that allow our modern lifestyle – like making electronic devices and driving automobile engines have consumed a tremendous number of resources such as rare earth metals and petrochemicals [3], [4]. Increased consumption and diminishing resources are making us reconsider our current production technologies and the way we use materials. Meanwhile, the world is dealing with pollution caused by the production and use of products [5]–[8]. A potential solution to this issue is to improve the efficiency of the manufacturing processes and strategically select and use resources in order to get the most out of our limited resources [9], [10]. In this regard, this thesis introduces a method to improve the process efficiency of the energy industry by employing strategic approaches to resource conservation and waste minimization, ensuring we make the best and most responsible use of our resources.

Process efficiency in the energy industry refers to the optimization of various processes involved in the production, conversion, transmission, and distribution of energy, with the aim of maximizing output while minimizing input and waste [11]. Improving process efficiency is vital for minimizing operational costs, conserving resources, and minimizing environmental impacts. The key aspects of process efficiency include effective resource utilization, waste minimization, and pollution prevention [12]. For positive

contribution towards global sustainability efforts, improving process efficiency in the energy industry is a multifaceted challenge that involves technological innovations and best operational practices. In response to the aforementioned challenges, this research endeavors to enhance the efficiency of processes within the energy industry. This improvement is pursued through the conservation of resources, reduction of production costs, increased productivity, enhanced managerial performance, and adherence to environmental standards. Figure 1 illustrates the pictorial representation of the main hypothesis of this research.

Figure 1. Research Hypothesis - Enhancement of Efficiency of Process Operations in the Energy Industry Using the Five Key Aspects.

The energy sector is at a pivotal juncture, bridging innovation with sustainability. It's within this context that the development of manufacturing devices and refinement of energy-related processes become crucial. Sustainable advancements in these domains can enable profound shifts within the energy industry, steering it towards a paradigm of improved efficiency and environmental consciousness. This research is focused on advancing operational efficiency and sustainability in the energy industry, targeting two pivotal domains: (a) Perovskite Solar Cells and (b) Packaging operations in multiproduct petroleum pipelines.

1.2 Computer-Aided Design of Perovskite Solar Cells

Out of many possible energy sources, solar energy is the most plentiful and easily accessible in most parts of the world. Each year, roughly 4 million Exajoules ($1EJ=10^{18}J$) of solar energy reaches our planet, with an estimated 5×10^4 EJ being readily harvestable [13]. Consequently, this significant potential has motivated global scientists and engineers to harness this energy in a more practical form. The technologies used to harness solar energy can be grouped into two main categories: (1) Solar thermal technology that transforms solar energy into thermal energy using devices such as solar collectors, heaters, dryers, etc. [14]–[16], (2) Photovoltaic (PV) technology that converts solar energy directly into electricity [17], [18]. In recent years, photovoltaics has gained comprehensive attention due to its ability to provide sufficient amounts of energy to satisfy our power demands and different types of PV materials have been developed over time. Since the discovery of the PV effect in the nineteenth century, PV cells have been classified into three generations of technology: The first generation includes commercially available silicon solar panels [19], [20]. However, due to the high cost associated with the fabrication

of silicon solar cells, advancement in technologies to harvest solar energy more economically and efficiently has always been an area of interest. The second generation of solar cells encompasses the thin-film solar technology usually fabricated using the element cadmium, while the efficiency of these cells is comparable to those of silicon, the rarity, and high toxicity of cadmium has prevented this technology from reaching its full potential [21], [22]. The third generation of photovoltaic cells includes the emerging cell technologies that are still under the R&D phase: Dye-Sensitized Solar Cells (DSSC), Quantum Dots and Perovskite Solar Cells [23]. Perovskite, the third material classified as the generation three solar cell, has shown an exceptional increase in performance since its discovery. Calcium Titanate ($CaTiO_3$) was the first perovskite discovered by Gustav Rose in 1839 in the Ural Mountains of Russia and was named after a famous geologist at the time, Lev Perovski [24]. Structurally, perovskite is a three-dimensional, simple, and highly symmetric crystal consisting of two cations combined with three anions and is defined with the stoichiometry of ABX_3, where A is a monovalent cation, B is a divalent metal cation and X is an anion (usually a halide or oxygen). One of the most stimulating property of perovskites that is fascinating researchers around the world is its application in photovoltaic cells. Since then the advancement in the field has increased drastically and perovskite solar cells have shown remarkable progress in recent years with a rapid increase in power conversion efficiency, from about 3.8% when the field took off in 2009 to efficiencies exceeding 26% (for single-junction cells) in 2023 [25]–[29]. The unremitting entity that has led to a drastic increase in efficiency of the perovskites is the device structure engineering and material composition [30]. Furthermore, the possibility of less expensive fabrication techniques through the use of low-cost materials has made perovskites the

fastest improving PV technology. Despite the advancements, the majority of high-efficiency perovskite solar cells (PSCs) remain confined to laboratories, unable to withstand harsh environmental conditions including extreme light, heat, and humidity, which leads to their degradation [31]. The instability of the cells has been mostly related to the organic ions of the cell such as Methylammonium (MA) and Formamidinium (FA) [20], [32], [33]. These organic cations are hygroscopic and volatile and thus, absorb moisture from the surrounding environment [34]. Continuous attempts are being made by the researchers to achieve better stability devices and different solutions are being proposed, such as improvisations to the structure design and composition of the cells. In recent years it has been found that replacing the organic cations with inorganic cesium ion resulted in better stability of the cell [35]–[37]. To raise the transition from lab to commercial production, it is vital to overcome several hurdles such as creating stable, scalable, and economical high-efficiency devices. A significant aspect of this involves replacing the toxic lead-based components with more sustainable alternatives without compromising on power conversion efficiency and keeping fabrication costs low [30]. Hence, modeling and simulation of materials can play a significant role in finding new functional materials that meet the requirements of perovskites.

Addressing these challenges, our research leverages computer-aided molecular design (CAMD) to develop novel perovskite crystals with desired features by exploring different combinations of components at the A, B, and X sites in the ABX_3 structure. Our focus extends to using Goldschmidt tolerance factor and octahedral factor to achieve improved stability and durability. Through CAMD, we aim to explore new materials for PSC technology characterized by low-cost, reduced toxicity, high PCE, and sustainable

solutions, bringing forward an optimized synthesis pathway for innovative organic-inorganic analogs for perovskite crystals. Figure 2 illustrates a graphical approach of our work.

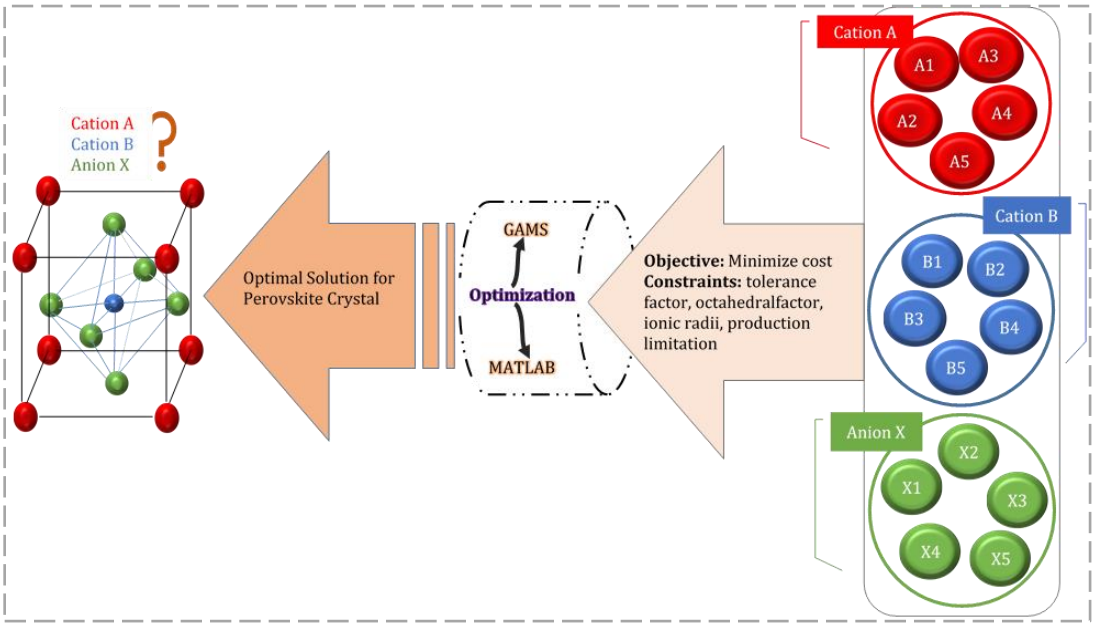

Figure 2. Optimal Selection of Ions Using Computational Tools for Computer-Aided Synthesis of Perovskite Solar Cells.

Despite the advancements in the development and adoption of renewable energy resources like solar energy, the global reliance on petroleum (oil and its byproducts) is unlikely to decrease significantly in the near future. Given that oil is a finite resource, it becomes crucial to enhance the efficiency of processes involved in converting crude oil into refined petroleum products. This is essential to maximize the judicious use of resources and mitigate associated environmental risks. To this end, the following section introduces the second domain of this research which entails developing efficient and sustainable manufacturing and packaging operations in multiproduct petroleum plants.

1.3 A Roadmap for Efficient Manufacturing and Packaging Operations in Multiproduct Plants

Multiproduct plants refer to industrial facilities or manufacturing plants that produce more than one type or category of product through batch operations within a single location. These plants are designed to handle the manufacturing and processing of various products simultaneously, allowing for efficiency in resource utilization and operational processes [38]. Therefore, such facilities are commonly utilized in numerous downstream petroleum operations [39], [40]. Instead of having separate pipelines for each product, the multiproduct plants utilize a multiproduct pipeline system for efficiently transporting various products from one location to another. Although, multiproduct pipelines make the transportation cost-effective, however, they present a unique challenge: the necessity for thorough cleaning between changeovers to prevent cross-contamination. At present, the cleaning procedure heavily depends on a trial-and-error method, involving the use of a valuable finished product from an upcoming batch, known as flushing. This practice results in the degradation of the high-value product, and due to stringent quality standards, it becomes unsuitable for its intended purpose, causing considerable economic setbacks. The trial-and-error approach often leads to excessive consumption of these valuable products, a situation that could be mitigated with more effective decision-making strategies. In extreme cases, the product has to be discarded, giving rise to environmental concerns. To this end, our work focuses on the implementation of novel process optimization methods and greener production techniques to improve the manufacturing and packaging operations in multiproduct plants. Our goal of improving the process efficiency will be achieved by reductions in the greenhouse gas (GHG) emissions, energy conservation, efficient raw

materials, and resource utilization, waste minimization, cost savings, and integration of all the aforementioned aspects into a novel and modernized greener production processes at the multiproduct plants. Our research follows a holistic approach, incorporating a wide array of techniques ranging from experimental characterization and process design to mathematical modeling, optimization, and data driven approaches. Through the integration of testing, control, and unit operations, we aim to explore and eventually rectify the existing shortcomings in these facilities. Our research is structured around a three-pronged approach, as depicted in Figure 3.

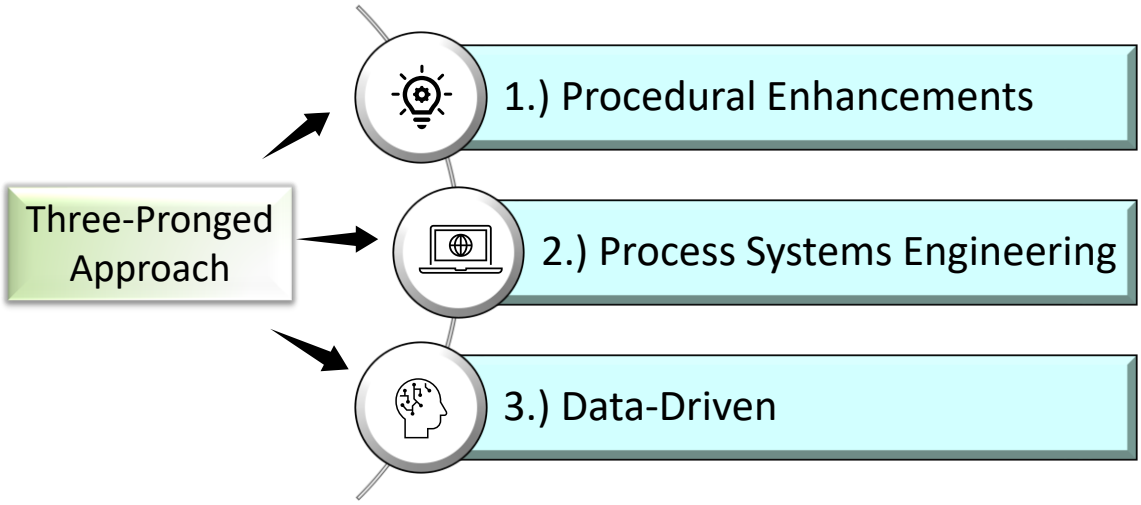

Figure 3. Strategic Optimization of Manufacturing and Packaging Operations in Multiproduct Petroleum Pipelines.

The first approach, Procedural Enhancements, involves an in-depth analysis of current flushing operations through collaboration with a leading lube oil industry based in North America. The primary objective of this phase is to understand the limitations of existing operations and develop solutions that require minimal to no capital investment.

Improving standardized operations to address the shortcomings of the current procedures was chosen as the focus for this approach. The second approach is Process Systems Engineering, where we aim to capture the dynamic nature of the flushing operation by framing it as an optimal control problem. The third prong of our research is the Data-Driven approach. In this phase, we delve into the data generated by the existing operations, employing machine learning algorithms to recognize patterns and identify key features with significant impact on the flushing operations. These identified key features are then incorporated into the existing process models to optimize the flushing operations, enhancing their efficiency and effectiveness.

To this end, the thesis is organized into eight chapters to systematically address the research objectives. In Chapter 1, the motivation behind the work is introduced, and a brief overview of the solution approach is provided. Chapter 2 offers an in-depth literature review and important background information relevant to the research. Chapter 3 details the work on Computer Aided Design on Perovskite Solar Cells, outlining the research methodology, solution strategy, and presenting the results and discussions. Chapter 4 explores the Optimization of Flushing Operations in Lube Oil Industries, offering insights into existing packaging operations and alternative solution strategies. Chapter 5 focuses on the first solution approach, presenting experimental studies 1, which involve the development and examination of a benchtop experimental rig. Moving on, Chapter 6 provides details of experimental studies 2, concentrating on the design and development of the pilot plant. Chapter 7 introduces the second approach, which involves process systems engineering. In Chapter 8, the third approach is explored, incorporating data-driven

methods and machine learning. Finally, Chapter 9 summarizes the key findings and recommendations for future work.

Chapter 2

Literature Review and Background

2.1 Perovskite Solar Cells

Inspired by the experimental findings for perovskite solar cells, researchers have carried out numerous computational studies in recent years. Atomistic modeling and simulation methods such as density functional theory (DFT), many-body perturbation theory, and pair-wise interatomic potential molecular dynamics (MD) have been successfully applied to find higher efficiency halide perovskites [41]. Through computer modeling, an understanding of the practical efficiency limitations of perovskite photovoltaics was developed based on the transfer-matrix analysis. This led to the prediction of the relationship between photocurrent and incidence light [42]. The light transmission to the perovskite absorbers was modeled using a transfer matrix method. Besides the conventional fluorine-doped tin oxide (FTO) transparent conductors, aluminum-doped zinc oxide (AZO), and indium-doped (ITO) tin oxide were also investigated to optimize the efficiency [43]. A physics-based analytical model that describes the current-voltage characteristics of perovskite solar cells has been developed. This model helps in determining the parameters of the solar cell [44]. Machine learning (ML) and density functional theory (DFT) have been combined to predict undiscovered hybrid organic-inorganic perovskites based on bandgap to solve the problems of toxicity and stability. To determine the crucial features that have significant impact in the bandgap of the device, the authors implemented a gradient boosting regression (GBR) algorithm [45]. To evaluate the exposed lead-containing compounds in perovskite solar cells and their impact on the environment and humans, environmental fate modeling (EFM) was carried

out by Yoo et al. 2019 [46]. The authors proposed a methodology to define a safe management range for perovskites. The potential hazard under two main accidental conditions in practical usage (fire and water exposure) was studied using EFM. Qiu et al. 2018 [47] evaluated the sustainability of perovskite solar cells for industrial production through a Life Cycle Analysis (LCA). The authors highlighted that the lead concentration of the conventional lead-based cells is 0.55%, which is five times higher than the limits stated by the Restriction of Hazardous Substances Directive (RoHS) (0.1%). Optical and electrical modeling was combined by Da et al. 2018 [48], to understand the energy loss mechanisms and promote the device performance of perovskite solar cells. Futscher et al. 2017 [49] merged optical model with an analytical model to simulate perovskite solar cells and predict the behavior of the cells under realistic conditions. Albrecht et al. 2016 [50], derived a thermodynamic model to predict the energy storage efficiencies of oxide-based perovskites. A modified drift-diffusion model was described by Liu et al. 2017 [51], to optimize the photocurrent in the UV visible region of a complete solar cell device. Raj et al. 2021 [52], used solar cell capacitance simulator (SCAPS 1D) to investigate suitable electron transport layer (ETL) for lead free $CsGeI_3$ based perovskites. The PSCs with C_{60} and SnO_2 ETLs exhibited superior device performance with power conversion efficiency of 8.46%. Tiwari et al. 2023 [53] studied the replacement of lead (Pb) based PSCs with tin (Sn) based for developing environmentally friendly solar cells. The authors selected methyl ammonium tin iodide ($CH_3NH_3SnI_3$) as the absorber layer and studied the effect of different electron transport layer (ETL) and hole transport layer (HTL) in the device structure by using SCAPS 1D simulation tool. Rani et al. 2023 [54], conducted computational investigation of inverse perovskite SbPX3 (X = Mg, Ca, and Sr) structured

materials using density functional theory (DFT). The authors tested the theoretical power conversion efficiency of the proposed materials and reported that the materials are extremely stable and have substantial absorption in visible, UV, and NIR bands.

As can be gleaned from the existing literature, there has been enormous work in the perovskite field, however, there has not been any specific work that simultaneously focuses on stability and cost of perovskite crystals. Furthermore, from literature, it can be noted that there are other possible alternatives to site-A, site-B, and site-X ions that can serve as a potential substitute for the conventional lead-based perovskite solar cells. To bridge this gap, presented here is an integrated stability and cost-based perovskite crystals synthesis approach. Our work presents the platform that can help find other possible combinations of ions for the synthesis of perovskite crystals with desirable stability characteristics at low costs.

2.2 Manufacturing and Packaging Operations in Multiproduct Petroleum Plants

Renewables growth did not diminish the dominance of petroleum-based fuels. The United States encompasses a diverse array of energy sources, categorized broadly as renewable and non-renewable [55]. Among these sources, petroleum has traditionally held the dominant position in terms of annual energy consumption, contributing to 36% of the total energy consumption as depicted in Figure 4 [27]. In 2022, the United States averaged approximately 20.28 million barrels per day of petroleum consumption [28]. It is now widely recognized that our reliance on petroleum is significantly unfavorable to the environment. However, finding a viable alternative to oil remains a considerable challenge, given its availability and suitability for various purposes. To this end, sustaining the vitality of the U.S. petroleum refining sector necessitates a continual focus on enhancing

operational efficiency, which involves integrating operational efficiency into a company's strategy as a pivotal aspect of its environmental sustainability effort.

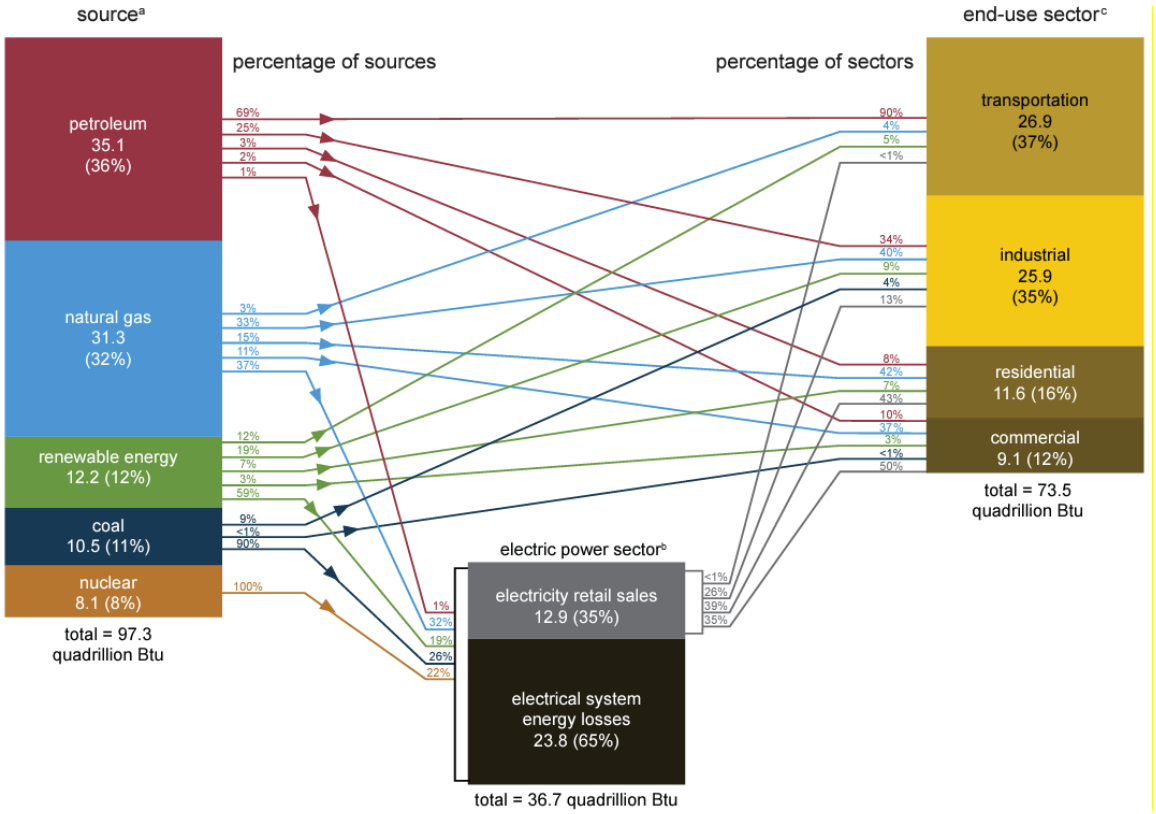

Figure 4. U.S. Energy Consumption by Source and Sector (U.S. Energy Information Administration (EIA), 2022 [55])

In today's business landscape, organizations are required to take into account three fundamental elements while formulating their strategies: people, planet, and profit. Consequently, industries must carefully evaluate two key factors in the management of their energy consumption: its environmental impact and its financial implications. When it

comes to crude oil, even though it can be traded, it's not useful until it goes through a process to turn it into valuable products like fuels, lubricants, and bitumen [56]. This refining process is called "downstream operations" in the petroleum industry [57]. Being able to make this process more efficient and use less energy is a key factor in how competitive a company can be in the downstream sector [58]. To achieve these goals, companies need to make smart and cost-effective investments in technologies and practices that use energy more efficiently, helping them meet both their environmental constraints and financial targets.

2.2.1 Lubricants: One of the Highest Consumed Petroleum Products

Among various other extensively consumed petroleum products like Gasoline, Diesel Fuel, and Hydrocarbon Gas Liquids, the United States holds the distinction of being the largest consumer of petroleum lubricants [59]. In the year 2022, the U.S. exhibited an average consumption of 41 million barrels of lubricants [58]. Lubricants are substances that play a pivotal role in enhancing the performance and lifespan of bearings and machinery. The idea of lubrication is not novel at its core, it is rather straightforward. Centuries ago, farmers used animal fat to lubricate the axles of their ox carts. However, with the evolution of modern machinery, which is significantly more complex than the ox carts of the past, the requirements placed on lubricants have become much more precise. Despite this, the fundamental principle remains unchanged: preventing direct metal-to-metal contact by introducing a layer of fluid or fluid-like material [60]. The lubricants enhance the performance of modern machinery by reducing wear on moving parts, minimizing friction between rotating and stationary components, absorbing shocks, lowering operating temperatures, preventing corrosion of metal surfaces, maintaining

system cleanliness by excluding contaminants, and sealing and safeguarding critical components. Every liquid offers some degree of lubrication, but there are significant variations in their effectiveness. The choice of lubricating substance can often determine whether a machine operates successfully or faces failure. Lubricating modern machinery is essential for extending its lifespan. It is noteworthy that the incorrect selection and application of lubricants are significantly responsible for all machinery failures, underscoring the vital role of lubrication procedures in maximizing equipment reliability [61].

2.2.2 Composition of Lubricants

A lubricant is a complex mixture of 85-90% base stock and 10-15% of a combination of functional additives as illustrated in Figure 5.

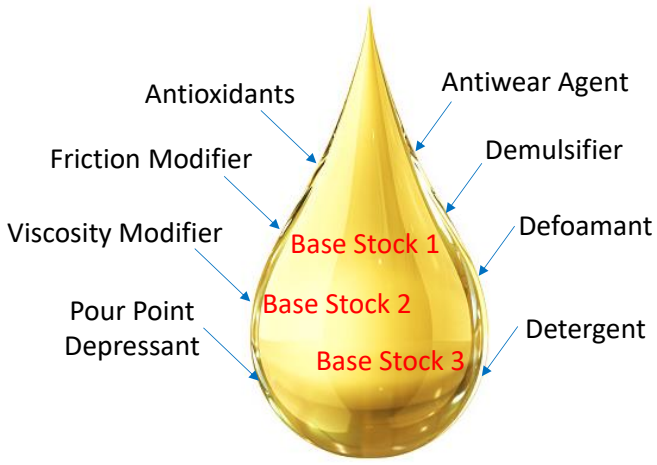

Figure 5. A Finished Lubricant Product Composition: Consists of 85-90% Base Stocks and 10-15% Functional Additive

The primary role of the base stock is to provide lubrication and serve as a carrier for additives. Additives, on the other hand, serve either to improve existing properties of the base stock or introduce new desired properties. Existing properties that can be enhanced include viscosity, viscosity index, pour point, and oxidation resistance. Examples of new properties additives can introduce encompass cleaning and suspending abilities, as well as antiwear performance. For instance, antioxidants can enhance the stability against oxidation and degradation in engine oil, while specific additives are employed to establish extreme pressure (EP) anti-wear properties required for gear lubrication. The base stock serves as the medium for these additives and, as a result, must have the capacity to keep them dissolved under typical operational conditions [62].

2.2.3 Lubricant Basestock

The lube oil basestock serves as the foundational element in which suitable additives are chosen and blended to achieve a precise equilibrium in the performance attributes of the final lubricating substance [63], [64]. Diverse methods for producing basestocks can yield products with the necessary qualities to create finished lubricants featuring desired performance standards. The basestocks contribute significantly to finished lube oil properties and can be of the following types: (i) Petroleum-based (from crude oil by distillation and special processing, (ii) Synthetic (from a chemical reaction of two or more simple chemical compounds), and (iii) Bio-based (from agricultural feedstock). Modifications in the standards for finished motor oils are driving a greater need for superior-quality lubricants that go beyond what traditional lubricant production methods involving solvent extraction, solvent dewaxing, and hydrofinishing can deliver [65]. To meet the demands for automotive lubricants with these upgraded

specifications, alternative methods like lube hydrocracking, deep hydrotreating, and wax hydroisomerization are being employed to produce lubricant base stocks [66]. In consideration to these shifts, the American Petroleum Institute (API) introduced a classification system for base oils. This classification uses physical and chemical parameters to divide the base stocks into five groups (I to V) as shown in Table 1.

Table 1

API Classification of Lube Base Stock (Source: [37])

Group	Saturates, wt.%	Sulfur, wt.%	Viscosity Index
I	<90	<0.03	>80 - <120
II	≥90	<0.03	≥ 80 - ≤ 120
III	≥90	≤0.03	≥ 120
IV	All poly alpha olefins		
V	All base stocks not in groups I to IV		

The classification is based upon saturates content, viscosity index, sulfur content and additives [61], [66], [67]. Transitioning from group I lubricants to group II lubricants results in an increase in both the paraffin content and the viscosity index (VI) of the base stock. Conventional lubricant technology, which includes solvent dewaxing and solvent dewaxing processes, remains economically viable primarily for the production of group I lubricants [65], [66]. On the other hand, group II and group III lubricant base stocks, which require very low sulfur levels, low volatility, and high VI to meet the demands of modern

automobile engines, can only be efficiently produced through alternative hydroprocessing methods [68], [69]. This does not imply that traditional lubricant manufacturing processes will be entirely replaced by alternative methods. Conventional techniques will continue to be essential for the production of high-viscosity lubricants. Additionally, lubricants intended for industrial applications, where a high viscosity index is not a critical requirement, may still be efficiently produced using conventional methods. The key factor in attaining the utmost levels of performance in these finished lubricants lies in understanding the interaction between base stocks and additives and aligning these with the requirements of machinery and operating conditions.

2.2.4 Functional Additives

Lubricant additives are continually evolving to enhance the performance and properties of modern lubricants [70]. Emerging technologies, including applications in space exploration and oceanic environments, demand the development of new lubricants with novel additive chemistries [71]. These additives can be organic or inorganic compounds that are either dissolved or suspended as solids within the base stock. Typically, they constitute anywhere from 0.1% to 30% of the total oil volume, depending on the specific application [72]. The primary functions of lubricant additives can be categorized into three basic roles:

(1) Enhancement of existing base stock properties: This involves the use of additives such as antioxidants, corrosion inhibitors, anti-foam agents, and demulsifying agents to improve the inherent characteristics of the base oil.

(2) Suppression of undesirable base stock properties: Additives like pour-point depressants and viscosity index improvers are employed to mitigate negative attributes of the base stock.

(3) Introduction of new properties to the base stock: Extreme pressure additives, including detergents, metal deactivators, and tackifiers, are utilized to impart unique qualities to the lubricant.

Lubricant additives are costly chemicals, and formulating the right mixture of additives is a complex science [70]. The choice of additives plays a crucial role in differentiating lubricants designed for specific applications, such as turbine oil, hydraulic oil, gear oil, and engine oil. Selection of these additives depends on their ability to effectively perform their intended functions, compatibility with the chosen base oils, interaction with other additives in the formulation, and overall cost-effectiveness [68].

2.2.5 Classification of Lubricants

Lubricating oils have numerous applications in a variety of fields and depending upon their final use they can be classified into the following types: (i) Engine oils (petrol and diesel engines, aircraft, marine engines), (ii) Turbine oils, (iii) Gear oils, (iv) Quench oils in metalworking, (v) Insulating oils, (vi) Chain lubricants, and (vii) Hydraulic oils. Each of these oils have distinguishing features [60]. Automotive engine oils have strict product performance claims and the viscosity index for these oils must match the desired levels to avoid plugging during the winter when temperatures can be extremely low. Industrial oils are incompatible with automotive oils. Industrial oils must be metal-free and are sensitive to contamination. When combined with automotive oil, emulsions and foaming can become an issue. Metalworking oils sometimes contain water which can

contaminate other oils and can corrode the system. Gear oils are made to withstand high pressures and can also form emulsions or lead to foaming when combined with another type of oil. Product integrity is extremely important to the oil-based automotive and chemical industries and therefore these different grades of oil must remain separate to ensure the best quality.

2.2.6 Lubricant Oil Blending Plants (LOBP)

The process of developing finished lubricants by combining different basestocks with functional additives is commonly known as lube oil blending, and the facilities dedicated to this process are referred to as lube oil blending plants (LOBP). Lube oil blending is the preferred term because it primarily involves mixing without significant chemical reactions. Nevertheless, the efficient operation of a modern blending plant is crucial for ensuring the production of the right quality and performance lubricants for customers. While blending lubricants may seem relatively easy, however, operating a blending plant is certainly not.

The blending process takes place in either inline blenders or off-line blenders, such as mixing kettles. Following this, the resulting finished products that are stored in storage tanks undergoes processing through a multiproduct pipeline system for packaging in various styles, including bottles, drums, and pails, as illustrated in Figure 6.

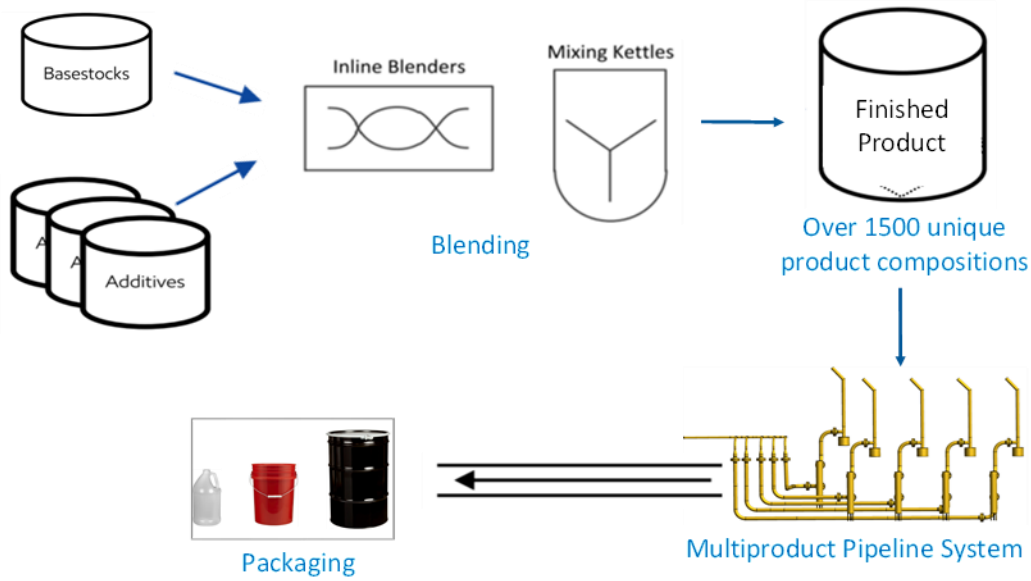

Figure 6. Blending and Packaging of Lubricant Products through a Multiproduct Pipeline System

Given that a typical lube oil blending plant produces over 2000 distinct products annually, it becomes impractical to maintain a separate processing system for each of these products. Hence, these facilities are categorized as multiproduct plants [40]. In these plants, various types and grades of products are manufactured and processed in sequential batch operations with batch capacities typically falling between 1000 and 30,000 liters. To maintain the integrity of each product batch, the entire system must be thoroughly cleaned and flushed between each changeover operation to prevent cross-contamination. The pipeline network within these plants can vary in diameter from as small as 1/8 inch to sometimes 4 inches or more. This network extends from the initial stages of vessel mixing, through the various process equipment used to the final packaging of products in containers like plastic bottles, pails or drums. The network often features numerous twists and turns, with raw materials passing through flow meters, filters, pressure regulators, and other

process instrumentation or metering devices. The complexity of this network makes thorough cleaning a challenging task. Furthermore, the use of external solvents for flushing operations is strictly prohibited because it introduces impurities into the high value finished products. Therefore, the traditional method involves using a finished product from an upcoming batch to clean any residues from the previous batch. Unfortunately, this flushing process generates a commingled (mixed) oil that doesn't meet the desired specifications of either batch, resulting in downgraded oil with low economic value. These issues have persisted for a long time and represent a significant economic challenge in these industries, with typical large-scale commercial facilities incurring losses exceeding $1 million per year due to these drawbacks.

2.2.7 Challenges with the Traditional Flushing Operations and Quality Control Techniques

Despite significant advancements in the field of lubricant tribology, the challenge of efficient packaging and successful flushing operations remains unaddressed in current literature. Presently, flushing procedures primarily rely on a trial-and-error approach, regulated by a flush timer. Operators select a flush duration based on their past experiences with a specific product. At the conclusion of the flushing process, samples are collected and sent to the laboratory, where it undergoes a series of physical and chemical tests to confirm the lubricant's top-grade quality. Typical physical tests involve assessing viscosity, specific gravity, and color, while common chemical tests include flash and fire point evaluations. Out of the several tests, viscosity is the preliminary and most crucial test that ensures the batch quality and the success of the flush. If viscosity test results fall outside

the desired range, additional flushing is carried out, and this cycle continues until the desired specifications are met.

In the traditional flushing method, sampling serves as the primary quality control and monitoring technique. However, this approach results in extended hold times and downtime. Moreover, in many cases, it leads to excessive flushing, resulting in the generation of large quantities of commingled oil and substantial economic losses for these industries. In some instances, the commingled product becomes commercially unviable and poses challenges in terms of disposal. Lubricants, both fresh and used, can pose significant environmental hazards, primarily due to their potential for severe water pollution [73]. The main classes of additives, such as succinimide ashless dispersants, calcium sulphonates, calcium phenates, zinc dialkyldithiophosphates, oxidation inhibitors, and anti-wear inhibitors, can be harmful to the environment's flora and fauna. The persistence of lubricants in the environment depends largely on the basestock, but the use of highly toxic additives can worsen this persistence issue. To minimize the inadvertent release of lubricants into the environment, it is imperative to develop more environmentally friendly and energy-efficient technologies by optimizing the efficiency of processing operations. With this objective in mind, our study aims to address these limitations and explore alternative operational methods aimed at reducing commingled oil volumes and improving the economic and resource management aspects of flushing operations in the lubricant industry. To achieve this goal, our work seeks to rectify existing drawbacks and enhance flushing operations by employing model-predictive optimization techniques, experimental characterization, innovative solution strategies, and data-driven approaches.

2.3 Product Cross Contamination in Crude and Refined Petroleum Pipelines

A common example of pipeline flushing operation is also encountered by the crude oil refineries during the process of batching. Batching involves the transportation of different grades of crude oils and finished petroleum products such as diesel and gasoline through an extensive length of pipelines that are operated continuously throughout the year. Interfacial mixing and cross contamination, therefore, arises as an unavoidable problem in the refineries. Various approaches that are used by the crude oil refineries for the key predictions in their respective flushing operations are used as guidance in our work.

Pipeline flushing is greatly influenced by the hydrodynamics and flow regimes of the fluids [74]. Therefore, for conducting an efficient flushing operation, it is important to understand the fluid flow characteristics and estimate various parameters such as pipe dimensions, fluid viscosity, density, flow rates, and mixing length. One of the earliest investigations of longitudinal mixing during sequential transportation was studied by Taylor 1922 [75]. The author reported "Convection-Diffusion" as the theoretical phenomenon that governs interfacial mixing. The convection-diffusion equation is established by convection and diffusion effects which are the two most important factors affecting the mixed segment. The concepts introduced by Taylor 1953 [76], [77], have been extensively used as the starting point in most of the studies of interfacial mixing, and a number of empirical models have been reported for approximating the interfacial mixing. Investigators have identified a list of parameters and put forth empirical correlations regressed from experimental data. The system-specific empirical models provide essential knowledge of the formation of the mixed oil in the form of length or volume basis [78].

Currently, the formulas predominantly utilized by major petroleum corporations to determine the length of mixed oil segments are largely empirical, one-dimensional, and tailored to each company's individual systems, taking into account intricate operational circumstances, pipe variables, and oil varieties [79]. The industry lacks a universally accepted standard formula applicable to all systems under real-world conditions. Key parameters influencing the decision-making process in determining the length of the mixed oil segment encompass the transportation range, the diameter of the pipeline, and the Reynolds number. Two-dimensional and three-dimensional simulation models have been employed to enhance the one-dimensional models as reported in various references [79]–[81]. Specifically, He et al. 2018 [79], used three-dimensional numerical simulations using computational fluid dynamics (CFD) to represent the volume concentration distribution of oil mixing in horizontal pipelines. Despite providing detailed insights, these three-dimensional models had a notable limitation; they are unsuitable for real-time calculation applications. To determine the efficacy of the empirical formula and validate the simulation results, a series of tests were conducted utilizing a sequential transportation experimental loop platform. Baptista et al. 2000 [80], introduced models that factor in the time-dependent flow rate and concentration-dependent effective dispersion coefficient to estimate mixing volumes of consecutive product batches operating under turbulent flow conditions. They validated the performance of their non-linear models using a finite volume method and demonstrated superior alignment with existing semi-empirical models. Zhang et al. 2017, [81] devised a scheduling strategy using a MILP approach, aiming to decrease operating expenses by addressing both operational constraints and interfacial mixing issues while taking into account the physical properties of different oil batches. In

parallel, Liu et al. 2019 [82], analyzed the formation mechanism of trailing oil during the transportation of diesel oil followed by gasoline, employing CFD simulations and multi-nonlinear regression to understand various factors including oil substitution time and flow speed. Liu et al. 2020 [83], explored the mixing phenomena at inclining pipeline sections, deriving correlations involving batch replacement time, mixing section volume fraction change time, and sectional flow velocity. Together, these studies offer a comprehensive view of the complexities of multiproduct pipeline operations and propose strategies to optimize them through detailed mathematical and computational approaches.

Extensive studies have been conducted on the formation of commingled oil within crude and refined petroleum pipelines, which transport multiple fluids consecutively during continuous operations. However, to the best of the author's knowledge, no prior studies have been published concerning multiproduct pipelines utilized in the production and packaging of finished lubricants.

To this end, concluding with the literature review and background of the two domains of this research, the next chapter delves back into the exploration of Computer-Aided Design for Perovskite Solar Cells. It provides an overview of the research methodology, explains the solution strategy, and presents a comprehensive discussion of the results.

Chapter 3

Computer-Aided Design of Cost-Effective Perovskite Crystals

Text and figures are reproduced and adapted with permission from S. S. Jerpoth, J. Iannello, E. A. Aboagye, and K. M. Yenkie, "Computer-aided synthesis of cost-effective perovskite crystals: an emerging alternative to silicon solar cells," *Clean Technol. Environ. Policy*, vol. 22, no. 5, pp. 1187–1198, Jul. 2020, doi: 10.1007/s10098-020-01861-8.

3.1 Overview

Perovskites are promising materials that have gained attention in recent years due to their increasing efficiencies in application to photovoltaic devices [82]. However, the high-efficiency perovskite solar cells (PSCs) that have been reported by far have only been manufactured on a lab scale under controlled environmental conditions. The device does not possess the capability to withstand severe atmospheric circumstances such as light illumination, heat, and humidity; hence, it tends to degrade. For the commercial-scale development of PSCs, the key challenges that need to be addressed include developing a stable, scalable, and cost-effective high-efficiency device. Another area is the use of less toxic and sustainable alternatives to conventional lead-containing perovskites that have high toxicity index.

The key component of a PSC is the perovskite crystal, which is used as a photo absorber and is represented by the stoichiometric formula of ABX_3, where A and B are cations, and X is an anion. The essential stability criteria for a crystal to be classified as perovskite include Goldschmidt's tolerance and octahedral distortion factors [31]. Almost all the high-efficiency PSCs consist of methylammonium or formamidinium at the 'site-

A', lead at the 'site-B', and halide (chloride, bromide or iodide) at the 'site-X' [30]. However, there can be different combinations for the site-A cations, site-B cations, and site-X anions, which can aid in devising novel crystals with superior properties. In addition to being stable, other key factors for determining the market competence of PSCs include the Power Conversion Efficiency (PCE) and device fabrication costs. Hence, we propose Computer-Aided Molecular Design (CAMD) methods for generating novel PSC configurations with superior properties.

This work is an attempt to solve the complex problem of synthesizing PSCs at low costs, low toxicity, high power conversion efficiency, long-term stability, and sustainability. We formulate and solve an optimum synthesis problem that accounts for finding new organic-inorganic analogs for the perovskite crystals through computer-aided molecular design.

3.2 Parameters Affecting the Structural Stability and Power Conversion Efficiency of Perovskite Solar Cells

The work focuses on designing cost-effective perovskites by finding out candidate options for positions A, B, and X for the ABX_3 chemical structure of perovskite using computational tools. To determine the formability of perovskites two important dimensionless descriptors, the tolerance factor 't' and the octahedral factor 'μ' play an important role [83]–[85]. These descriptors were proposed by Victor Moritz Goldschmidt in 1926 and are stability factors. In this approach, the perovskite is considered as a collection of rigid spheres with ionic radii R_A, R_B, and R_X. Goldschmidt inferred a relation between these ionic radii and confirmed that size and geometry play an important role.

3.2.1 Tolerance Factor

The tolerance factor 't' is defined as the ratio of the distance A-X to the distance B-X. For an idealized solid sphere model:

$$t = \frac{R_A + R_X}{\sqrt{2}(R_B + R_X)} \quad (1)$$

Where:

R_A: Ionic radii of cation A

R_B: Ionic radii of cation B, and

R_X: Ionic radii of anion X.

The ionic radius of cation A is always greater than that of cation B. Figure 7 depicts the different configurations of perovskite crystal based on the tolerance factor. The best device performance is obtained with cubic symmetry due to high ionic bonding. When the tolerance factor exceeds the ideal range an octahedral or tetragonal tilting occurs which affects the electronic properties of the device [86].

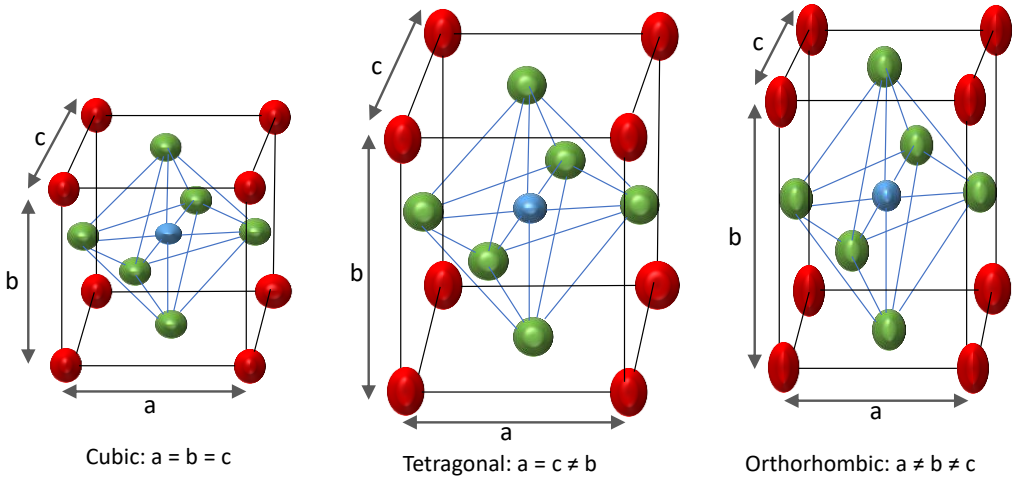

Figure 7. Illustration Depicting Different Configurations of Perovskite Crystal Based on Tolerance Factor (Red: A site, Blue: B site, Green: X site)

3.2.2 Octahedral Factor

The octahedral factor μ is defined as the ratio of ionic radii of cation B to the ionic radii of the anion X.

$$\mu = \frac{R_B}{R_X} \tag{2}$$

Table 2 shows the desired range of t and μ for the formation of a stable perovskite. When considering perovskite as a light harvester the material must fall within the ideal range of tolerance factor and octahedral factor. Materials that do not lie within the ideal range will degrade rapidly resulting in disruption of the device.

Table 2

Stability Factor Range for Ideal Crystal Structure (Source: [7], [19], [48], [49])

Stability Factors	Range	Description
Tolerance factor (t)	0.7-1.11	The material can be defined as a perovskite crystal
	0.8-1	Ideal cubic structure
	0.94-0.98	Best device performance
	<0.8	Orthorhombic structure
	>1	Hexagonal structure
Octahedral factor (μ)	0.44-0.90	Ideal crystal structure

Our present contribution proposes a methodology that can select an optimum combination of different materials for the perovskite solar cell based on the tolerance factor and the octahedral factor, which are amongst the important parameters that determine the stability and formability of a perovskite solar cell. Through an extensive literature review, we have explored some of the analogs to the hybrid lead halide perovskites that have been investigated in some recent work (Kieslich et al. 2015, 2014; Hoye et al. 2017). The goal is to develop a model that selects the possible combination of different ions for the perovskite cell based on the stability factors and simultaneously minimizes the material cost, which is considered a significant criterion for large scale commercialization of perovskite solar cells.

3.3 Formulation of Optimal Synthesis Problem for Finding Novel Analogs in the Perovskite Crystals

In our model, we first define three sets representing cation A, B, and anion X. Set A and B consist of fifteen elements (or ions), whereas set X consists of nine ions. These elements or ions (shown in Table 3) have been explored through extensive literature review and can serve as the potential analogs for each of the positions A, B and X in the perovskite crystal structure [87], [88].

The parameters associated with our models are the ionic radii of the ions, the molecular weight of each ion, as well as the cost of each ion per gram ($/g). The mathematical constraints are categorized into three parts: molar constraints, binary constraints, and stability constraints. The molar constraints constitute the ratio 1:1:3, which conforms to the general perovskite crystal structure. The binary constraints consist of that for cation A, cation B, and anion X. The stability constraints equation is made up of

Goldschmidt's tolerance factor, octahedral factor, and ionic radius constraints. The tolerance factor has a lower limit of 0.9 and an upper limit of 1.12. Correspondingly, the octahedral stability factor has a lower limit of 0.44, and an upper limit of 0.9. The radius constraint is implemented to make sure that cation A always has a bigger ionic radius than cation B. The cost objective function is made up of multiplication of the moles of each ion required, the molecular weight of that particular ion, and the cost per gram of that ion. Equations (3) - (12) gives a summary of all the mathematical equations that were developed.

Table 3

Potential Ions for the Position A, B and X in the Perovskite Crystal (Source [51], [52])

Ion			Effective Ionic Radii (Å)			Cost ($/gram)		
Cation A	Cation B	Anion X	Cation A	Cation B	Anion X	Cation A	Cation B	AnionX
Ammonium	Cadmium	Chloride	1.46	0.95	1.81	13.4	68.3	30.75
Hydroxyl-ammonium	Lead	Iodide	2.16	1.19	2.2	152.4	183	84
Methyl-ammonium	Tin	Bromide	2.17	1.18	1.96	32.6	25.9	91
Hydrazinium	Bismuth	Fluoride	2.17	1.03	1.285	56.5	59.6	980
Azetidinium	Calcium	Selenium	2.5	1	1.98	712	83	725
Formamidinium	Indium	Oxygen	2.53	0.8	1.4	54.5	992	146
Imidazolium	Mercury	Sulphur	258	1.02	1.84	1396	77	13.9
Dimethylammonium	Palladium	Tellurium	2.72	0.86	2.21	1052	8576.09	112
Ethylammonium	Strontium	Formate	2.74	1.18	1.36	940	768	18.2
Guanidinium	Magnesium		2.78	0.72		740	19.1	
Tetramethylammonium	Lithium		2.92	0.76		70.6	215	
Thiazolium	Gallium		3.2	0.62		473	758	
3-Pyrollionium	Iridium		2.72	0.82		16000	2780	
Tropylium	Lanthanum		3.33	1.03		3536	780	
Tert-butylamine	Cobalt		3.03	0.7		59.9	1428	

The following are the steps involved in the mathematical formulation of the problem: *Step#1* define the parameters and sets needed for the problem, *Step#2* construct a discrete optimization model as a mixed integer linear program which consists of mass balances, and cost equations, *Step#3* minimize the cost of perovskite crystal based on the selected sites A, B, and X ions.

3.3.1 Definition of Sets

A set of fifteen cations for position A, fifteen cations for position B, and nine anions for position X are developed based on an extensive literature review. Each ion in set *i* can take up different elements in set *j*. For example, the number of cations for site-A are A1, A2, and A3. Equation (3) shows the mathematical expression for these sets.

$$Sets \;\; i \;\; \in (A, B, X)$$

$$j \;\; \in \;\; (1,2,3, \ldots . 9) \tag{3}$$

3.3.2 Model Parameters and Variables

Below are the model parameters and variables used for the problem formulation. The model parameters are:

α	-- total moles (1 mol) of perovskite
$\pi_{(i,j)}$	-- Cost ($/g) of ion
$\gamma_{(i,j)}$	-- Ionic radii (Å) of ion
$\omega_{(i,j)}$	-- molecular weight of ion

and the model variables are:

$m_{(i,j)}$	-- moles of ion
$Y_{(i,j)}$	-- Binary variable for ion
t	-- Goldschmidt's tolerance factor
μ	-- Octahedral factor
C	-- Total cost ($) of perovskite crystal

3.3.3 Objective Function

Similarly, model parameters, being the ionic radii, molecular weight, and cost per g of each selected ion are also deduced from literature. Integer optimization is employed in the problem formulation. This allows us to select one site-A cation, site-B cation, and site-X anion that satisfies the earlier factors stated, as well as minimize the cost. Below is the mathematical equation for the objective function (Obj).

$$Obj = C = \sum_{i=A,B,X} \sum_{j=1}^{3} \pi_{(i,j)} m_{(i,j)} \omega_{(i,j)} \quad ; \ \forall \quad i,j \tag{4}$$

3.3.4 Model Constraints

The total moles of perovskite crystal considered is 1 mol as shown in Equation (8). Since the ratio of A, B, and X in the perovskite crystal is 1:1:3, a constraint is added to make sure the perovskite produced satisfies this requirement as shown in Equation (7). The upper and lower limits required for the moles of each ion is shown in Equation (5) and Equation (6) respectively.

$$m_{(i,j)} \leq \alpha Y_{(i,j)} \ ; \ \forall \ i,j \tag{5}$$

$$m_{(i,j)} \geq 0 \ ; \ \forall \ i,j \tag{6}$$

$$m_{(A,j)} = m_{(B,j)} \ ; \ 3m_{(A,j)} = m_{(X,j)} \ ; \ \forall \ j \tag{7}$$

$$\sum_{i=A,B,X} \sum_{j=1}^{3} m_{(i,j)} \geq \alpha \ ; \ \forall \ i,j \tag{8}$$

Since only one ion can be selected for each ion category, a binary variable constraint is added which limits the choice of each ion to one. Equation (9) gives the mathematical equation for this constraint.

$$\sum_{j=1}^{3} Y_{(i,j)} = 1 \; ; \; \forall \, i,j \tag{9}$$

Stability is of paramount importance in the production of any perovskite crystal. Goldschmidt's tolerance factor shown in Equation (10), helps in deciding which combination of ions will give a stable crystal structure. Further to this, the octahedral shape of the perovskite crystal should be maintained. Therefore, Equation (11) rectifies that problem. The size of cation A is greater than that of cation B hence, this constraint was added to ensure that this condition is met. Equation (12) shows the mathematical equation of this constraint.

$$t = \frac{\left[\gamma_{(A,j)} Y_{(A,j)}\right]\left[\gamma_{(X,j)} Y_{(X,j)}\right]}{\sqrt{2\left\{\left[\gamma_{(B,j)} Y_{(B,j)}\right] + \left[\gamma_{(X,j)} Y_{(X,j)}\right]\right\}}} \; ; \quad \forall \quad j \tag{10}$$

$$where: \; 0.90 \leq t \leq 1.12$$

$$\mu = \frac{\gamma_{(B,j)} Y_{(B,j)}}{\gamma_{(X,j)} Y_{(X,j)}} \; ; \quad \forall \quad j \tag{11}$$

$$where: 0.44 \leq \mu \leq 0.90$$

$$\gamma_{(A,j)} > \gamma_{(B,j)} \; ; \quad \forall \quad j \tag{12}$$

3.4 Solution Strategy for Exploring Novel Analogs for Perovskite Crystal Synthesis

A tree representation approach is used to simplify the developed optimization problem. This kind of representation is used when one wants to represent a clear path to the final decision. Three general nodes are involved in representing a problem in a tree format which are as follows: the initial nodes, the intermediate nodes, and the terminal nodes. In our problem, the initial nodes are cations A, the intermediate nodes are cations

B, and the terminal nodes are anions X. After developing the tree structure for the problem, the next step is to find an optimum path. Integer programming is used for the formulation of the optimization problem. This solution is executed using a mixed-integer programming (MIP) solver in General Algebraic Modeling Systems (GAMS) software. Even though GAMS possess higher capabilities for solving integer programming, we further implement our mathematical models in MATLAB to verify our results and test the strength of MATLAB when it comes to solving integer programming problems. The 'Intlinprog' solver is used in MATLAB for this analysis. Figure 8 shows a summary of our solution strategy. We first start by initializing our sets, parameters, and equations. Then the Goldschmidt's tolerance factor and the octahedral factor are calculated for a set of cation A, cation B, and anion X. If the calculated values are within the tolerance limits, then the cost for that combination is calculated. If the selected ions do not meet the tolerance factor criteria, different combinations are selected, and the process repeats itself. This is done until all the possible combinations are covered. Furthermore, for the combinations which are within the tolerance limits, the cost is calculated, and finally, out of the calculated individual costs, the one with the minimum value is displayed. This displayed combination of A, B, and X along with the minimum cost is the optimum solution.

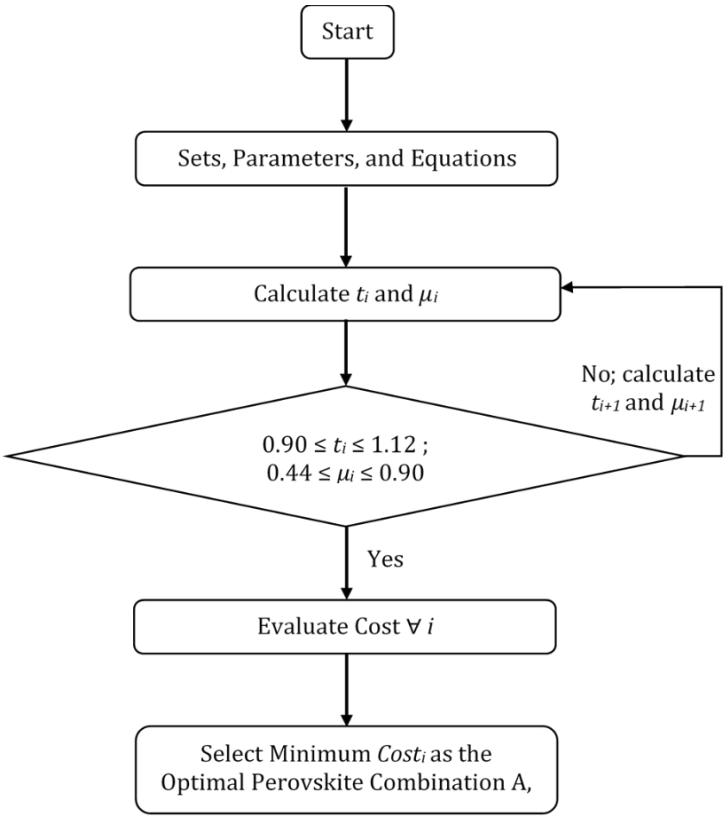

Figure 8. Flowchart for Optimal Perovskite Crystal Synthesis Based on Goldschmidt Tolerance Factor and Octahedral Factor.

Our three-ion motivational case study is further extended to a second case wherein we use fifteen A-cations, fifteen B-cations, and nine X-anions which are decided through an extensive literature review. The objective of the problem is to extend the model to several possible combinations of A, B, and X to determine the perovskite ABX_3 based on cost minimization, subject to the same mathematical equations used for case study#1 (see supplementary materials for all the ions used for this analysis, together with their ionic radii, molecular weight, and cost). Furthermore, this model is extended to a third case study in which the cation A is restricted to Cesium (Cs^+) while all other ions for cation B and

anion X are maintained. The goal is to determine a combination of Cesium with cation B and anion X that would result in the lowest cost subject to all the mathematical models presented earlier in case one.

3.5 Results and Discussions

The following sections illustrate the results of the two case studies and also provides detailed discussions.

3.5.1 Case Study #1

With A1(Methylammonium) being the root of the tree, the selected B site is B3(Tin), and the selected X site is X1(Chloride). The associated cost for this path is 0.2874 $/g of perovskite crystal produced. With A2 (Dimethylammonium) being the root of the tree, the selected B site is B3(Tin), and the selected X site is X1 (Chloride). The associated cost for this path is 2.0222 ($/g) of perovskite crystal produced. With A3 (Formamidinium) being the root of the tree, the selected B site is B3(Tin), and the selected X site is X1 (Chloride). The associated cost for this path is 0.3258 ($/g) of perovskite crystal produced. MATLAB gave the same combinations of ions, and costs, with a relative gap of zero. Figure 9 shows the tree representation with the stared ions being the optimal paths. The model statistics for this case are shown in Table 4.

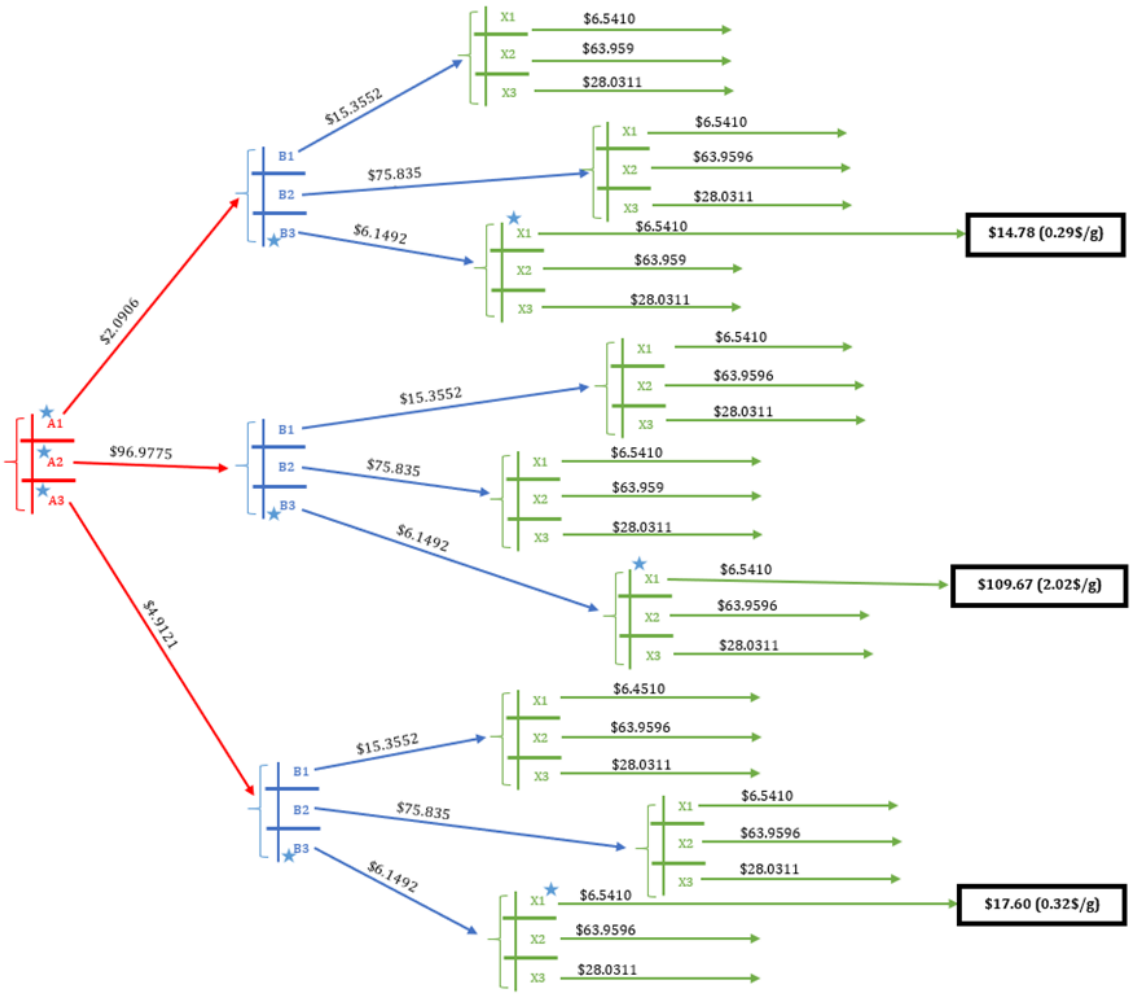

Figure 9. Tree Structure Depicting the Optimum Path Solution for the Three Ions in Case Study.

Table 4

GAMS Model Statistics for Case Study #1

Model statistics	Values		
	Root, A1	**Root, A2**	**Root, A3**
Equations	22	22	22
Variables	18	18	18
Discrete variable	7	7	7
Relative gap	0	0	0
Solution time	0.047 sec	0.062 sec	0.060 sec
Solution	0.2874 ($/g)	2.0222 ($/g)	0.3258 ($/g)

3.5.2 Case Study #2

For Case study 2, the minimum cost was found to be a value of 0.1784 ($/g) of perovskite crystal produced. This value corresponded to a perovskite combination of Ammonium for site-A, Magnesium for site-B, and Formate for site-X. Table 5 shows the model statistics for the second case study. MATLAB also gave the same cost of 0.1784 ($/g), with the same ions, and relative gap of zero.

Table 5

GAMS Model Statistics for Case Study #2

Model statistics	Values
Equations	54
Variables	82
Discrete variable	39
Relative gap	0
Solution time	0.187 sec
Solution	0.1784 ($/g)

The second-best perovskite crystal for this case study was hydroxylammonium-tin-sulfur, with a cost of 0.2209 $/g. This corresponded to a 19.24% increase in the optimal cost. The third best crystal was ammonium-lithium-formate, with a cost of 0.2627 $/g. The percentage difference between this cost and that of the optimal was 32.09%. Metal halides perovskites are one of the emerging alternatives for solar energy harvesting among the photovoltaics. Much attention has been dedicated recently in identifying other combinations that will increase the current power efficiency of 23.7%. It is possible that a combination of ammonium and its derivatives with anions, other than halides, can give solar cells with higher conversion efficiencies and stability. Thus, this work presents the opportunity to further extend experimental research to our generated possible combinations. A comparison of the second and third best scenarios to the optimal for case study #2 is shown in Table 6.

Table 6

Comparison of the Second and Third Best Case Scenarios to the Optimal for Case Study #2

Case	Combination	Cost ($/g)	Difference (%)
1st Best (Optimal Case)	Ammonium-Magnesium-Formate	0.1784	---
2nd Best Option	Hydroxylammonium-Tin-Sulfur	0.2209	19.24
3rd Best Option	Ammonium-Lithium-Formate	0.2627	32.09

3.5.3 Case Study #3

For case study 3, the cation A was restricted to cesium, while maintaining all other ions for cation B and anion X the same as case study 2. The cost of this perovskite crystal was 21.84 ($/g). This cost resulted in a perovskite crystal made up of cesium for Cation A, magnesium for Cation B, and formate for X. This high cost was due to the high cost of a 99.98% pure cesium in 1-gram ampoules. Table 7 shows the model statistics for case study 3. MATLAB also selected the same ions, at the same cost.

Table 7

GAMS Model Statistics for Case Study #3

Model statistics	Values
Equations	40
Variables	54
Discrete variable	25
Relative gap	0
Solution time	0.063 sec
Solution	21.84 ($/g)

Cesium-based perovskite crystal is also on the rise in recent years. Research has been conducted in adding cesium to site-A cation to improve stability, reproducibility, and efficiency [33], [35], [37]. Since this combination has shown an increase in stability and efficiency, it is possible that perovskites of cesium with other alternatives for site-B and site-X ions would further increase stability and help in the commercialization of the perovskite solar cells (PSCs). It is also possible that with cesium being the site-A cation, multiple ions for site-B and site-X can give a much-improved PSCs ($CsB_yB'_{1-y}X_iX'_{1-i}$). Therefore, much attention should be directed toward this area of research. Cai et al. (2016) [89] predicted the levelized cost of energy (LCOE) of perovskite module to be between 3.5 to 4.9 cents/kWh. Also, Chang et al. (2017) [90] reported the manufacturing cost of 107 $/m2. Song et al. (2017) [91] also reported an LCOE of 4.93 to 7.90 cents/kWh. Li et al. (2018) [92] performed a cost analysis for the manufacturing of a perovskite solar cell. In their analysis, they used a perovskite crystal cost of 700 $/kg (0.7

$/g), 450 $/kg (0.45 $/g), and 400 $/kg (0.4 $/g). As stated earlier in our assumptions, the cost analysis was only made for the perovskite absorber the goal is to expand the search for cost effective perovskite crystals that satisfies the Goldschmidt and octahedral tolerance factors. It can be noted that only case study 3 and root-A2 scenario in case study 1 had values greater than that presented by Li et al. (2018) [92].

With more emphasis on global sustainability, the need to drive processes towards a more sustainable and cleaner pathway has become paramount in the design of new and emerging alternatives to already existing processes. With the application of systems engineering, processes can now be implemented with a higher surety of sustainability. If there is a breakthrough in the solar energy field for perovskite crystals with higher solar energy conversion efficiencies, a more sustainable way of harnessing the sun's energy could be achieved.

3.6 Conclusion

The work presented here, facilitates the identification and selection of innovative materials for each designated site A, B, and C in the perovskite crystal, taking into account crucial criteria such as stability and economic viability. This approach pivoted on the foundational principle of selecting an individual material based on its ability to provide both stability and affordability, a strategy applied uniformly across all three sites.

The first case study opted for a uniform choice of cation B and anion X for every variant of cation A under study. This consistent selection strategy laid a structured foundation for the experiment, ensuring that the variables remained controlled and allowing for a focused analysis on the effects of the different cation A choices. In diving deeper into the initial methodology, it emerged that the optimum perovskite crystal combination could be

achieved through a combination of ammonium-magnesium-formate at a cost of 0.1784 ($/g). This combination gave a best solution in both stability and cost feasibility, costing a mere 0.1784 dollars per gram, presenting itself as a cost-effective solution. In the cesium case, the selected site-B cation and site-X anion were magnesium and formate respectively, with a cost of 21.84 ($/g). Both GAMS and MATLAB selected the same combinations in each case study.

To sum up, this work has successfully presented a pathway to select a single, most appropriate material for each specified site, A, B, and X, based in an analysis of stability and cost parameters. This study helps in fine-tuning the methods for choosing the right materials carefully. It sets the stage for upcoming projects to build on this research. It also encourages more discoveries in finding cost-effective and stable materials for perovskite crystal synthesis. To this end, the next chapter revisits the second domain of this research, focusing on optimizing flushing operations in lube oil industries. It provides a detailed exploration of current packaging operations and proposes alternative solution strategies to enhance efficiency.

Chapter 4

Optimization of Flushing Operations in Lube Oil Industries: Studies of Existing Packaging Operations and Alternative Solution Strategies

4.1 Overview

In a typical lubricant manufacturing facility, the production process is complex and comprehensive. It initiates at the feed tanks located in the tank farm, progresses into the blending room where different product formulations are created by combining basestocks with functional additives in blending vessels. Finally, it extends to the packaging station, where the finished products are packaged in various containers such as bottles, pails, and drums. Lubricating oils find diverse applications across various industries, and based on their intended use, they can be broadly categorized into several types: (i) Engine oils (for petrol and diesel engines, aircraft, and marine engines), (ii) Turbine oils, (iii) Gear oils, (iv) Quench oils used in metalworking, (v) Insulating oils, (vi) Chain lubricants, and (vii) Hydraulic oils. Each of these oil types possesses unique characteristics that require separation to uphold stringent quality standards [56]. Consequently, it is crucial to thoroughly clean the system before starting the blending and packaging operations for a different product batch to prevent any potential cross-contamination. The production network spans from the initial stages of vessel mixing, encompasses the various process equipment used, and concludes in the final filling of containers for distribution to customers, which could include plastic bottles, pails, or drums. This network often comprises numerous twists and turns, typically involving 45° and 90° angles, and the product may traverse through flow meters, filters, pressure regulators, and other process instrumentation or metering devices. This inherent complexity in the network makes it

challenging to achieve thorough cleaning. Consequently, existing flushing methods may prove insufficient for completely removing residual products left over from previous production runs.

The main goal of this project is to introduce advanced process improvement strategies and methods to boost the effectiveness of cleaning processes during production changeovers and thereby improve the operational efficiency at lube oil blending plants, in partnership with our associated industry. Figure 10 illustrates a computer aided design (CAD) of the multiproduct pipeline system within a drum packaging station in a generic lube oil manufacturing facility.

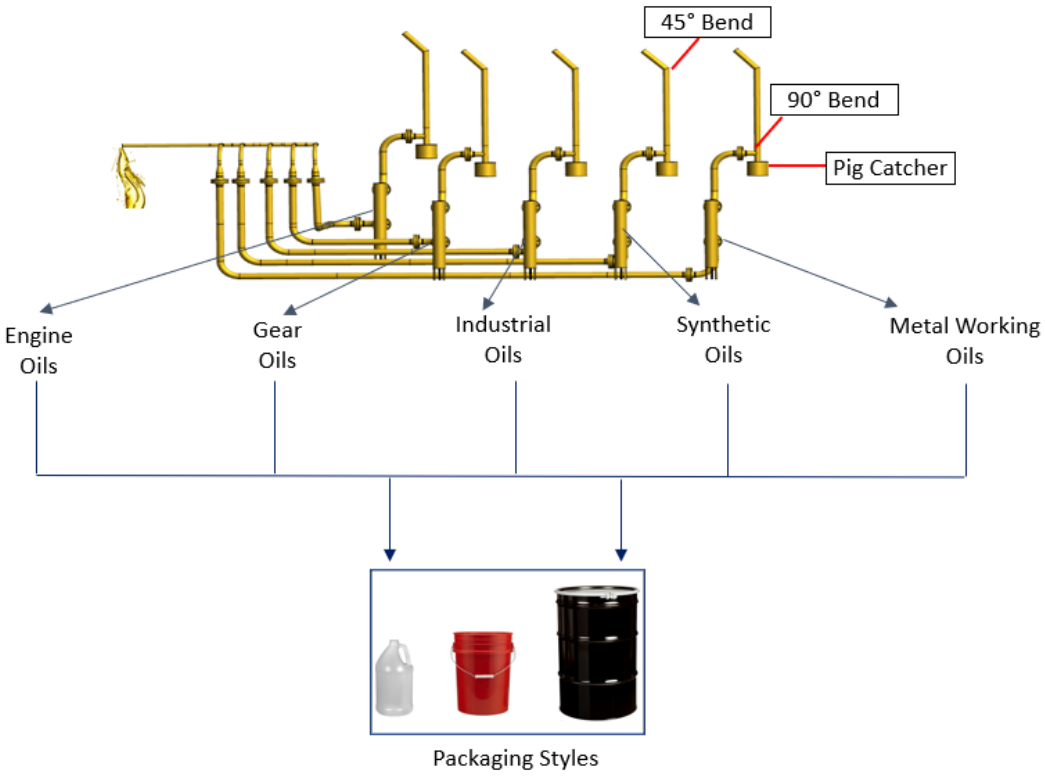

Figure 10. Computer Aided Design (CAD) of a Packaging Station from a Multiproduct Pipeline System within a Generic Lube Oil Blending Facility.

The piping between the storage tanks and the Drum fill line equipment can be cleaned using a pigging device. These devices cannot be used in piping with fittings and bends. So, the end of this straight pipeline is at the pig catcher shown on the right side of Figure 10. More information on the pig catcher and the pigging technique is discussed in the following section.

4.1.1 Pipeline Pigging

Lubricant industries are progressively adopting 'pigging technology' for liquid product recovery. Within the lube oil sector, pigging systems utilize a distinct device known as a 'pig' to retrieve leftover liquid from pipelines [93]. This particular tool, a polymeric 'pig', is named for the unique squealing noise it produces while moving through the pipelines. Historically, the name 'pig' transformed into an acronym for 'pipeline inspection gauge'. Driven by compressed air, the pig serves as a scraper, sealing against the inner surfaces of the pipes and efficiently clearing oil residues [94]. The compact nature of the pig allows it to push the leftover product to its intended location, typically a storage or feed tank, as shown in Figure 11.

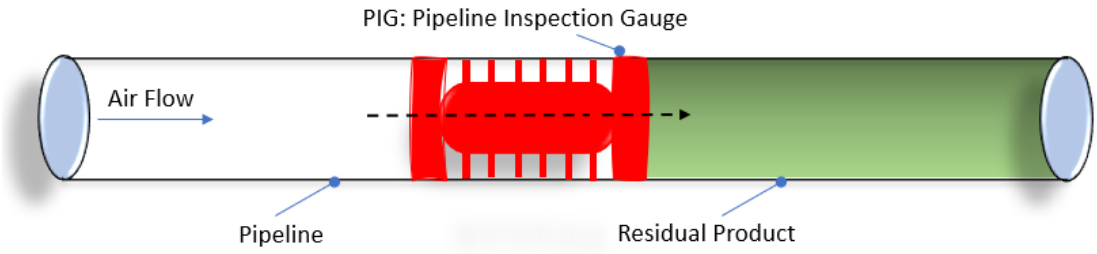

Figure 11. Lube Oil Pipeline Cleaning Tool: Pipeline Inspection Gauge (PIG)

Crucially, pigging technology helps recover products that would otherwise be discarded, resulting in significant benefits and savings. Apart from the lube oil sector, industries like food, beverages, confectionery, household items, cosmetics, personal care, pet food, paint, and coatings also employ pigging in their production processes [95]. By extracting residual liquids from pipelines, pigging systems substantially boost product yields. The recovered product remains of high quality, identical to the product being processed, rather than being downgraded. In the absence of pigging, this product would be either wasted or repurposed for a lesser quality product during transition processes [96]. However, there is a notable challenge: the inflexibility of these polymeric pigs. They struggle with pipelines of differing diameters, can't handle sharp 90° bends, turns, or auxiliary equipment like filters. To cleanse parts of the system inaccessible to the pigs, a flushing oil technique is employed. This oil, a product from an upcoming batch, is used to clean residues of the previous batch. This action produces a mixed oil / commingled oil, not meeting the standards of either batch, resulting in a downgraded product of diminished economic value. Importantly, instead of sending product to waste, pigging recovers it. So, the benefits and savings from pigging are significant. In addition to lube oil industry, other industries that use pigging technology during their production process include food, beverages, confectionery, household liquids, cosmetics, personal care, pet food, paint, coatings and many others. By recovering the residual liquid product from the pipe, pigging systems are an extremely effective way to increase yields. The reclaimed product is perfectly saleable product. It’s in the same condition as the rest of the product being processed, and It’s not been downgraded. But, without a pigging system, this product would be sent to waste, or for use in a downgraded product, during the changeover process.

However, a significant limitation arises from the rigidity of these polymeric pigs, preventing them from navigating through variable diameter pipelines, negotiating 90° bends, handling turns, or dealing with ancillary equipment like filters. As a solution to clean the remaining sections of the system, a method involving the use of a flushing oil is employed. This flushing oil is a finished product from an upcoming batch, utilized to cleanse any residues of the preceding batch. This practice results in the creation of a mixed or commingled oil that does not adhere to the specifications of either of the two batches, and as a consequence, it is classified as a downgraded product having a significantly low economic value as compared to the pure product.

4.1.2 Filtration

In the lube oil industry, utilizing filters is pivotal in maintaining the high standards of purity, quality, and performance of the oils, thereby fulfilling customer expectations [97]. Figure 12 illustrates the bag filters of conventional designs that are currently used at these facilities. These filters are included in the system to eliminate various contaminants such as dust, metal particles from pipeline wear and tear, and rust

Figure 12. Bag Filter and Filter Housing Utilized in Lube Oil Industries (Source [98])

Bag filters are commonly employed in the lube oil sector and other sectors involving fluid processing, serving a critical role in eradicating contaminants and securing the purity and high quality of the final products. These filters encompass several key components including a robust housing to secure the filter bags, the filter bags themselves which are central to the filtration process, and inlet and outlet ports for the fluid. The filter bags, available in diverse micron ratings, facilitate the removal of particles of various dimensions. Regular monitoring and changing of these filters are vital to sustain the efficacy of the filtration process, aligned with adherence to environmental norms during the disposal phase. One prominent downside of traditional bag filter designs is the substantial oil retention in the expansive design of the housing, leading to a considerable

hold-up of oil. This, coupled with the frequent necessity for manual changing of the filter bags, not only elevates labor demands but also triggers operational downtimes. In line with our principal objective of minimizing the amount of downgraded oil during transitions in production, we are setting forth to investigate contemporary and more compact filter designs. Our aim is to significantly diminish hold-up volumes, thereby reducing the downgrading of oil during changeovers.

4.1 General Improvement Methods

Through a comprehensive analysis of existing literature, we explore innovative strategies and general enhancements aimed at minimizing product downgrade during changeover operations in multiproduct pipelines.

4.2.1 Gel Pigs

We are considering replacing the current rigid polymeric pigs with more adaptable materials such as gel pigs, which would facilitate their passage through pipelines with varying diameters, consequently reducing the necessity for flushing [63]. These gel pigs, characterized by their high viscosity, function more like fluids than solid substances. Their working principle involves forming a high viscosity plug that establishes a firm seal against the pipeline walls, effectively cleaning the pipe surfaces [64]. A notable benefit is their resistance to breaking down under the pressure exerted by the compressed air used to propel the pigs. Leveraging their fluid-like nature, gel pigs can navigate bends, turns, and sections of pipelines with uneven diameters with ease.

4.2.2 Pipeline Coatings

Omniphobic (Omni: all, phobic: repellent) coatings are gaining attention due to its ability to repel almost all types of liquids from its surface [99]. These surfaces force the liquid to form droplets that do not wet the surface. Consequently, they can repel almost all types of liquids reducing cleaning problems and time spent in cleaning operations [100]. Applying these kinds of coatings to lube oil pipelines can diminish the amount of oil retained in the system, thus decreasing the need for extensive flushing [101], [102]. Beyond this application, these surfaces have broader utilities encompassing automotive and marine sectors, as well as serving de-icing and anti-fouling functions in the oil & gas, chemical, and transportation industries.

4.2.3 Fluid Blasting

This advanced technology involves blasting the pipelines using either water or any other liquid at very high pressure (up to 20 kpsi) [103]. In this technique, the liquid is introduced in the inner walls of the pipelines utilizing high-pressure jets with suitable nozzles. The jet is created by forcing liquid through a nozzle at high-pressure. After spraying the walls this fluid, typically water must be removed by a drying process. Fluid blasting has the potential to serve as an efficient and versatile solution in maintaining the cleanliness and functionality of pipelines, especially in the lube oil industry. It not only ensures the removal of undesirable substances from the pipelines but also promotes the longevity and efficient operation of the systems. However, careful consideration must be given to the process parameters to avoid any damage and to ensure environmental compliance.

4.2.4 Vibration Cleaning

Vibration cleaning is a process that leverages mechanical oscillations to dislodge and remove unwanted deposits and accumulated materials from the inner walls of pipelines [104]. It is sometimes used in industries to maintain pipeline efficiency and safety. A vibrator fixed directly on the machinery wall operates in a frequency range of 20 – 50 kHz, creating standing waves in the fluid [105]. These standing waves induce the formation of cavitation bubbles in the fluid, which are essentially voids or bubbles that are formed at low pressure regions [106]. The cavitation bubbles collapse once they move to high-pressure regions, releasing substantial energy capable of dislodging solids and foul materials attached to the machinery or pipeline walls. Vibrator-induced cavitation presents an approach to maintaining cleanliness in industrial pipelines, ensuring operational continuity and efficiency. This methodology, proven by research and practical applications, has been demonstrating notable effectiveness in dislodging solids and mitigating fouling, promoting a cleaner and more efficient operational environment. However, care must be taken to manage the potential stress induced in the equipment due to long-term vibration.

4.2.5 Alternative Filters

In the conventional setup, bag filters have been employed in the pipeline system to eliminate solid impurities potentially present in the final product [97]. The current configuration which houses these bag filters in a metallic enclosure tends to retain a substantial amount of fluid, posing challenges in holdup. Moreover, the necessity for manual upkeep can lead to interruptions in operations. A potential alternative to this

traditional setup is the integration of inline welded filters with more compact designs as illustrated in Figure 13.

Figure 13. Inline Welded Filters (Source [107], [108])

These filters are seamlessly incorporated into the pipeline of the fluid system through welding, creating a secure and leakage-resistant junction. Their capability to handle high-pressure scenarios stems from the resilient welded junctions that are superior to other forms of connections, offering enhanced longevity even in rigorous operational environments. Additionally, inline welded filters stand as space-efficient solutions compared to the bag filters housed in bulkier setups. They promise consistent functionality across varying pressures and temperatures, providing dependable filtration amidst unstable operational dynamics. In summation, inline welded filters present a series of benefits over their bag filter counterparts, including better leak resistance, expanded durability, improved filtration precision, and diminished maintenance demands. These merits position inline welded filters as the potential choice in circumstances that prioritize safety and

efficiency at high thresholds. A summary of the potential alternative technologies and improvement methods along with their pros and cons are discussed in Table 8.

Table 8

List of Potential Technologies and their Description

Potential Technology	Industrial Scale-up	Relative Cost	Relative Time Necessary	Pros	Cons
Gel Pigging	Yes	Low	Low	Potentially replace flushing process	Increased operational complexity
Pipeline Coatings	Yes	Moderate	Moderate	Minimize film formation on pipeline walls	Challenge in coating the inner walls of pipeline
Fluid Blasting	Yes	High	Low	Efficient for residue removal More economical and environmentally safe	System must be able to withstand high pressure
Vibration Cleaning	Yes	Low	Low	Non-invasive method	Potential cavitation damage
Inline Filtration	Yes	Moderate	Low	Decreases amount of flush oil required	Disrupting current production process Maintenance and replacement of filters

4.3 Data Analysis

We realized that we had a great opportunity to collect valuable insights through careful data collection and analysis at our collaborative facility. The objective behind analyzing this data was to examine and identify patterns in the slop (commingled/ mixed oil) generated during each flushing operation. This data encompasses a variety of critical metrics such as the current and preceding products in the drum fill, the date of filling, the drumline number, properties like viscosity and density, the volume of fluid flushed (measured in gallons), and the product family classification, among other details. Figure 14 offers a depiction of the collected data set.

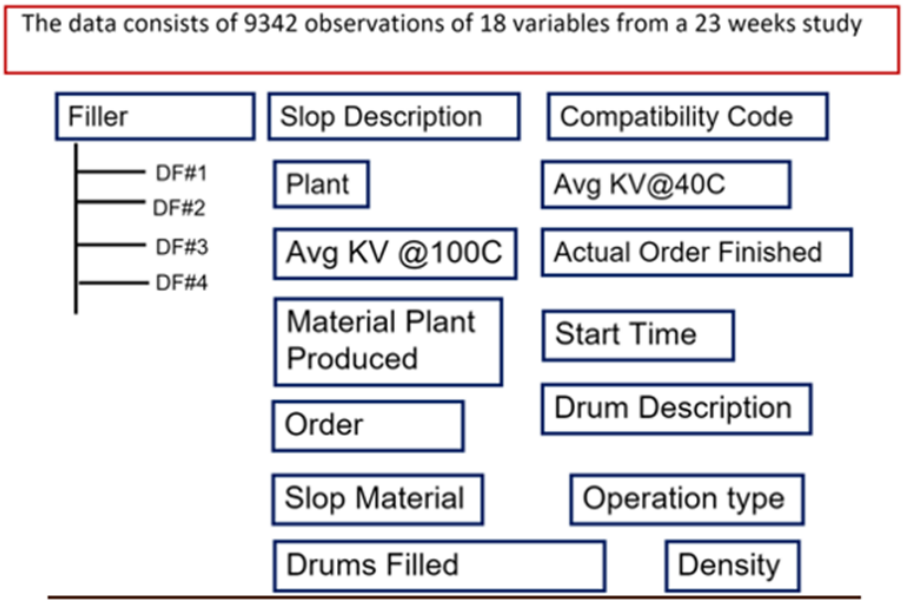

Figure 14. Dataset of Information Collected and Analyzed through the Experiments

We began our analysis by organizing the data based on the time each order was completed and grouping them by their respective product families. Our objective was to identify patterns in the necessary volume of flush required during a changeover within the same product group, such as transitions between different lubricants within the Type-A or Type-B family. The terminology Type-A, Type-B is employed to distinguish between various oil families, with Type-A representing the engine oil family, Type-B representing the gear oil family, Type-C representing the industrial oil family, and so forth. In addition to this, we focused on understanding the range of viscosity within each product family by examining products with the highest and lowest viscosity levels. Next, we took a closer look at scenarios where the changeover happened from a Type-A family lubricant to other types, such as Type-B, Type-C, and so on as illustrated in Figure 15.

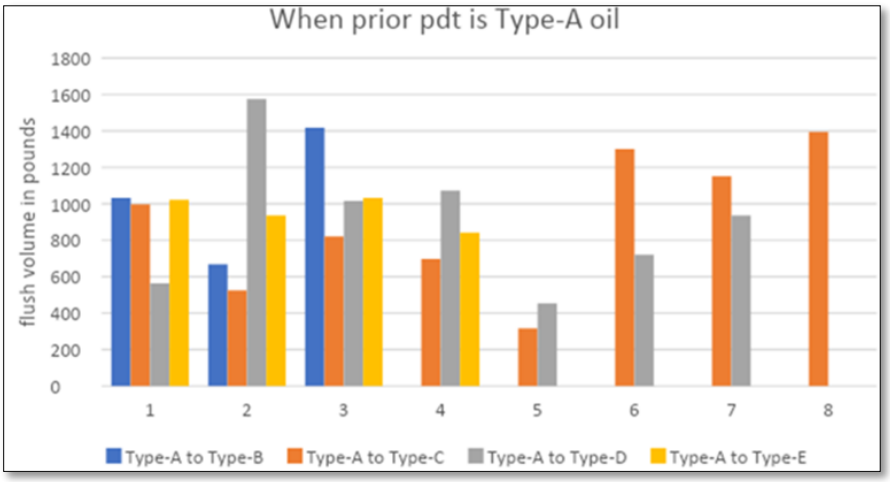

Figure 15. Volume of Flush Generated When a Type-A Family was Changed to Other Families (pdt is used as an abbreviation for product)

Following this, we focused our analysis on observing the volume of the flushing required with respect to several factors, including the viscosity of the residual product, the viscosity of the new product, and the difference in viscosities between the two. We wanted to get a clear picture of how these parameters influenced the fluctuating volumes of flush created during the production process. Our detailed exploration, which is displayed in Figure 16, aimed to find any consistent patterns across various cases. On the first y axis is the flush volume which is given as a blue bar. The gray, orange and yellow bars refer to the second y axis represents the viscosity of the prior product on the drum fill line, viscosity of the current product, and the difference in viscosities of the two products.

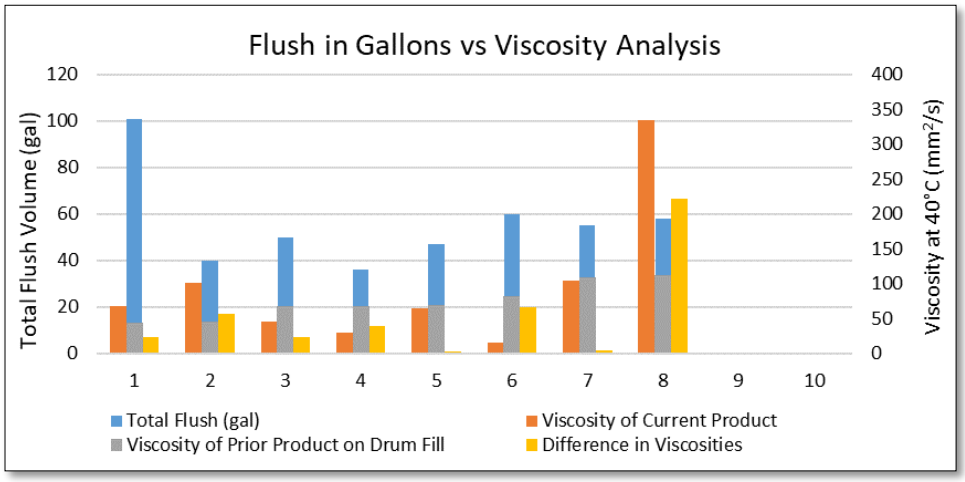

Figure 16. Flush in Gallons vs Viscosity of Prior Product, Viscosity of Current Product and Difference in Viscosities of the Two Products

Unfortunately, despite our efforts, it appeared that there wasn't a defined trend identifiable through the different situations we analyzed. Next, we explored how seasonal changes affect the failure rate. Since viscosity changes with temperature, we were keen to

see how failure rates differed between warm and cold weather. Our findings are shown in the graph in Figure 17. The orange line on the graph shows the average monthly temperature and the blue bars are the proportion of the failed samples. As can be seen from the trend, in the cold months starting in November, the failure rate increases significantly to a maximum failure rate of 21% in February.

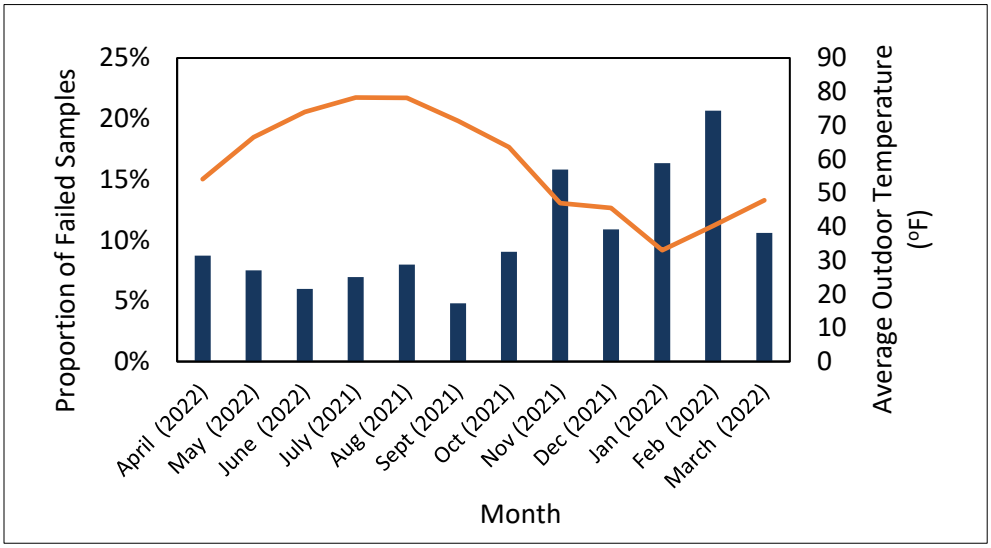

Figure 17. Effect of Seasonal Change on the Failure Rate.

In the warm months the failure rate is less than 10%. To better understand this trend, we transformed this graph from a plot of failures vs the calendar month to a plot of failures vs the average monthly temperature shown in Figure 18. This graph shows a clear trend of failures decreasing with increasing temperatures.

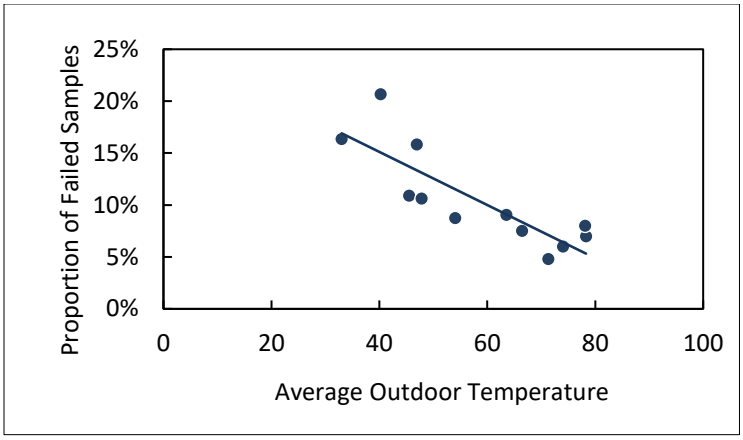

Figure 18. Linear Decreasing Trend of the Proportion of Failed Samples with Respect to Temperature.

To this end, after understanding the existing drawbacks we proceed towards our first solution approach out of the three-pronged solution approach. Chapter 5 entails our experimental studies 1, which involves the development and examination of a benchtop experimental rig.

Chapter 5

Experimental Studies 1: Procedural Enhancements

The inconsistencies observed from the data analysis of the regular flushing operations, paved us to get better insights into the current operational methods by mimicking the industrial set up benchtop plant design and higher capacity pilot plant setups. Our goal was to get an in-depth understanding of the existing procedures, study the drawbacks and develop enhanced operational methods with the help of an experimental approach. To this end, in this chapter, we explain the hands-on method we employed towards achieving the optimization of flushing operations.

5.1 Process Flow Diagram of a Generic Lube Oil Industry

Lube oil enters the pipeline system either from the storage tanks located in the tank farm or from the blending vessels situated in the blending room. The pipeline sections remain straight and can be pigged until they reach the packaging station which involves complex pipe geometry and hence are unpiggable. Figure 19 is an illustration of the unpiggable section from the commercial facility.

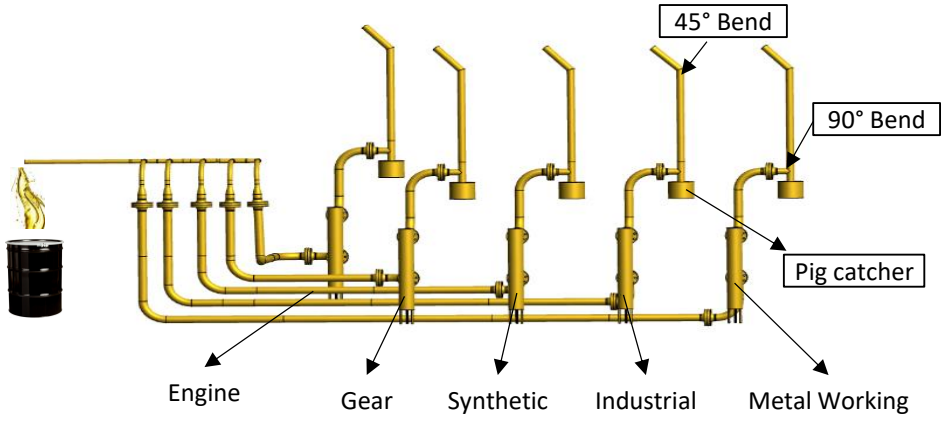

Figure 19. Schematic of the Unpiggable Section of the Multiproduct Pipeline Configuration at the Commercial Lube Oil Facility

The finished lube oils are pumped to the packaging station where they are packaged in bottles, drums, and pails to reach the end users. The small cylinders following the 45° bend shown in Figure 19 is the pig catcher. The pig is passed through the straight pipe sections to scrap the residual oil and clean the straight lines prior to a changeover operation. After the pigging processes is completed, the pig sits in the pig catcher. Immediately following the pig-catching station is a 90° tee bend that leads to the remainder of the pipeline system which is unpiggable. The flushing time and procedure are dependent on the previous experience of an operator in regard to the specific product.

In Figure 20 a process flow diagram of the drum packaging line is shown. This diagram was constructed with reference to the setup at the partnered commercial facility. It includes the important aspects of the drum fill line, such as pressure gauges and the airline.

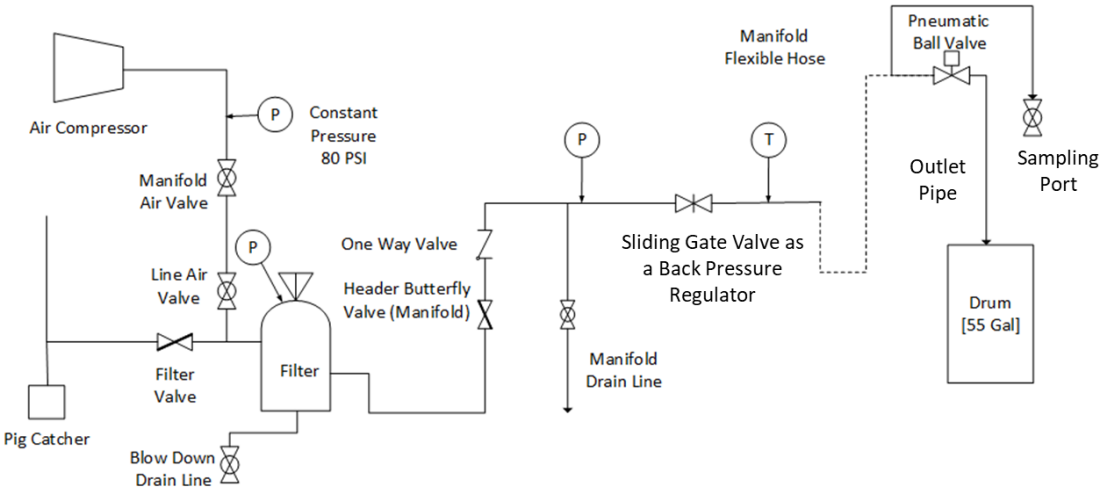

Figure 20. Process Flow Diagram of the Drum Packaging Station at a Generic Lube Oil Facility

The oil enters the system into the filter, which then travels through a U-bend and up through the manifold. Then, the oil travels through the flexible hose and out of the outlet pipe and sampling port. The pipelines are carbon steel 3" nominal size. The volume of the filter is approximately 13 gallons and the total volume of the rest of the system is approximately 32 gallons. Using this process flow diagram, the main configuration of the drum fill line can be determined, and the system can be analyzed for oil holdup and potential improvements. During a product changeover, the first step is using pigs to scrape out excess oil, sending it back to the feed tank. The second step involves gravity draining the filter, then purging it with compressed air for approximately 30 seconds to remove residual oil. In the third step, the rest of the unpiggable section is then gravity drained through the manifold line to remove some of the residual oil trapped within the system. The third step is gravity draining the remaining unpiggable section through the manifold

line to remove some trapped residual oil. However, this method is not entirely efficient, leaving a significant volume of residual oil in the system. Figure 21 illustrates the process flow diagram, with faint red sections indicating cleared lines and deep red sections representing trapped residual oil.

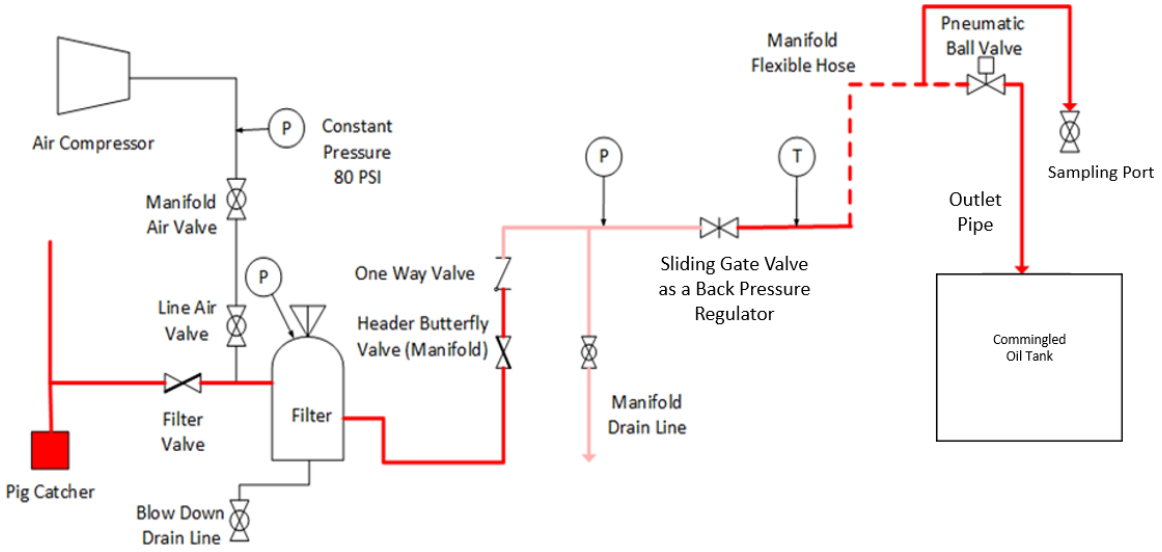

Figure 21. Process Flow Diagram Illustrating the Inefficiency of the Current Draining Method and the Trapped Oil in the System

In the fourth step, the system is then flushed with the incoming oil that is needed to be packaged. At the end of the chosen flush time that depends on the previous experience of the operator and ranges between 60 – 200 seconds, an oil sample is taken at the sampling station and sent to the lab to get it tested for specifications. The preliminary test that confirms the purity of the batch and the success of the flush is the kinematic viscosity of the oil sample at 40 ℃ or 100 ℃. The test is conducted as per the ADTM D445 guidelines and is estimated to take about 20-30 minutes [109]. If the kinematic viscosity falls within the desired range specified for the product, the product is approved for packaging.

However, if the product falls outside of the specifications, then a secondary flush is performed. This process is repeated until the product meets specifications. The amount of flush volume is controlled by the operator at the flushing station. And the commingled product is pumped into a storage tank. The limitations inherent in the current flushing procedures contribute to the high costs associated with the operation. Consequently, in our pursuit of an optimal solution, we have delved into enhanced procedures aimed at more effectively draining the system. The primary objective is to minimize the presence of residual products within the system to the greatest extent possible. By reducing the residual oil content, we anticipate a corresponding decrease in the necessary volume of the subsequent product required for system flushing. The study of the improved procedures was conducted through a benchtop experimental rig that is discussed in detail in section 5.2.

5.2 Benchtop Plant Design

After conducting multiple onsite flushing experiments and developing a process flow diagram of the drum filling line at the partnered facility, we developed a benchtop plant design, shown in Figure 22.

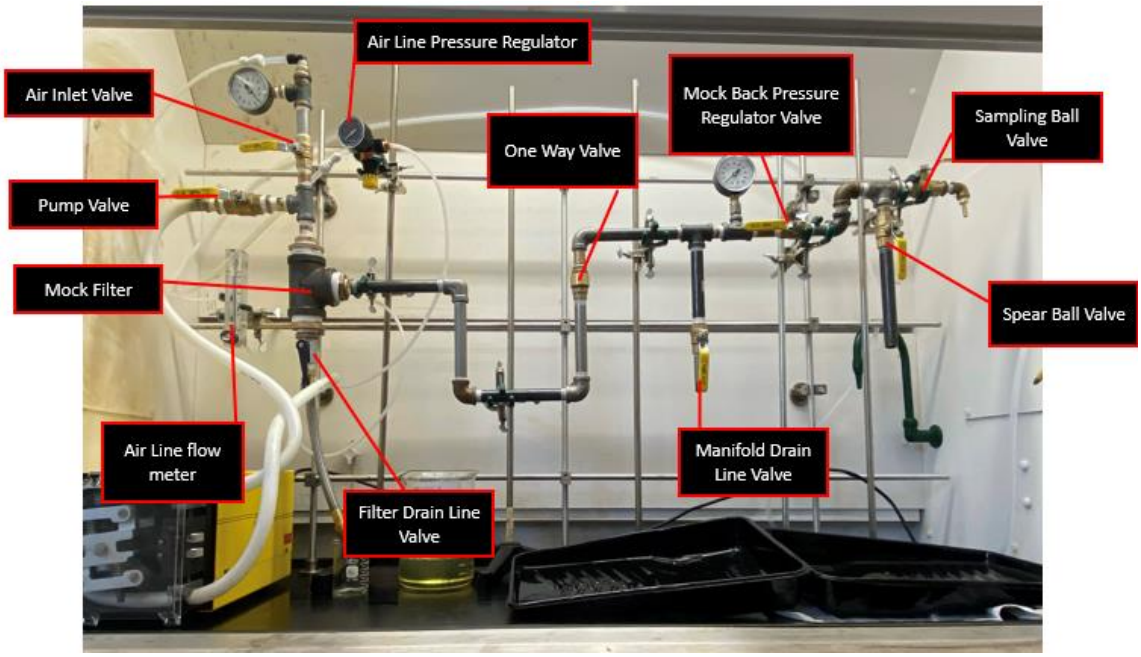

Figure 22. Benchtop Plant Design for Mimicking the Industrial Flushing Operation

This setup was developed to reflect a flushing process more accurately at the drum filling line of the partnered facility, by using the process flow diagram of the plant. In this setup, the filter housing was replicated using a 1½ inch tee, with a bend in the pipe following the filter comparable to that of the drum filling line at the plant. This setup featured a one-way valve in the same location relative to the plant, as well as a drain line and a pressure gauge located on the manifold of the benchtop plant design. Finally, the benchtop features a spear and sampling port at the end of the design where oil samples can be collected. This benchtop plant design was constructed using threaded pipe lengths and Teflon tape to prevent leakage. Additionally, ball valves were placed in the system to replicate the location of valves at the partnered plant. To introduce air into this system, an airline pressure regulator and airline flow meter were utilized to keep the air pressure at

40 psig as well as the air flow rate at 3 scfm. For the current experiments utilizing this setup, a pump speed of 150 RPM was used, which gave a flow rate of approximately 137 mL/s. The main goal of the first set of experiments conducted with this experimental setup was to determine the effect of improved drainage procedure on the volume of oil required to flush the system. Additionally, this set of experiments achieved the goals of determining whether air could be used to clear the oil holdup in the setup and determining whether the oil in the system behaves as a plug.

5.2.1 Flushing Experiments

For the first two experiments, two flushes were performed using a product A and Product B. In these two experiments, both oils were flushed through the system to determine whether the operating procedure that replicated the flushing procedure at the plant was accurate, determine whether the two second sampling rate was acceptable for this setup, and determine how much oil was required to flush the system. These two experiments yielded that the operating procedure was acceptable, that the sampling rate must be increased to one second, and that approximately 1500 mL was required to completely flush the system. Using these results, the next four sets of experiments were developed.

For the next two experiments, the same two flush and residual oils were utilized, and the procedure used to drain the line was same as that at the collaborated facility (Prior Method). For this procedure, the filter was gravity drained and air blown, the manifold drain line was then gravity drained, and then the system was flushed, and samples were collected at equal time intervals. For the second set of two experiments, the same two flush and residual oils were utilized. The procedure used to drain the line was optimized by air

blowing the entire system to clear as much residual oil from the lines as possible (Improved Method). For this procedure, the filter was gravity drained and air blown, the manifold drain line was then air blown, the spear was air blown, and finally the system was flushed at the same pump speed and sampling rate as the prior two experiments. It was observed that when air blowing the system, the drainage technique was highly effective in removing residual oil. The outcomes of both experiment sets are visually represented in Figure 23 and Figure 24. Further specifics regarding the results of both drainage methods for both sets of experiments are provided in Table 9 and Table 10.

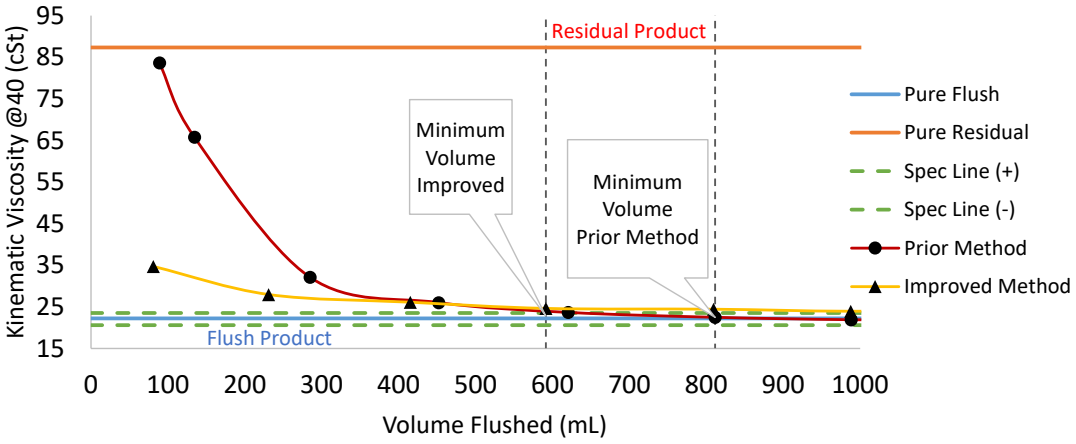

Figure 23. Comparative Analysis of Flushing Methods: Existing vs. Improved - First Set of Experiments

The plot of the volume flushed vs kinematic viscosity for the first set of experiments is illustrated in Figure 23, the kinematic viscosity of the residual oil was 87.36 cSt (represented by the solid red line) and the desired viscosity of the new product was 23.5 cSt (represented by the solid blue line). In the experiments we collected samples at an interval of two seconds and tested them for their viscosities. The dashed green line

represents the desired specification range for the flush oil. When the sample reaches the specification line, it confirms that the required purity level is attained, the flushing can be stopped, and the product can be packaged. As can be seen in Table 9, the minimum volume of flush required for the prior method was 811.6 mL whereas for the improved method, it was 591.5 mL. This illustrates that there was a 27.11% reduction in the required flushing volume.

Table 9

Results for Comparative Analysis of the Existing and Improved Drainage Method for the First Set of Experiments

Method	Mass % Drained from Filter	Mass % Drained from Manifold	Mass % Drained from Spear	Total % Drained	Minimum Volume to Spec (mL)
Prior	41%	11%	0	52%	811.6
Improved	45%	39%	8%	87%	591.5

For the next set of experiments as illustrated in Figure 24, the viscosity of the residual product was 23.5 cSt and the viscosity of the pure flush product was 87.36 cSt. As explained in Table 10, the minimum volume of flush required with the prior drainage method was 525 mL whereas for the improved method it was 232 mL. This means that there was a 55.8% reduction in the required flushing volume.

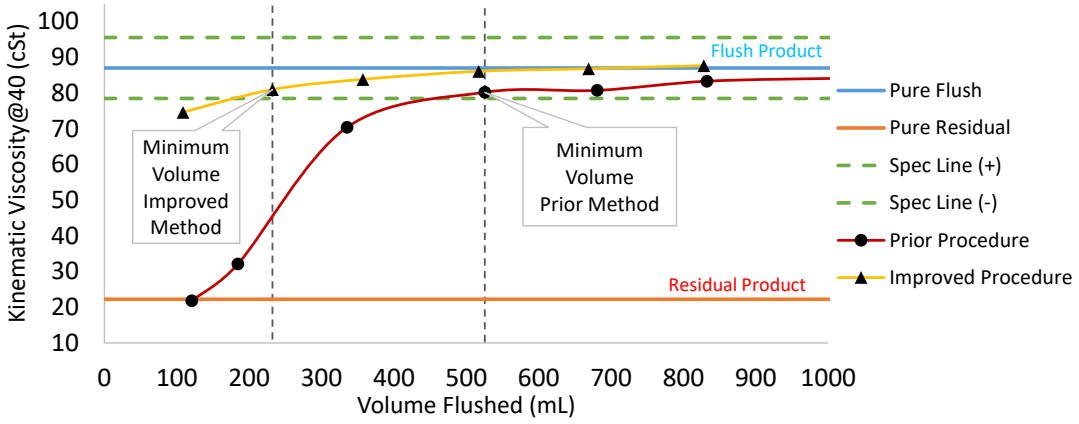

Figure 24. Comparative Analysis of Flushing Methods: Existing vs. Improved - Second Set of Experiments

Table 10

Results for Comparative Analysis of the Existing and Improved Drainage Method for the First Set of Experiments

Method	Mass % Drained from Filter	Mass % Drained from Manifold	Mass % Drained from Spear	Total % Drained	Minimum Volume to Spec (mL)
Prior	45%	16%	0	60%	525
Improved	45%	42%	8%	95%	232

These experiments confirmed that the improved method of drainage was effective in reducing the necessary flushing volume to reach the desired specifications of the new product. However, these experiments were performed in 0.5" nominal pipe size experimental rig. Hence, to confirm that the method would be applicable to 3" nominal pipe size carbon steel pipes at the commercial facility, we conducted at scale experiments

by constructing a Polyvinyl chloride (PVC) experimental rig of 3" diameter. The details of these experiments are discussed in section 5.2.2.

5.2.2 At Scale PVC Pipe Experiments

To test whether the improved drainage technique developed using the benchtop pilot plant can be applied to plant scale with the same level of drainage in low sections of the plant such as a U-bend, we developed a rig constructed of 3" PVC pipe to test how well varying fluids can be air blown out of 3" pipelines and bends. The finalized rig which was used for experimentation is shown below in Figure 25.

Figure 25. At Scale Experimental Setup

The goal of the experiment was to understand how well different types of fluids were able to be cleared out of a U-bend in a 3" pipeline using compressed air at differing

flow rates and air pressures to simulate how effective the air blowing procedure would be at the industrial scale. Initially, water was used to fill up the pipeline to test how effective different flowrates and air pressures were to clear out the water from the system. Then, we used an 83 wt% 75 cSt Glycerin mixture with water to more accurately represent how a typical range of viscosity of oil would be removed from the U-bend when air is blown through. The results of both the water and glycerin system drainage can be seen in Figure 26 and Figure 27.

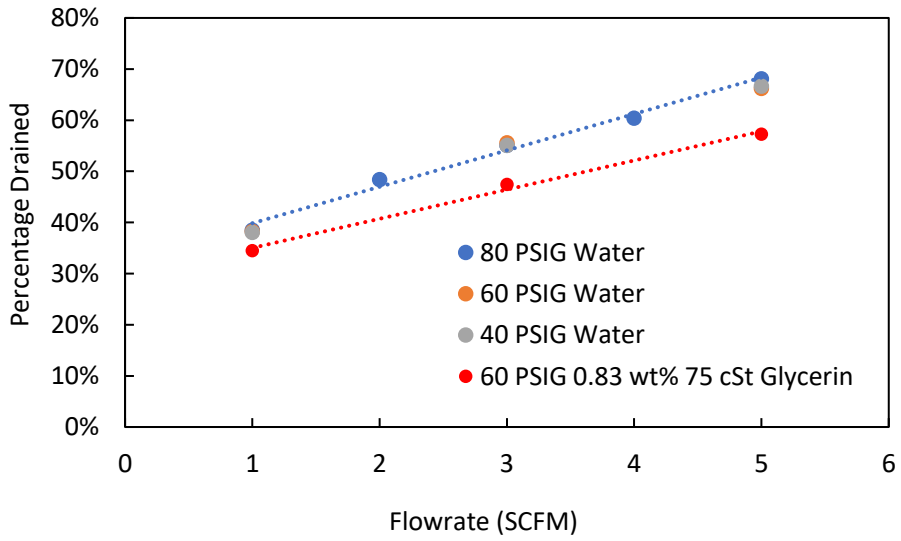

Figure 26. Drainage of 83 wt% 75 cSt Glycerine at 60 psig

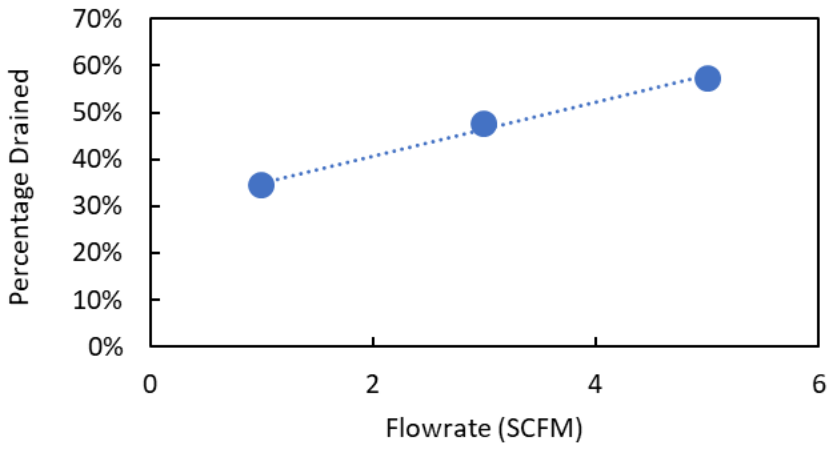

Figure 27. Overall Results for the Drainage of Water and Glycerin at Varying Flowrates

Through these set of experiments, we studied that increasing flowrate results in an increase in the fluid removed. However, air pressure did not have a large impact on the effectiveness of the drainage of the system. The volume of the fluid removed was inversely proportional to the viscosity of the fluid. We also studied that low flowrates of air may not remove all of the residual fluid from the system. Furthermore, at a flowrate of 5 SCFM, air blowing the pipeline can remove up to 60% of the residual fluid from the U-bend. Therefore, we concluded that at the collaborated facility, the air blowing procedure would be greatly effective in removing most of the residual oil from the pipelines, including the U-bend, given that the facility uses an air flowrate higher than 5 SCFM. We then conducted onsite flushing experiments to test out the improved procedure with air blowing at the plant scale, which is detailed in the following section.

5.2.3 Implementation of the Enhanced Procedure at the Collaborated Facility

We collaborated with operators, chemists, plant engineers, and managers to evaluate the process scale up to plant scale production with consideration of cost, safety, and workability. We successfully executed a HAZOP study, devised a standard operating procedure, and conducted thorough training sessions for plant operators, leading to process change implementation. Our goal was to determine the efficacy of the improved procedure at the commercial scale. This was accomplished by documenting 83 flushes via the improved drainage method and comparing the flushing failure rates with the prior and the improved method. A lower percentage of failed flushes using the improved procedure compared to flushed documented in the plant data statistically proved that the improved drainage technique significantly reduces the amount of residual oil left in the line prior to charging and thus the number of failed flushes. Currently, there have been a total of 83 documented flushes conducted with the improved procedure, and out of these 83 flushes there have been only 3 documented failures. Based on this sample size, there has been a significant decrease in the number of flushing failures using the improved procedure. The failure rate with the improved procedure has reduced to 3.6 % as compared to the traditional flushing procedure which results in an 11 % failure rate. It was also observed that using the improved procedure results in less pure flush oil being required to flush the drum filling line in a changeover. Considering these two developments the plant representatives, including the plant manager, decided to officially standardize this improved flushing procedure at the plant scale for their drum filling line operations. Additionally, in the near future this improved procedure will be standardized plantwide. The projected cost savings for the implemented improved procedure is explained in section 5.2.3.

5.2.3 Projected Cost Savings

The cost savings estimate is based on comparing past flushing operations to the enhanced flushing procedures. Our analysis factored in the yearly production capacity and the expected market price per gallon of the product. We also considered the operational downtime caused by unsuccessful flushes. The total cost of the process was calculated by assessing savings in product volume, reduction in downtime, labor costs, material cost for testing, and overhead expenses. No new equipment was required for the improved procedure, which eliminated capital costs. Additionally, utility costs were not considered in this analysis.

Considering,

a) Number of annual flushing operation, $\#F_T$ = 1500
b) The total failure rate as per the plant data analysis owing to the existing flushing operation, R_{OLD} = 11%
c) The total failure rate per the improved procedure (based on 3 failures out of 83 flushes), R_{NEW} = 3.6%
d) Downtime for a single failed flush, T_D = 40 mins (0.67 hr)
e) Volume used per flush, V_F = 60 gal
    a. For a failed flush, total volume, $V_F = 2 \times 60 = 120$ gal
    b. Extra flush volume, $V_{EF} = 60$ gal
f) Product selling price, SP = $ 12 / gal
g) Labor cost, CLB = $ 30 / hr
h) Cost of Heptane = $ 45 / L.
    - Approximately 100 mL of Heptane is used to clean the viscometer after every test
    - Cost per viscometer cleaning, C_C: $4.5
    - Considering a particular changeover operation, where the sample fails to meet the required specification, cleaning is repeated twice assuming the product passes on the second test.

Number of Failed Flushes Annually

Existing flushing operation, $N_{OLD} = F_T \times R_{OLD}$

$$N_{OLD} = 1500 \times \frac{11}{100} = 165 \text{ flushes}$$

Improved flushing operation, $N_{NEW} = F_T \times R_{NEW}$

$$N_{NEW} = 1500 \times \frac{3.6}{100} = 54 \text{ flushes}$$

Annual Extra Flushing Volume

Existing flushing operation, $V_{EF,OLD} = N_{OLD} \times V_{EF}$

$$V_{EF,OLD} = 165 \times 60 = 9900 \text{ gal}$$

Improved flushing operation, $V_{EF,NEW} = N_{NEW} \times V_{EF}$

$$V_{EF,NEW} = 54 \times 60 = 3240 \text{ gal}$$

Annual Recorded Downtime

Existing flushing operation, $T_{D,OLD} = N_{OLD} \times T_D$

$$T_{D,OLD} = 165 \times 0.67 = 111 \text{ hr}$$

Improved flushing operation, $T_{D,NEW} = N_{NEW} \times T_D$

$$T_{D,NEW} = 54 \times 0.67 = 36 \text{ hr}$$

Product Volume Cost Savings, V_S

$$V_S = (V_{EF,OLD} - V_{EF,NEW}) \times (SP) = (9900 - 3240) \times (12) = \$\,79,920.00$$

Labor Cost Savings, LBCS

$$\text{LBCS} = (T_{D,OLD} - T_{D,NEW}) \times (CLB) = (111 - 36) \times (30) = \$\,2{,}250.00$$

Overhead Cost Savings, OCS

$$\text{OCS} = \text{LBCS} \times 2.2 = 2{,}250 \times 2.2 = \$\,4{,}950.00$$

Material cost savings, MCS

$$\text{MCS} = (N_{OLD} - N_{NEW}) \times C_C = (165 - 54) \times (4.5) \times 2 = \$\,999.00$$

Total Process Cost Savings, TCS

$$\text{TCS} = V_S + \text{LBCS} + \text{MCS} + \text{OCS}$$

$$\text{TCS} = \$\,79,920.00 + \$\,2{,}250.00 + \$\,4{,}950.00 + \$999.00 = \$\,88{,}119.00$$

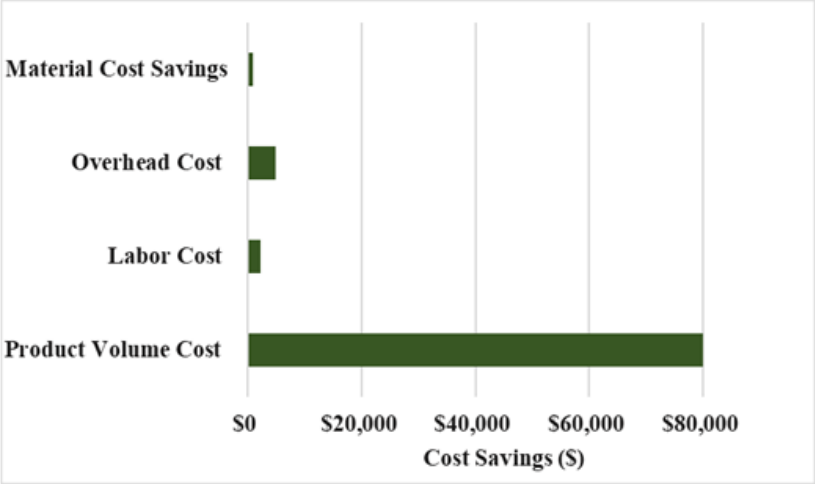

Figure 28. Projected Cost Savings from the Improved Flushing Procedure

The total cost savings with the implementation of the improved drainage method was projected as $88,119/ yr.

Continuing our research, we recognized the significant influence of flow regimes on the efficacy of flushing operations. Hence, our subsequent initiative involved the development of an advanced pilot plant equipped with a more robust pump and a higher-capacity storage tank to explore flushing operations at various flow rates to study the laminar and turbulent flow regimes. Additionally, we aimed to understand the efficiency

of real-time viscosity measurement by incorporating an inline viscometer, with the objective of mitigating the process downtime associated with conventional sampling methods. Further insights into the development of the pilot plant are thoroughly presented in Chapter 6.

Chapter 6

Experimental Studies 2: Pilot Plant Development

The principal objective of the pilot plant was to explore the importance of fluid hydrodynamics through the reduction in scale from the industrial operation. This involved the precise assessment of the impact of variations in process parameters, including flow rate, viscosity, and temperature. To achieve this, a laboratory-scale pilot plant was engineered to replicate the industrial process, with a focus on investigating necessary improvements related to flow rates and flow regimes.

6.1 Pilot Plant Design and Development

The pilot plant used in this work was constructed using scaled down calculations from the partnered facility. Two scale down factors were used to approximately size the components installed in the pilot plant. The first of these factors is a dimensionless number scale down based on the straight pipe Reynolds number for a series of flushes. The second factor is a volumetric ratio between the total volume of the unpiggable section of pipeline and the filter. An accurate representation of the pipeline was developed in our lab by balancing these two criteria. The flow of simulant fluid through the pilot plant and the design process for the scale down of the system is discussed in the following sections.

6.1.1 Reynolds Number

An appropriate scale down factor must be chosen when designing a pilot plant to mimic the characteristics of a much larger operation. In this work, a dimensionless number was a clear choice for our design. Because this project focuses on the mixing properties within sections of pipeline, the Reynolds number for the system was used to scale the

system down. The Reynolds Number for an incompressible fluid can be calculated using equation (13)

$$N_{Re} = \frac{Dv\rho}{\mu} \tag{13}$$

Where: N_{Re} – Reynolds Number, D – Pipe Diameter, v –Flowrate, ρ –Density, and μ –Dynamic Viscosity

(a) Line Diameter: At partnered facility, the internal diameter of the pipeline can be broken up into two sections. The first section which runs from the external tank to the manifold connection is constructed of 3" schedule 40 carbon steel (ID: 3.068"). The second, significantly shorter length, is 2" schedule 40 carbon steel (ID: 2.067"). The volumetric flow achieved by the selected pump determined the internal diameter of the tube.

(b) Product Viscosity: The viscosity of the product is a key aspect in determining the behavior of the product changeover. Not only this affects the Reynolds number, but also the quantity of product remaining within the system. Because the pilot plant is operated at room temperature, the product viscosity must be corrected to account for the elevated temperatures shown at scale.

(c) Volumetric Flowrate: The volumetric flowrate of the system is one of the most critical aspects of the pilot plant. Selection of the pump that will provide the proper flow characteristics is paramount in emulating the design of the at scale operation.

6.1.2 Volumetric Ratio

The second metric that was used in our scale down process is the system volume ratio. This ratio is defined as the volume of the filter by the volume of the remaining system. Accurately recreating this ratio was critical to the design of our system. The system was

modelled by theorizing to be a combination of plug flow and well mixed chambers. The filter acts as a well-mixed chamber with an initial concentration, and the pipe sections act as a plug flow chamber. This volume was determined by slowly filling the plant scale line with fluid and recording the corresponding drop in fluid from the filling tank. The system volume at the partnered plant was determined to be approximately 32 gallons, with the filter containing 13 gallons of product. With these parameters measured, the ratio of the filter to the system is calculated to be one part filter to 2.5 parts system.

6.1.3 Finalized Design

When deciding on a finalized design there were several limitations that determined the products that could be utilized. The first design limitation was based on the tube diameter that could be used owing to the restricted available lab space. The maximum tube diameter for our project was ¾" OD. The minimum tube diameter was set at ¼" OD, as any smaller than this size would require an excessive length of tubing to achieve a similar system volume.

The development of the pilot plant can be divided into the following major components:

a) Product storage tanks
b) Product tracking system (measuring balances)
c) Peristaltic pump
d) Pressure relief valve (PRV)
e) Compressed air system
f) Filter
g) Fittings and valves
h) Inline viscometer
i) Data acquisition system

The detailed explanation for the selection of each of these components is as follows:

A). Product Storage Tanks: The tank material selected for this application was high density polyethylene (shown in Figure 29). This material has an excellent chemical compatibility with petroleum lubricants and water. This specific variety of tank had a rounded bottom with a ½" bulkhead fitting for easy drainage and rests on a steel stand. They are connected to the main pipeline through flexible buna-nitrile hydraulic hoses.

Figure 29. Polyethylene Product Storage Tanks - 30 Gallons Capacity, Measuring Scales and Metal Foundations

B). Product Tracking System (Measuring Balances): The product tracking system best suited to our application was a system of three electronic balances resting under each of the three 30-gallon product storage tanks. The main criteria for the selection of electronic balances were weight capacity, size, polling rate and cost. A simple calculation was used to determine the maximum possible weight of the scales based on the density of water (8.34 lbm/gal) and the weight of the tank stands (~50 lbm). In total the scales must be able to

accurately display up to 300 lbs, representing a full tank of water used in early safety tests. The second factor in selecting a scale is the size of the scale. In this case, the scale could not be wider than two feet, as the total width of the plant is four feet (two side by side). To ensure that the weight of the scales could be accurately measured, the polling rate of the scale had to be high enough to capture swings in weight change when the pump is turned on and off. In the end, the scales chosen had a 600 lb weight capacity (illustrated in Figure 30). This scale easily meets the minimum weight requirement of 300 lbs and remains within the required size constraints at just 19.75" wide. This scale has a 600 lbm range (±0.1 lbm), with a maximum capacity of 900 lbm. These scales are connected to a digital readout, which then forwards this reading to the data acquisition system via RS485 connection.

Figure 30. Measuring Balances with 600 lb Weight Capacity

C). Viking Spur Gear Pump: To effectively handle high viscosity fluids in our project, we need a peristaltic pump. While our industrial partner uses sliding vane positive

displacement pumps, these are not suitable for the scale of our project. Therefore, we explored various peristaltic gear pumps and found that the best fit for our requirements is a spur gear pump. Specifically, we chose the viking spur gear pump (illustrated in Figure 31, which has a maximum flow capacity of 7 gallons per minute (GPM) and is tailored for high viscosity fluids. This pump features a cast iron interior and 3/4" NPT ports, which are reduced to ½" outer diameter tubing.

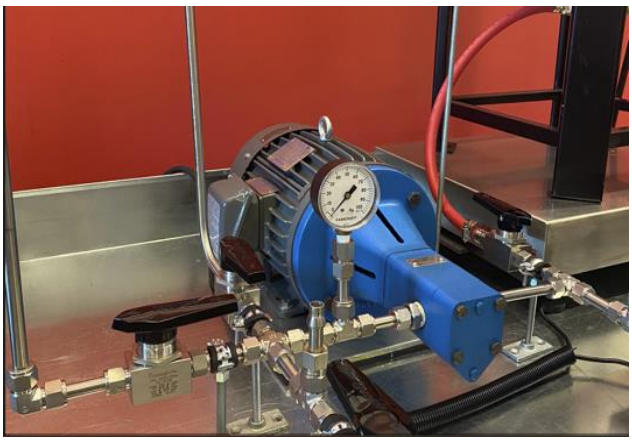

Figure 31. Viking Spur Gear Pump, Flow Capacity – 7 GPM

For safety and to prevent overpressure, particularly in case of operator error, we selected a pressure relief valve (PRV) with a specification that matches the lowest pressure rating in our system, which is 100 PSI for the filter. We set the PRV to 70 PSI, which is higher than the normal operating pressure at 7 GPM but below the maximum pressure rating of the filters. Based on performance charts for lubricant oils up to 500 SSU (108 cSt), the maximum pressure drop through the valve is 25 PSI, staying within the filter's safe limit. We acquired the PRV from Fulflo, specifically the V-Series VSS-3R/3SS/XS

model. This valve has an 11 GPM capacity, a set pressure range of 60-175 PSIG, and can handle a full 7 GPM flow at approximately 25 PSI overpressure. Its maximum rated pressure is 1000 PSI, and it features a buna-nitrile seal with stainless steel construction.

D). Inline Viscometer: The most crucial property of a lubricating oil is its viscosity, as it is essential for achieving optimal performance in any machinery application. Selecting an oil with the right viscosity that matches the operating conditions is key. Kinematic viscosity testing is vital for confirming the quality of a product batch and the success of a flushing operation. Traditional methods for measuring kinematic viscosity typically involve sampling and laboratory analysis using glass capillary viscometers. The effectiveness of these methods depends heavily on the quality, accuracy, and utility of the data obtained from the samples. It is necessary to take precise samples from each batch for process and quality control, as well as assurance. However, this approach is labor-intensive, time-consuming, and prone to errors. To overcome these challenges, automating the viscosity testing process can reduce manual labor and operational expenses. Additionally, real-time viscosity measurement for a product batch offers extra environmental and logistical benefits, as it reduces the need for multiple iterations of the flushing operation. We employ a Hydramotion-manufactured inline viscometer (illustrated in Figure 32) to explore the benefits of real-time viscosity measurements as compared to traditional sampling methods. Key features of the Hydramotion TV5 series, a through-flow viscometer, include its seamless bore design, compatibility with pigging systems, a lack of moving parts, and no requirement for regular maintenance. This model's viscosity measurement capabilities range from 0 to 10,000 centipoise (cP), with a rapid measurement time of just 1 second. The device boasts an accuracy of either 1% of the reading or +/- 0.1 cP. It operates

effectively within a temperature range of -50°C to 100°C and can handle pressures up to 100 bar.

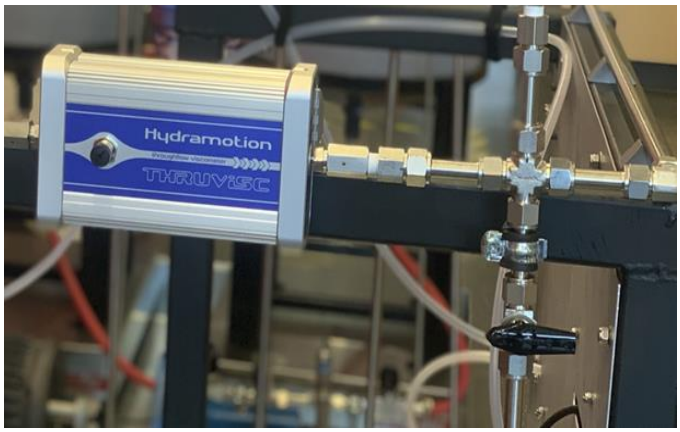

Figure 32. Inline Viscometer for Real Time Viscosity Measurement

E). Data Acquisition System: Accurate and simultaneous recording of experimental data is essential for understanding and gaining insights into the studied process. Recognizing this, we identified the need for a data acquisition system (DAQ). The DAQ allows us to effectively gather, process, and analyze data from various instruments such as scales, inline viscometers, and thermocouples. It offers real-time measurement capabilities, crucial for our experimental procedures. This immediate data access is pivotal for monitoring and controlling experimental variables, contributing significantly to the effective modeling of our system and enabling prompt decision-making. After thorough research and evaluation, we chose the DAQ from NI, Labview (illustrated in Figure 33). Our selected system includes a cRio-9045 chassis with eight slots for multi-module input, a choice influenced by our plans for future expansion and the desire for increased flexibility in adding more

parameters to enhance our study's effectiveness. The selection criteria for the DAQ were based on specific needs of our experimental pilot plant, focusing on the type of measurement signals, the maximum sampling rate, and the number of channels that both the individual modules and the chassis can support. The chosen data acquisition system aligns with the signal requirements of our equipment. The scales used in the system deliver a 9 V DC output, while the inline viscometer delivers a 4 – 20 mA analog signal. Additionally, the thermocouple module is designed for type C series input, complementing perfect temperature measurement required for our system. The core of our data acquisition system is the cRio-9045 chassis, with an 8-slot housing for accommodating various modules. In this work we utilized three of these slots for specific modules. The first slot was occupied by NI–9870 and facilitates mass readouts from the scales. This module uses a GPIB interface for interaction with the scales for simultaneous readouts. The second slot housed the NI – 9212 module paired with TB – 9212 allowing for precise temperature measurements. The third module contained the NI -9203 module dedicated to viscosity readouts from the inline viscometer.

Figure 33. Data Acquisition System (DAQ)

The finalized CAD design of the pilot plant is illustrated in Figure 34. Furthermore, Figure 35 illustrates the engineered pilot plant in the laboratory.

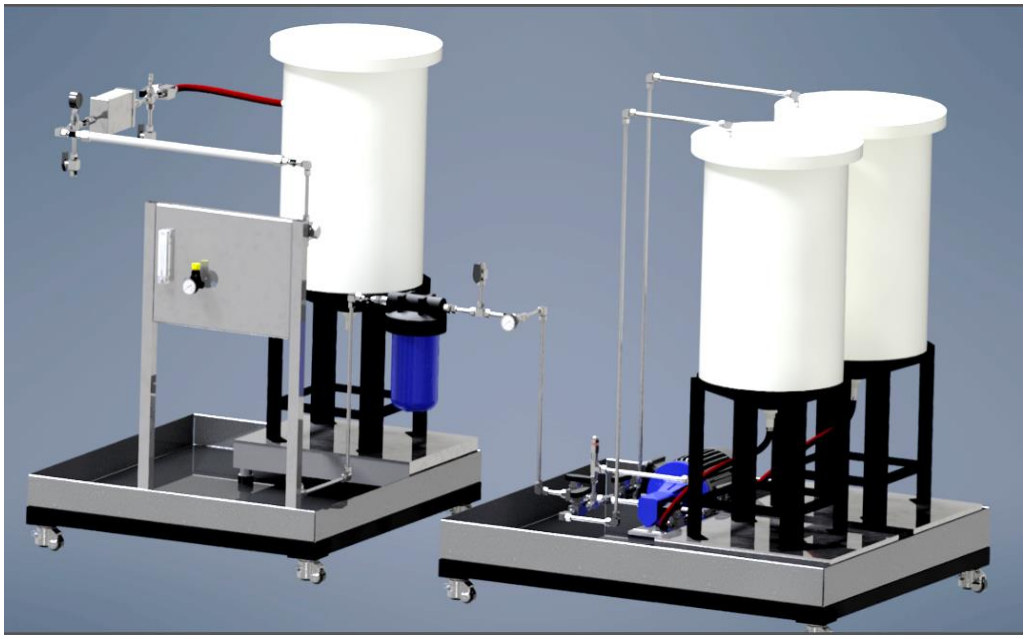

Figure 34. Computer-aided Design (CAD) of the Pilot Plant

Figure 35. Engineered Pilot Plant in the Laboratory

6.2 Process Flow Diagram of the Pilot Plant

A process flow diagram of the developed pilot plant, replicating a single-family line is illustrated in Figure 36. The phenomena of the commingled oil formation were studied using this design.

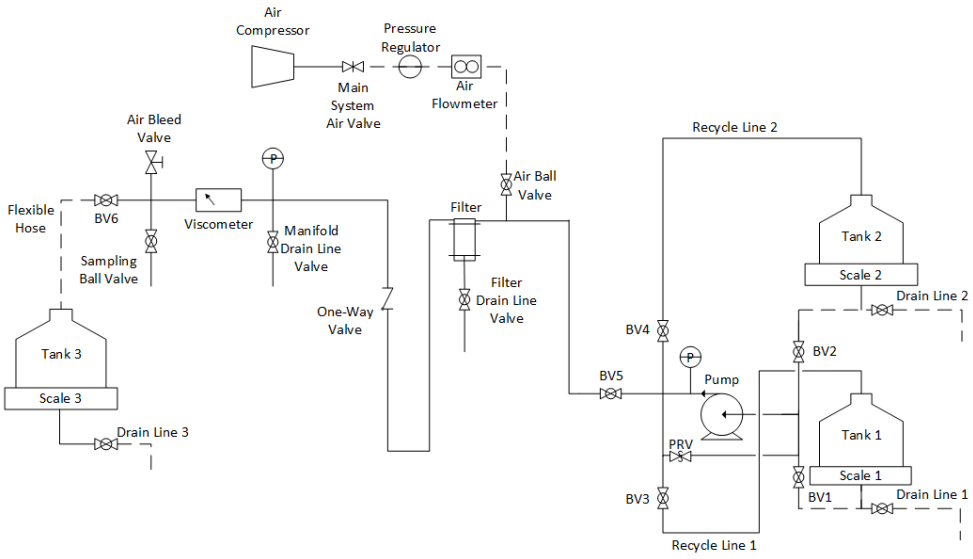

Figure 36. Process Flow Diagram of the Pilot Plant

The system illustrated in Figure 36, flows from right to left in order to accurately represent how the pilot plant was constructed and the way fluid moves from the first two tanks to the third tank. Starting at the two tanks pictured to the right, the simulant fluid is filled into the two tanks to start, with Tank 1 fluid representing the residual fluid and Tank 2 representing the flushing fluid of the system. As a note, all three tanks are on scales in order to determine the quantity, or mass, of fluid moving through the system and the flowrate of the simulant fluid when the scales are paired with a time of flush. This is essential to determining how the system behaves as fluid flowrate greatly affects the mixing behavior within the pipelines and the time necessary to simulate a flush. Draining from below the tanks, the simulant fluid encounters a tee, where one side of the tee leads to the drain line used to drain the tanks and the other side leading to the pump. The drain line ball valves denoted in the process flow diagrams are by default closed unless the system is

being drained. The section between the pump and each of the two tanks are separated by ball valves (BV1 and BV2), as this controls which fluid will be pushed through the system depending on whether the system is being prepared for a flush with the residual fluid (Tank 1) or is in the process of flushing (Tank 2). For example, if the system is being flushed, BV2 will be open and BV1 will be closed. After the ball valves, the fluid reaches the pump where it is then propelled through the rest of the system. Immediately after the pump there is a pressure gauge which, in conjunction with the pressure gauge at the end of the line, allows the operator to determine the outlet pressure of the pump and the total pressure drop of the system. The fluid then reaches a cross in the pipeline where there are three options, the first of which is achieved by opening BV3. This allows the residual fluid to recycle back into Tank 1 to allow the pump to reach steady state and to prime the pump with the simulant fluid. The second option is the open BV4, which allows the flushing fluid to recycle back into Tank 2, achieving the same result as BV3. The final option is to open BV5, which allows the simulant fluid to flow through the rest of the system. After BV5, the system encounters a bend where the pipes reach a higher height to allow the user greater access to the filter and compressed air lines. Next is the air ball valve, which in conjunction with the pressure regulator and air flowmeter allows compressed air to be blown through the system for increased drainage of the residual product. The fluid enters the bag filter shortly after which filters the fluid and includes a drain line to allow for better filter drainage. This filter was chosen to represent the partner industrial plant filters most accurately, which is also a bag filter and has an equal system to filter volume ratio. After the filter, there is a U-bend in the line followed by a one-way valve, which is also representative to that of the partner industrial facility. The U-bend in conjunction with the

one-way valve allows for the modeling of simulant fluid holdup in the system and the effectiveness of system drainage. The simulant fluid then reaches the “manifold”, which connects the one-way valve to the filling spear and Tank 3. Located on the manifold is a pressure gauge to determine the pressure drop of the system and a drain line, which is utilized for system drainage. Shortly after is the in-line viscometer, which records the viscosity of the simulant fluid as it flows through the system and models how the system behaves during a flush. The final connection before reaching Tank 3 is an air-bleed valve, which is used to bleed all air from the system, and a sampling port used to collect intermittent samples during a flush. Lastly, the simulant fluid flows through BV6 and into Tank 3, which is the commingled tank and where both the residual and flushing fluids flow to at the end of the line. BV6 is utilized to separate the system from Tank 3, which is essential when draining the system using compressed air. This tank also had a scale to determine how much fluid flowed through the system and a drain line to drain the tank after a flush has been performed.

The pilot plant study is a work in progress and the further studies are being performed by the fellow graduate and undergraduate students in the lab. To this end, in the next chapter, i.e. chapter 7, we proceed to our second approach of optimizing the flushing operations through process systems engineering. In this approach we formulate the flushing operation as an optimal control problem and develop a flowrate controlling strategy for conducting an efficient flush.

Chapter 7

Process Systems Engineering Approach

Text and figures are reproduced and adapted with permission from S. S. Jerpoth, R. Hesketh, C. S. Slater, M. J. Savelski, and K. M. Yenkie, “Strategic Optimization of the Flushing Operations in Lubricant Manufacturing and Packaging Facilities,” *ACS Omega,* p. acsomega.3c04668, Oct. 2023, doi: 10.1021/acsomega.3c04668.

7.1 Optimal Control Problems and Applications

In the course of the flushing procedure, a mixture comprising both the remaining oil and the incoming oil is generated. As we progress through each time step, the proportion of the incoming lubricant in the mixture steadily rises while the proportion of the remaining lubricant steadily diminishes. This dynamic evolution over time signifies that the system is in a state of continuous change, thus categorizing it as a dynamic system. Optimal control theory, a mathematical discipline, specializes in identifying the most efficient methods for regulating dynamic systems. In this chapter, we delve into the development and optimization of the flushing procedure, treating it as an optimal control problem.

Within the petroleum industry, optimal control problems are indispensable tools applied across a range of crucial processes and operations. These applications encompass various domains: Reservoir management relies on optimal control to maximize hydrocarbon extraction from oil reservoirs while contending with complex constraints and uncertainties. This entails finely tuning injection rates, strategically placing wells, and adjusting operational variables to optimize oil and gas recovery [110]–[112]. Advanced methods such as model predictive control (MPC) and Pontryagin's maximum principle find

utility in this context [113]–[115]. Optimal control plays a pivotal role in drilling operations, enabling real-time adjustments to drilling parameters. This adaptability enhances drilling efficiency and reduces the likelihood of accidents [116]–[118]. Pipeline management is another arena where optimal control strategies come into play, ensuring the streamlined and cost-effective transport of oil and gas [119], [120]. This involves managing factors such as pressure regulation, optimizing flow rates, and minimizing energy consumption. Finally, in the complex landscape of refinery scheduling, optimal control techniques are essential for crafting efficient production schedules. These schedules are carefully crafted to meet market demands while optimizing resource allocation and minimizing operational costs. Together, these applications underscore the indispensable nature of optimal control in enhancing efficiency and effectiveness within the petroleum industry [121].

Optimal control is a field that examines the details of control functions, specifically examining their properties and characteristics. These control functions, when integrated into differential equations, yield a solution that seeks to either minimize or maximize a designated performance index or objective. In practical engineering applications, these control functions take the form of control strategies, which essentially dictate how a system or process should be controlled [122].

Optimal control deals with the properties of control functions, such that these functions, when inserted in differential equations, give a solution that minimizes or maximizes a performance index. In engineering applications, the control function is a control strategy. The differential equations describe the dynamic response of the mechanism to be controlled and depend on the control strategy employed [122]. The

evaluation of the time-dependent operating profiles, in terms of the control variable, is used for optimizing the process performance [123]. It's worth noting that optimal control problems present unique challenges compared to other types of optimization problems where decision variables are scalar. This complexity arises due to the dynamic nature of the decision variables in optimal control. Decision variables in optimal control are functions over time, and optimizing these functions within a dynamic system necessitates a more complex approach. Consequently, optimal control problems demand specialized methodologies and tools tailored to address these dynamic complexities.

In this chapter, the focus is on optimizing the pipeline flushing process at a lubricant facility through dynamic system analysis. The key element to manage this system dynamically is the regulation of the oil flow rate used in the flushing operation, which has been established as the control variable in this study. The objective here is to develop a control policy for the flow rate that can adapt over time, a goal pursued through dynamic optimization strategies. By reaching a theoretically ideal flow rate profile, we have gathered critical data that can guide both the design and supervision of the flushing operation moving forward. Solving the optimal control problems necessitated a deep dive into mathematical theories, leveraging techniques including dynamic programming, the calculus of variations, discrete-time non-linear programming, and the application of Pontryagin's maximum principle [124], [125]. The mathematical depth involved in some of these techniques; both calculus of variations and dynamic programming rely on the use of second-order differential equations and partial differential equations, introducing a high level of mathematical complexity. Pontryagin's maximum principle, on the other hand, simplifies the process significantly by requiring only first-order differential equations,

thereby reducing computational demands and presenting a more appealing option compared to the other methodologies [123].

7.2 Viscosity Blending Correlations

Traditional viscosity testing methods, following the ASTM D445 standards [109], are time-intensive, often taking between 20 to 30 minutes . This lengthy process results in significant operational pauses. Addressing this inefficiency, our study aims to improve in-line control during the flushing process by formulating models to predict the viscosity of lubricant blends in real-time. We have incorporated viscosity blending correlations from the American Petroleum Institute's Technical Data Book (API-TDB) [126], [127]. The specific correlation, denoted by equation (1), computes the viscosity of a blend comprised of two or more components, using the cubic-root average of the viscosities of the individual components. This calculates the viscosity of the blend and also provides insight into the concentration of each component. With this equation, we can monitor in real-time how the viscosity of the mixture adjusts to meet the requirements of the new lubricant during the flushing process.

In our context, the suffix 'A' stands for residual lubricant and the suffix 'B' stands for upcoming lubricant (flushing lubricant).

$$\mu_{AB}^{\frac{1}{3}} = x_A \, \mu_A^{\frac{1}{3}} + x_B \, \mu_B^{\frac{1}{3}} \tag{17}$$

Where: μ_{AB} – Viscosity of mixture of lubricant A and B (cSt)

μ_A – Viscosity of residual lubricant (cSt)

μ_B – Viscosity of upcoming lubricant (flushing oil) (cSt)

x_{A} – Mass fraction of residual lubricant

x_{B} – Mass fraction of upcoming lubricant (flushing oil)

Note: In the reference Riazi 2005 [126], x_A and x_B in equation (17) stands for mole fraction of the pure components. However, in this work we noticed that the mole fractions and mass fractions for the lubricant mixtures had negligible difference and therefore to eliminate the computational complexities, we considered x_A and x_B to be the mass fractions.

To validate the API-TDB recommended blending correlation for lubricant mixtures, a series of experiments were conducted following this stepwise procedure:

Step 1: We prepared known compositions of lubricant mixtures, ranging from a volume fraction of 0.1 to 0.9, with each sample incrementing by 0.1. This resulted in a total of eleven samples. We ensured the accuracy of sample preparation by selecting a total sample volume of 25 ml and carefully measuring the weights while mixing the two lube oils. This allowed us to obtain precise mass fraction data for each of the eleven samples.

Step 2: The kinematic viscosity of each sample was determined according to the ASTM D445 guidelines [109], using ubbelohde viscometers and a constant temperature bath setup.

Step 3: We compared the experimentally measured viscosity values with those calculated using the blending correlation. In Figure 37 (left), you can see the ubbelohde viscometers and the constant temperature bath setup used in the experiments. The changing colors depicted in Figure 37 (right) visually represent the increasing concentration of the golden-colored lube oil in a mixture of translucent and golden lube oil with known mass fractions. We conducted the validation of calculated viscosity values against experimentally measured values for two distinct lubricant mixtures, as illustrated in Figure 37 . The agreement within a 5% margin of error confirmed the applicability of the blending correlation to lubricant mixtures.

Figure 37 (left) illustrates the Ubbelohde viscometers and a constant temperature bath setup that was used for the experiments. The changing colors in Figure 38 visually depict the increasing concentration of the golden-colored lube oil in a mixture of translucent and golden lube oil of known mass fractions. The validation of the calculated viscosity values against the experimentally measured values was carried out for two distinct lubricant mixtures, as shown in Figure 38. The agreement within a 5% margin of error between the experimental and the calculated values confirmed the applicability of the blending correlation to lubricant mixtures.

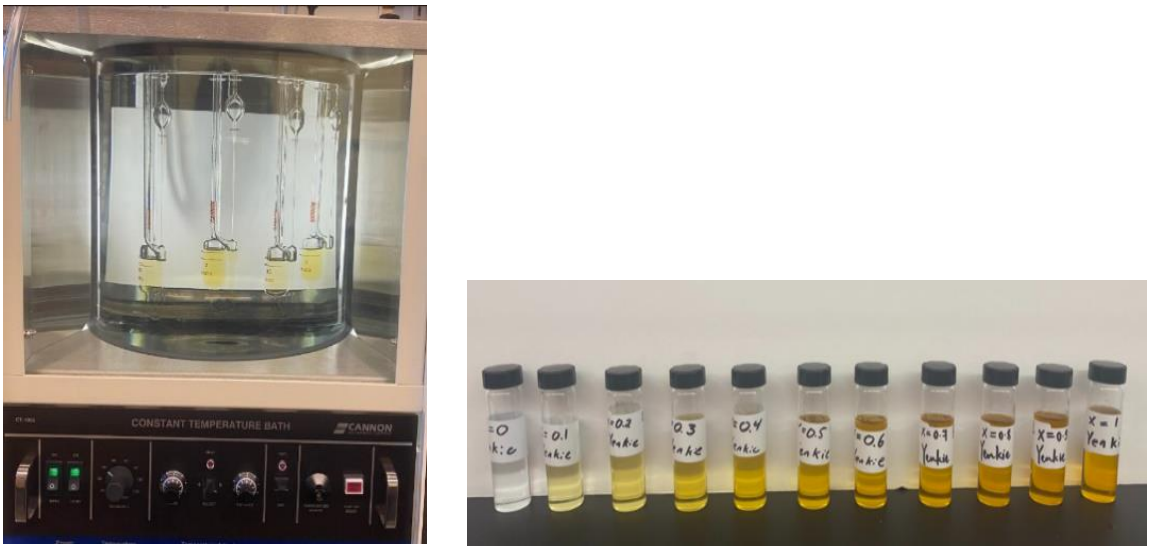

Figure 37. Constant Temperature Bath Setup with Ubbelohde Viscometers for Kinematic Viscosity Measurement (left) Sample Vials of Known Mass Fractions of Lubricant Mixtures (right)

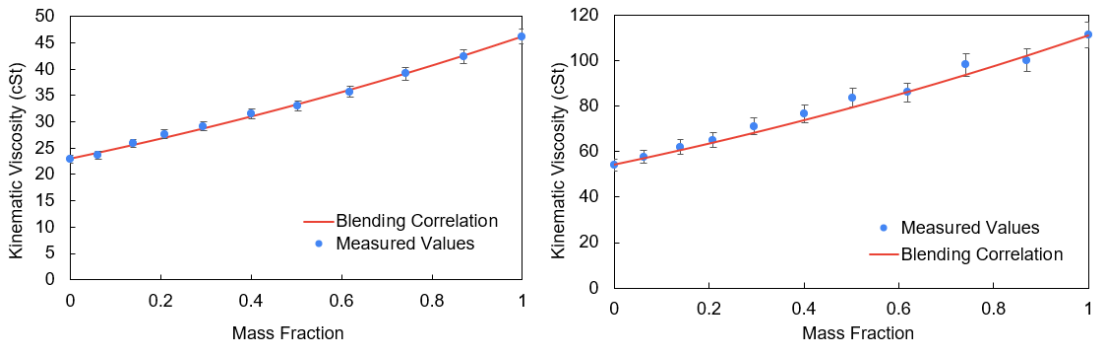

Figure 38. Validation of API-TDB Blending Correlation for Lubricant Mixtures. Blue Data Points Indicating the Experimentally Measured Values of Kinematic Viscosity and Red Curve Illustrating the Calculated Value from the Blending Correlation

7.3 Dynamic First Principles Model of Flushing Operation

Let us consider that initially, lubricant A is processed through the pipelines. After the packaging of 'lubricant A' is completed, the upcoming batch of lubricant B is to be packaged as illustrated in Figure 39. Hence, the pipelines must be flushed with lubricant B until the desired specifications are reached.

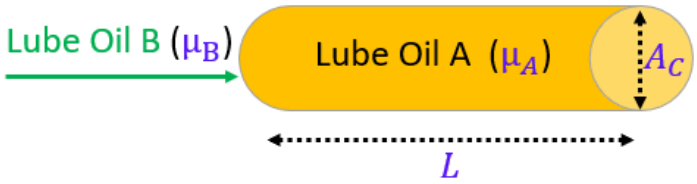

Figure 39. Illustration of a Changeover Operation in a Lubricant Pipeline with a cross sectional area 'A_C' and total length 'L'.

Below are the list of model parameters and variables used for the problem formulation:

Model Parameters:

μ_A – Viscosity of residual lubricant (cSt)

μ_B – Viscosity of upcoming lubricant (flushing oil) (cSt)

ρ_A – Density of lubricant A (kg/m^3)

ρ_B – Density of lubricant B (kg/m^3)

A_C – Cross-sectional area of the pipeline (m^2)

L – Total length of the pipeline (m)

V – Total volume of the pipeline (m^3)

Model Variables:

μ_{AB_t} – Viscosity of blend of lubricant A and B (cSt)

m_{A_t} – Mass of lubricant A (kg)

m – Total mass of the system (kg)

x_{A_t} – Mass fraction of lubricant A

x_{B_t} – Mass fraction of lubricant B

Q_t – Volumetric flowrate of lubricant B (m^3/s)

t – Flushing time (s)

A general mass balance equation for lubricant A and B is derived below:

$$\text{Accumulation} = \text{Input} - \text{Output} + \text{Generation} - \text{Consumption} \quad (18)$$

Assumptions: (1) Initially the pipeline is completely filled with lubricant A before the lubricant B is processed. (2) The densities of lubricants A and B is approximately the same. (3) There is no chemical reaction taking place in the pipeline.

The model parameters ρ_A, ρ_B, A_C, L, and V remains unchanged for the system. However, the parameters μ_A and μ_B changes with respect to each case study and the effect of the changes have been discussed in results section.

The generation and consumption term in equation (18) can be neglected as there is no chemical reaction taking place in the pipeline. Therefore,

$$\frac{dm_{A_t}}{dt} = 0 - \rho_A x_{A_t} Q_t + 0 - 0 \quad (19)$$

Writing equation (3) in terms of mass fraction

$$\frac{dx_{\mathrm{A_t}}}{dt}\, m = -\rho_A x_{\mathrm{A_t}}\, Q_t \tag{20}$$

$$\frac{dx_{\mathrm{A_t}}}{dt} = \frac{\rho_A x_{\mathrm{A_t}}\, Q_t}{m} \tag{21}$$

$$m = \rho.V \;\; (Assuming\; \rho_A = \rho_B = \rho) \tag{23}$$

$$m = \rho A_C\, L \tag{24}$$

Substituting equation (24) in equation (21)

$$\frac{dx_{\mathrm{A_t}}}{dt} = -\frac{x_{\mathrm{A_t}}\, Q_t}{A_C\, L} \tag{25}$$

Similarly,

$$\frac{dx_{\mathrm{B_t}}}{dt} = \frac{x_{\mathrm{A_t}}\, Q_t}{A_C\, L} \tag{26}$$

Differentiating equation (1) w.r.t 't' and substituting the values of $\frac{dx_{\mathrm{A_t}}}{dt}$ and $\frac{dx_{\mathrm{B_t}}}{dt}$

$$\frac{d\mu_{AB_t}}{dt} = \frac{3x_{\mathrm{A_t}}\, Q_t}{A_C\, L}\left[x_{A_t}\, \mu_A^{\frac{1}{3}} + x_{B_t}\, \mu_B^{\frac{1}{3}}\right]^2 \left[\mu_B^{\frac{1}{3}} - \mu_A^{\frac{1}{3}}\right] \tag{27}$$

Equations (25), (26), and (27) represents our first principles models. These models were then validated against well designed experimental data. More details in regard to the validation is presented in section 7.4.

7.3 Validation of First Principles Models

Our partnered lubricant facility processes over 15,000 unique products in a given production year. We first started by collecting and analyzing data from the regular flushing operations conducted by this facility. Our analysis gave us a strong indication that the

flushing operation was not optimum, and the flush time was chosen based on the operator's experience and through trial-and-error method. Therefore, in the subsequent phase, we formulated and executed a set of structured experiments to acquire empirical data points for the purpose of validating our mathematical models. The procedural sequence observed during these experiments within the plant is outlined as follows:

Step 1: 25 ml sample bottles, were prepared ensuring proper labeling.

Step 2: Prior to initiating the flush, the initial volume of the feed tank was recorded.

Step 3: The flush procedure was initiated with well-defined time.

Step 4: Over a flush duration spanning from 60 to 120 seconds, based upon operator's experience, samples were collected at every 10-second interval.

Step 5: Upon completion of the flush, the timer and the sample collection were halted.

Step 6: The final volume of the feed tank for then documented.

Step 7: Subsequently, the collected samples were dispatched to the laboratory for kinematic viscosity testing.

The samples taken at 10-second intervals provided us with valuable insights into how the viscosity of the mixture, comprising residual and fresh lubricant, progressed toward meeting the desired specifications of the new lubricant at each time increment. The flushing data for twenty-five different changeover operations were analyzed and compared against the mathematical models. Confirmation of the accuracy of our models in representing the flushing operation was established with an agreement within a 7% margin of error. This means that the percentage error between the experimental and the simulated results was within 7%. Figure 40 provides a comparative analysis between the experimental data points and the simulated outcomes for four specific changeover operations. We have

singled out these four changeovers from the total of twenty-five, as they offer a clear and illustrative depiction of the transition providing further insight into the effectiveness of our models in capturing these transition scenarios.

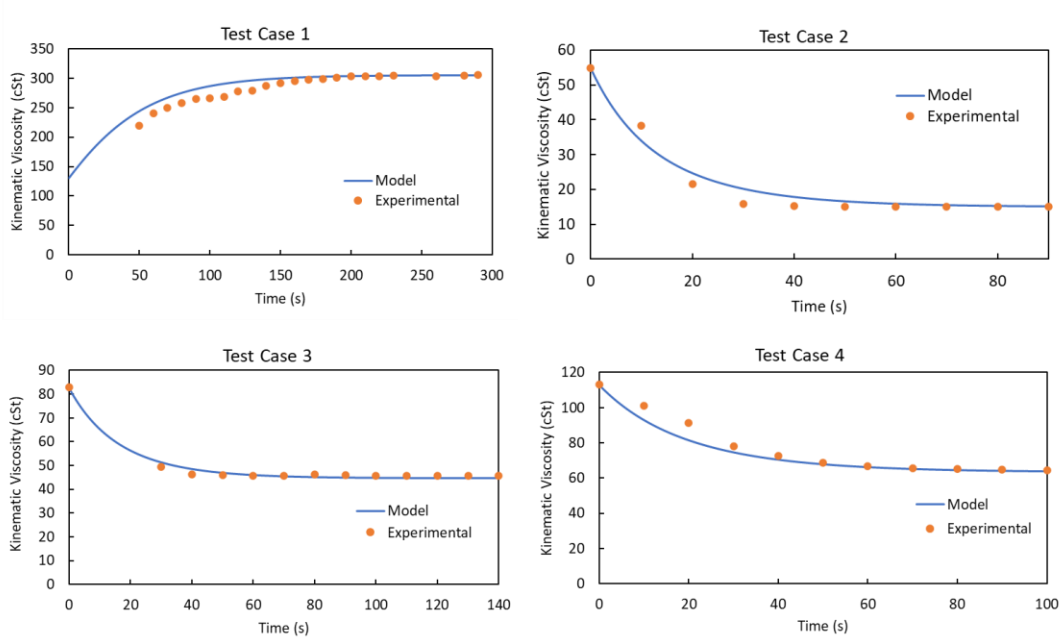

Figure 40. Validation of Developed First Principles Models with Empirical Data Points Collected from Well-Structured Experiments Conducted at the Partnered Lubricant Facility

Table 11 illustrates the viscosity difference between the residual and flushing oil and the flushing flowrate for each of these test cases.

Table 11

Viscosity Gradient between the Residual and the Flushing Lubricant, and Flushing Flowrate of the Selected Test Cases

Test Case	Viscosity of Residual Oil (cSt)	Viscosity of Flushing Oil (cSt)	Viscosity Difference (cSt)	Flushing Flowrate (m^3/s)
1	130.26	305.39	175.13	0.003
2	54.85	15.06	39.79	0.006
3	82.84	44.8	38.04	0.006
4	113	63.2	49.8	0.005

To illustrate, consider test case 1 where the residual lubricant had a viscosity of 130.57 cSt, while the new lubricant measured 305.39 cSt. This results in a significant viscosity difference of 174.82 cSt, signifying a transition from a low-viscosity oil to a high-viscosity one. The experimental data points are denoted by orange markers, while the blue curve highlights the results simulated using our first principles models. Similarly, in test case 2, the residual lubricant exhibited high viscosity, whereas the flush oil had a lower viscosity, i.e. this was a changeover from a high viscosity to a low viscosity oil resulting in a viscosity difference of 39.79 cSt. For test case 3, the viscosity difference was 37.17 cSt, and in test case 4, it was 48.56 cSt providing further insight into the effectiveness of our models in capturing these transition scenarios.

7.5 Formulation of Optimal Control Problem

Our objective is to have the upcoming oil (lubricant B) completely free of the residual oil (lubricant A) at the final collection point. Hence, the viscosity of the blend at the final time point should be equal to the viscosity of the lubricant B. Mathematically, our objective can be formulated to minimize the difference between the viscosity of the blend and the viscosity of lubricant B by finding an optimum flushing time, as shown in equation (28).

$$Min\, J = [\, \mu_{AB_t}\, (t_{final}) - \mu_B]^2 \tag{28}$$

The state of our system is controlled through the flow rate of lubricant B (flushing oil). Hence, the variable Q_t represents the control variable of the system. The process performance is determined by attaining the desired viscosity of lubricant B. Given the values of the state variables x_i [$where\ x_i = (x_{A_t}, x_{B_t}, \mu_{AB_t})$] and the control variable Q_t at time t, the differential equations (25), (26), and (27) specify the instantaneous rate of change in the state variables. The developed optimal control problem was solved using two solution approaches, viz. Pontryagin's maximum principle and discrete-time nonlinear programming (NLP).

7.5.1 Solution Using Method#1: Pontryagin's Maximum Principle

The application of the maximum principle requires an introduction of additional variables known as adjoint variables and a Hamiltonian. Three adjoint variables 'z_i', corresponding to each of the state variables, and a Hamiltonian was used in this work. The introduced adjoints must satisfy equation (30), and the Hamiltonian must satisfy

equation (31). The details of the derived adjoint and Hamiltonian equations are provided in Appendix A. Table 12 summarizes the various quantities that describe our model.

$$\frac{dx_i}{dt} = \mathrm{f}\,(x_i, Q_t\,, t) \tag{29}$$

$$\frac{dz_i}{dt} = -\sum_{j=1}^{n} z_j\,\frac{\partial f_j}{\partial x_i} \tag{30}$$

$$\frac{dz_i}{dt} = -\sum_{j=1}^{n} z_j\,\frac{\partial f_j}{\partial x_i} \tag{31}$$

Table 12

Quantities that Describe the Developed First Principles Mathematical Model

Quantity	Mathematical Model
Parameters	$\mu_A, \mu_B, A_C\,, L$
State variables	$x_i \quad = \quad [x_{A_t}\,, x_{B_t}\,, \mu_{AB_t}]$
State equations	$\frac{dx_i}{dt} \quad = \quad \mathrm{f}\,(x_i, Q_t\,, t)$
Adjoint equations	$\frac{dz_i}{dt} \quad = \quad -\sum_{j=1}^{n} z_j\,\frac{\partial f_j}{\partial x_i}$
Hamiltonian equations	$\mathrm{H} \quad = \quad \sum_{i=1}^{3} z_i\, f(\,x_i, Q_t\,, t)$

For evaluating the Hamiltonian derivative, we use an analytical method proposed by Benavides and Diwekar, 2013 [124] which introduces an additional variable corresponding to each state variable and adjoint variable. The variable θ_i corresponds to

each of the state variables x_i and the variable Φ_i corresponds to each of the adjoint variables z_i, respectively. These equations are described in detail in Appendix B.

$$\frac{dx_i}{dQ_t} \text{ and } \Phi_i = \frac{dz_i}{dQ_t} \tag{32}$$

$$\frac{d\left(\frac{dx_i}{dt}\right)}{dQ_t} = \frac{d\left(\frac{dx_i}{dQ_t}\right)}{dt} = \frac{d\theta_i}{dt} \tag{33}$$

$$\frac{d\left(\frac{dz_i}{dt}\right)}{dQ} = \frac{d\left(\frac{dz_i}{dQ_t}\right)}{dt} = \frac{d\Phi_i}{dt} \tag{34}$$

$$\frac{dH}{dQ_t} = \sum_{i=1}^{3}\left(\frac{dH}{dx_i}\right)\left(\frac{dx_i}{dQ_t}\right) + \sum_{i=1}^{3}\left(\frac{dH}{dz_i}\right)\left(\frac{dz_i}{dQ_t}\right) \tag{35}$$

Thus, the complete model will consist of three state equations [equations (25) – (27)], three adjoint equations, and twelve Hamiltonian equations. The algorithm starts with the initial guess of flowrate Q_t. Next, state equations represented by (29) are solved for the interval of t_0 to t_f using forward integration and employing Euler's method. Then, the adjoint equations represented by (30) are solved using backward integration. Next, the optimal control variable Q_t is obtained by finding the extremum of the Hamiltonian at each time step, using the optimality condition of [|dH/dQ_t|] < tolerance. Our tolerance limit is zero. If the optimality condition is not satisfied, the flowrate Q_t is updated using the gradient, such that the updated flowrate profile improves the objective function. Figure 41 shows the flowchart for the solution approach.

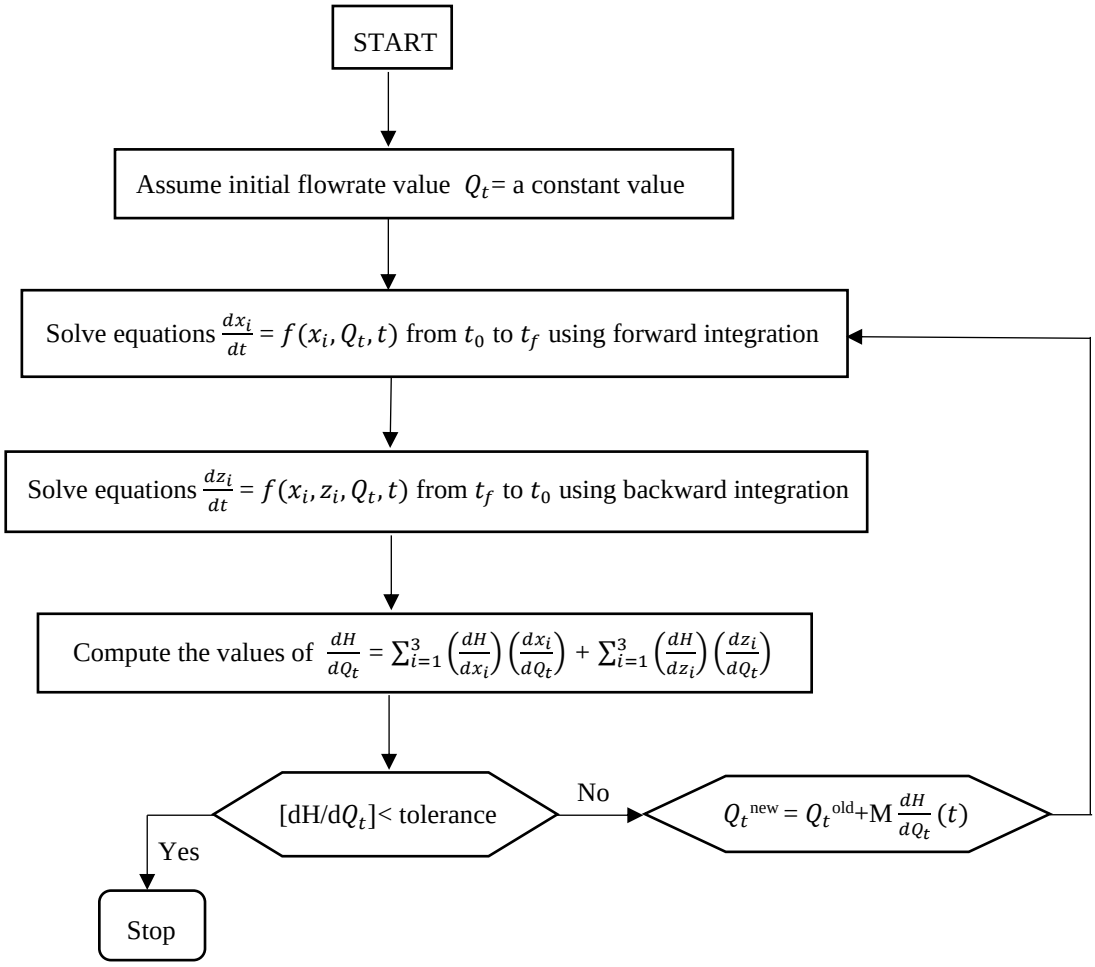

Figure 41. Flowchart of Solution Technique Using Maximum Principle Approach

In this work we experienced that the execution time for the Pontryagin's maximum principle algorithm exceeded over 60,000 seconds. Hence to overcome this drawback we used discrete-time nonlinear programming (NLP) solution method. In the discrete-time NLP solution approach, the total time is discretized into 'n' known intervals and the state equations are solved for each interval. More details of the method are presented in the following section 7.5.2.

7.5.2 Solution Using Method#2: Discrete-Time Non-Linear Programming (NLP)

In the discrete-time NLP solution method, the total flush time is discretized into known 'n' equal intervals. The objective function stays the same as shown in equation (36) and it is subjected to the integrated form of the state equations [equations (37) and (38)]. These equations are solved for each interval. Let's consider for an example the total flush time was 60 seconds and we divide the total flush time into 6 equal intervals of 10 seconds each as illustrated in Figure 42. The solution algorithm solves the state equations for each interval. In this solution approach the control variable '$\bar{Q}$' is provided as a vector and we specify the system specific maximum and minimum constraints for our control variable (flowrate of lubricant B).

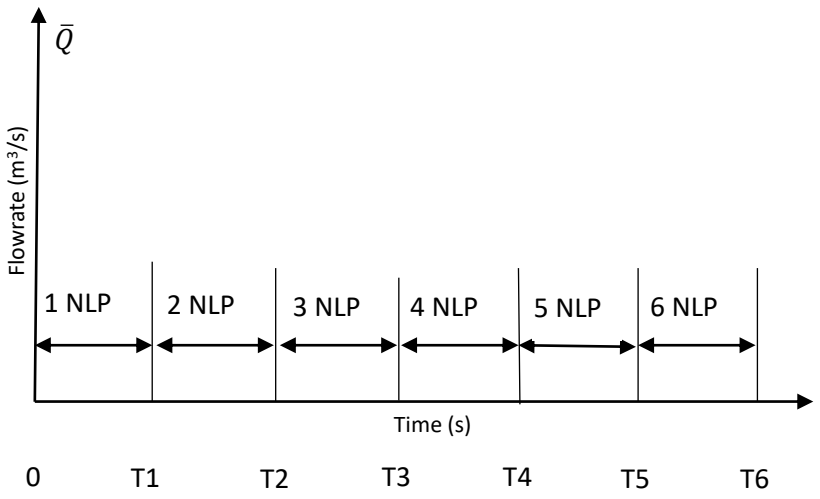

Figure 42. Discretization of Total Time into Equal Intervals to Solve the State Equations within Each Interval.

$$Objective: Min\, J = [\,(\mu_{AB_t}(t_{final}) - \mu_B)/\mu_B]^2 \tag{36}$$

Subject to:

$$x_{A_t} = exp\left(-\frac{\bar{Q}t}{A_c L}\right) \tag{37}$$

$$x_{B_t} = 1 - exp\left(\frac{-\bar{Q}t}{A_c L}\right) \tag{38}$$

Equation for μ_{AB_t}

$$\mu_{AB_t}^{\frac{1}{3}} = x_{A_t}\mu_A^{\frac{1}{3}} + x_{B_t}\mu_B^{\frac{1}{3}} \tag{39}$$

Next, we solve the state equations for the 1st interval to achieve the desired objective function. If the optimality criteria is not satisfied, the flowrate is updated for the next interval such that the updated flowrate profile improves the objective function. The iterations continue for 'n' intervals until the desired optimality condition is achieved. i.e., the difference in the viscosities of the blend and the viscosity of lubricant B is minimized. In other words, the desired specifications of the new lubricant B are reached. The choice of our decision variable is based on time because in real world scenario the plant operators at these facilities can provide the input in terms of time. Therefore, we study the optimum flowrate in a given time interval to conduct a successful flush. The developed discrete-time NLP problem is solved in MATLAB using the constrained optimization algorithm 'fmincon'. Figure 43 depicts the flowchart of the solution approach.

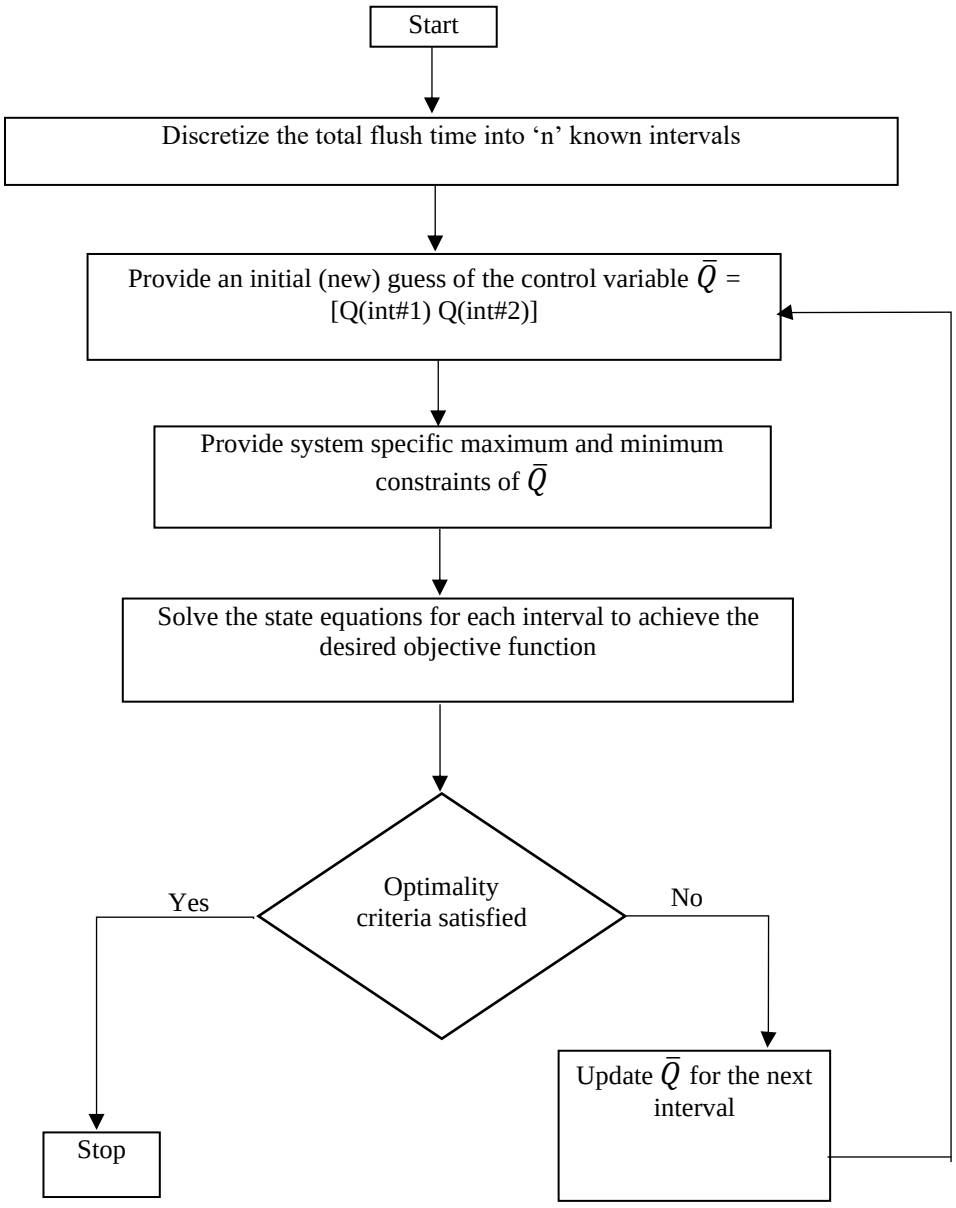

Figure 43. Flowchart of Solution Technique Using Discrete Time Non-Linear Programming (NLP) Solution Approach

7.6 Results and Discussions

The results and discussions are divided into two sub sections. Section 6.4.1 illustrates the maximum principle solution approach. Section 6.4.2 explains the comparison of maximum principle solution results with the discrete time NLP results and it's comparison with the experimental data.

7.6.1 Pontryagin's Maximum Principle Solution Method

The derivative of Hamiltonian profiles at different iterations for a case study is shown in Figure 44. It can be observed that the dH/dQ_t value decreases with every iteration.

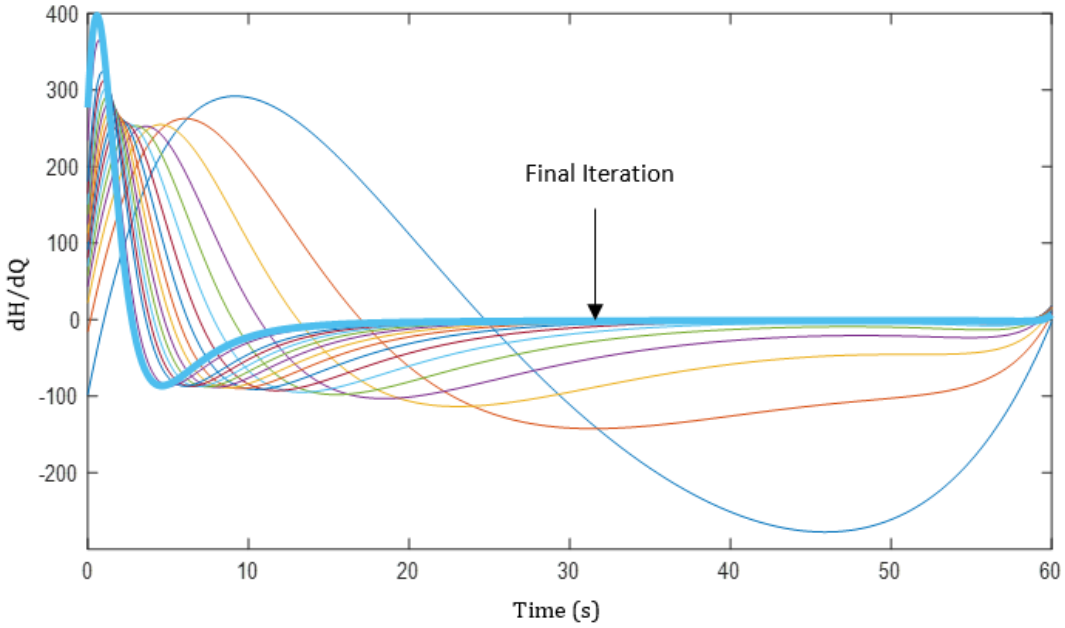

Figure 44. Graph Depicting the Hamiltonian Gradient Profiles for Each Iteration, Showcasing a Progressive Reduction in Value with Each Step, Ultimately Reaching the Tolerance Limit in the Final Iteration.

The final iteration value lies within the given tolerance limit which is a value close to zero. Hence, we conclude the flowrate to be optimal and the corresponding profile is shown in Figure 45.

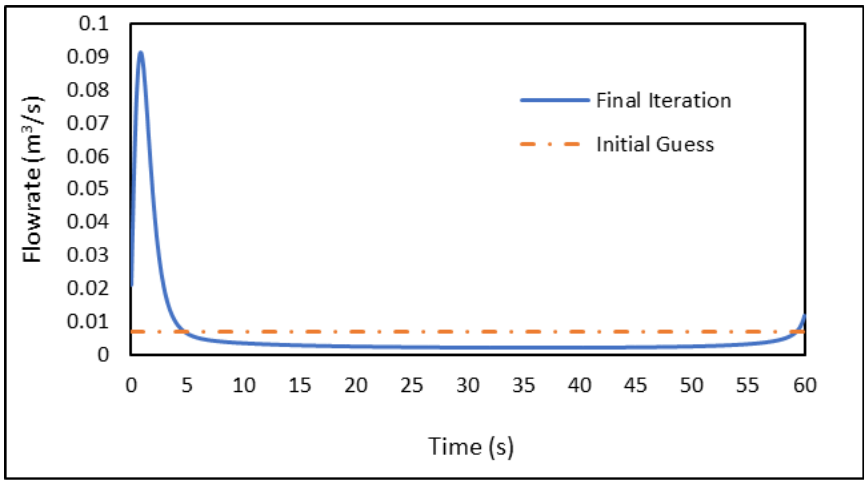

Figure 45. Profile of Flowrate Corresponding to the Final Iteration where the Hamiltonian Gradient Achieves the Desired Tolerance Limit

The final iteration of the optimal flowrate profile was used for simulating the state equations. The goal was to predict the time step at which the viscosity of the blend reaches the desired viscosity limits of the lubricant B. The comparison between the optimum flushing time predictions via the maximum principle solution approach, the discrete-time NLP solution approach and the experimental data is discussed in section 6.4.2.

7.6.2 Comparison of Different Solution Methods

We show a comparison of the maximum principle and the discrete time NLP solution approach for a test case 1 in Figure 46. We plot the flush time against the kinematic viscosity of the collected lubricant blend samples. Test Case 1 was a changeover operation

where the viscosity of the residual lubricant was 130.26 cSt and the desired viscosity of the new lubricant was 305.39 cSt. According to the industrial standards, the flushing can be stopped when the sample reaches a value within 5% of the desired value. At the partnered industrial facility, the operator based upon his experience with this specific product choose a total flush time of 290 seconds. However, as explained previously, for our designed experiments conducted at this facility, we collected samples at an interval of every 10 seconds for the total flush time.

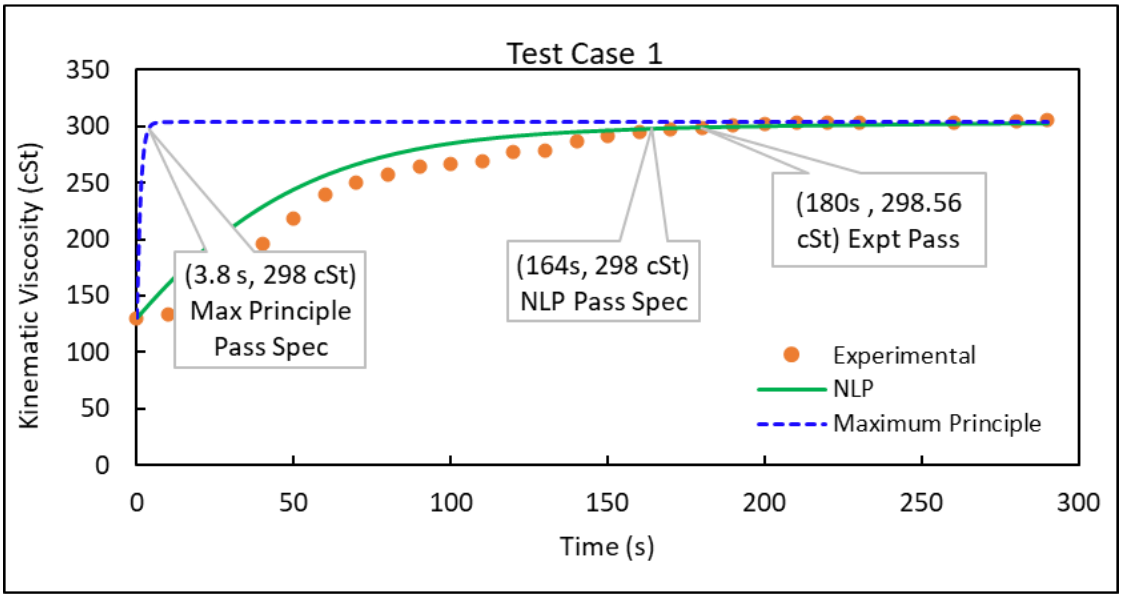

Figure 46. Comparison of Maximum Principle and Discretized Non-Linear Programming Solution Approach for Test Case 1 where the Viscosity of the Residual Lubricant is 130.26 cSt and the Desired Viscosity of the New Lubricant is 298.56 cSt

We tested these samples for their kinematic viscosity and the experimental data points are shown by the orange scattered plot in Figure 46. As observed the desired passing specification of 298.56 cSt was achieved right at the 18th sample for the total flush time of

180 seconds. Our results from the discrete-time NLP solution method (represented by the smooth green curve in Figure 46) shows that if the operation was to be conducted at an optimal flowrate profile the desired specifications will be achieved at a total flushing time of 164 seconds. The execution time for the problem was 250 seconds. Furthermore, we ran the simulation for the Pontryagin's maximum principle solution approach. Furthermore, we ran the simulation for the Pontryagin's maximum principle solution approach (illustrated by the dashed curve in blue Figure 46). The execution time for the problem was 70,360 seconds and the results indicate that the desired specification will be achieved at 3.8 seconds of the flushing time. However, this is not possible in practical scenario. We further compared the optimal flowrate profile for the non-linear programming solution method and the maximum principle solution method shown in Figure 47.

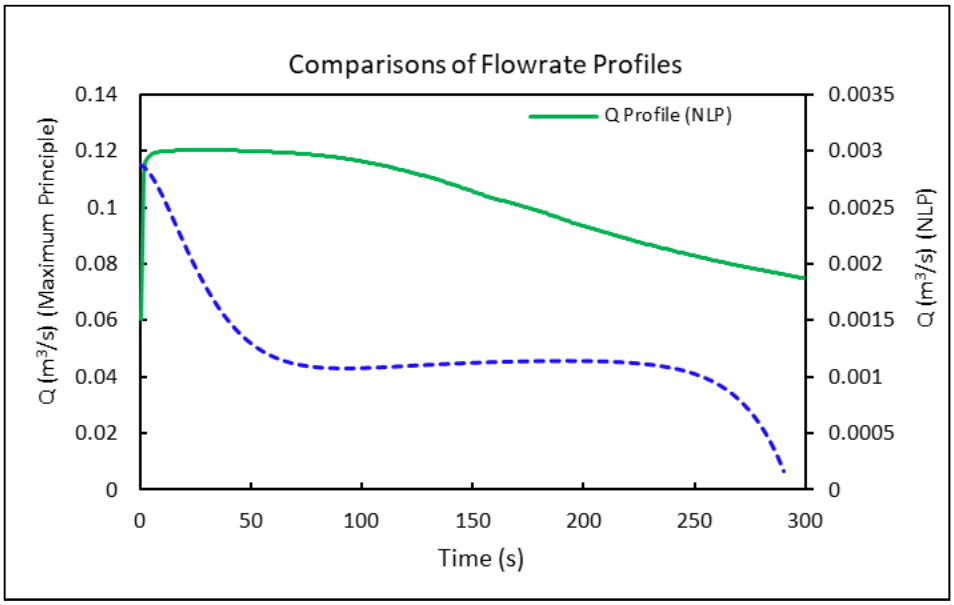

Figure 47. Comparison of the Optimal Flowrate Profiles for the Maximum Principle and the Non-Linear Programming Solution Methods for Test Case 1

The flowrate profile for the maximum principle method (dashed curve in blue in Figure 47), starts with the initial guess, and starts decreasing for the next 50 seconds of interval. It stays constant until 250 seconds and further starts decreasing until the last interval. The optimal flowrate profile for the NLP solution method starts with the initial guess reaches a maximum value and slightly decreases for the next intervals until the end time. Similarly, we compare results for the change in kinematic viscosity against time for twenty-five changeover operations and compare the results with the experimental data. The graphs for four changeovers are shown in Figure 48. For Test Case 2, the NLP prediction for the optimum flush time was almost double as compared to the experimental data. Furthermore, the maximum principle prediction for the optimum flush time was only a fraction of a second. For the Test Case 3 and Test Case 4, the NLP results obeyed very closely with the experimental data. Furthermore, the optimum flush time for the maximum principle was still below 5 seconds. The execution time for the NLP solution method was within 20 seconds whereas the execution time for the maximum principle exceeded over 70,000 seconds.

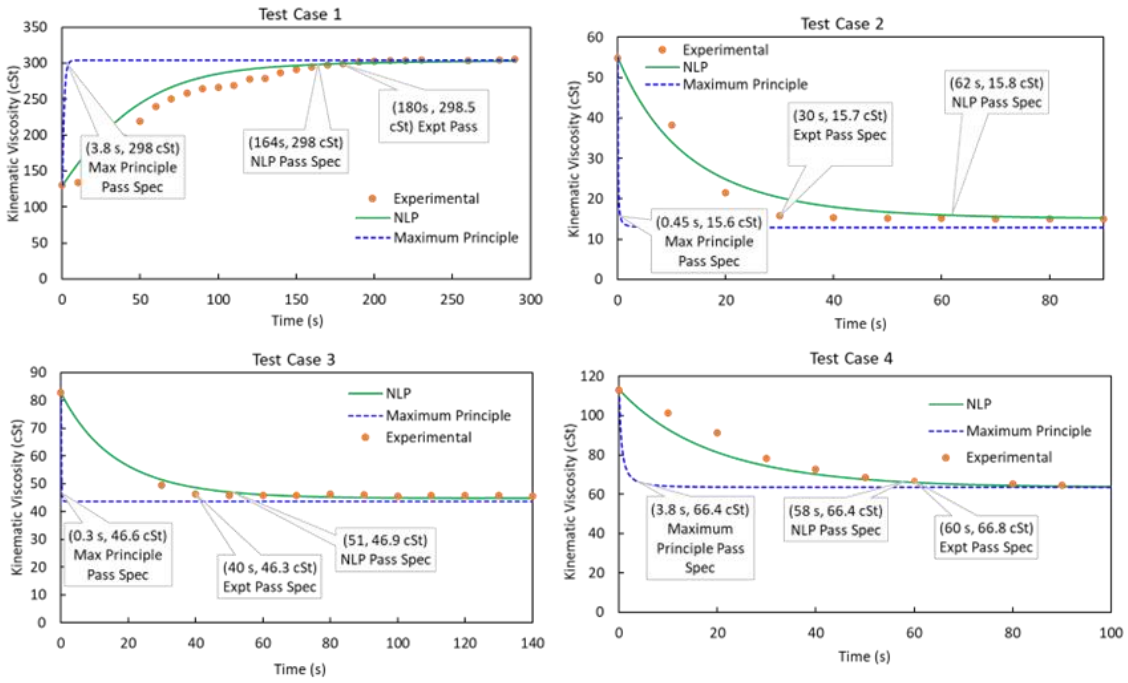

Figure 48. Comparison of Maximum Principle and Discrete-Time NLP Solution Approach

7.6 Economic and Environmental Significance

The existing trial and error method that is currently used at lubricant facilities often requires the flushing operation to be repeated for multiple iterations and therefore involves a significantly large associated flushing volume. Alternatively, if we apply the discretized NLP solution approach and conduct the operations at a customized flowrate, we can reduce the necessary flushing volume to over 30%. Figure 49 illustrates a comparison of the flowrate profile of the discrete-time NLP solution method and the constant flowrate. Looking at the area under the curve which illustrates the volume flushed we can observe that the green curve (discrete-time NLP) uses less volume as compared to the constant flowrate (red line).

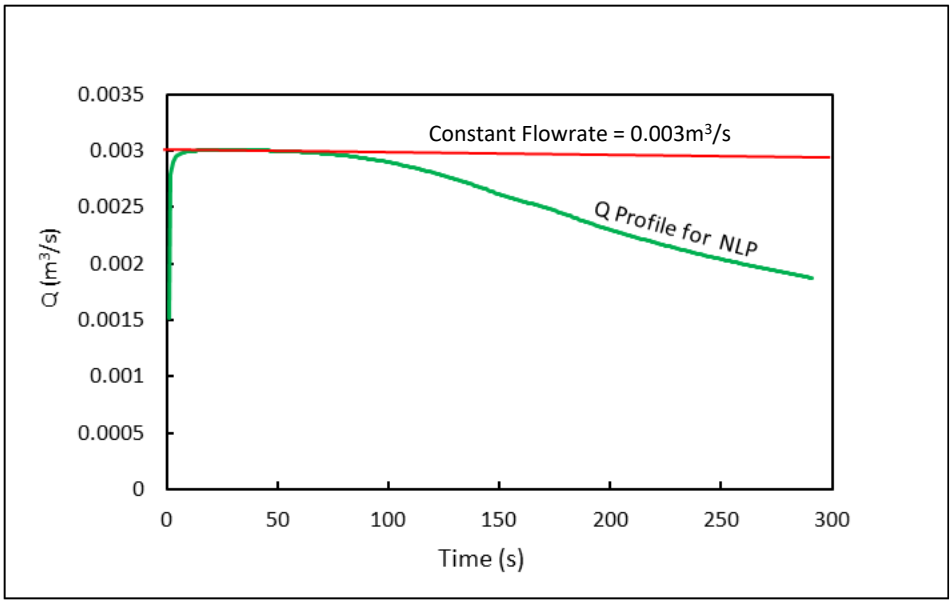

Figure 49. Comparison of Constant Flowrate with the Flowrate Profile of Discrete-Time NLP Solution Method for Test Case 1.

To compare the savings in the volume we study the minimum required flush volume for existing mode of operation (constant flowrate) with the optimum flowrate profile (discrete time NLP). Figure 50 illustrates the required flushing volume in gallons for the existing mode of operation and the proposed customized flowrate via discrete-time NLP solution approach. As observed the optimized flowrate by discrete-time NLP results in flush volume savings of over 30%

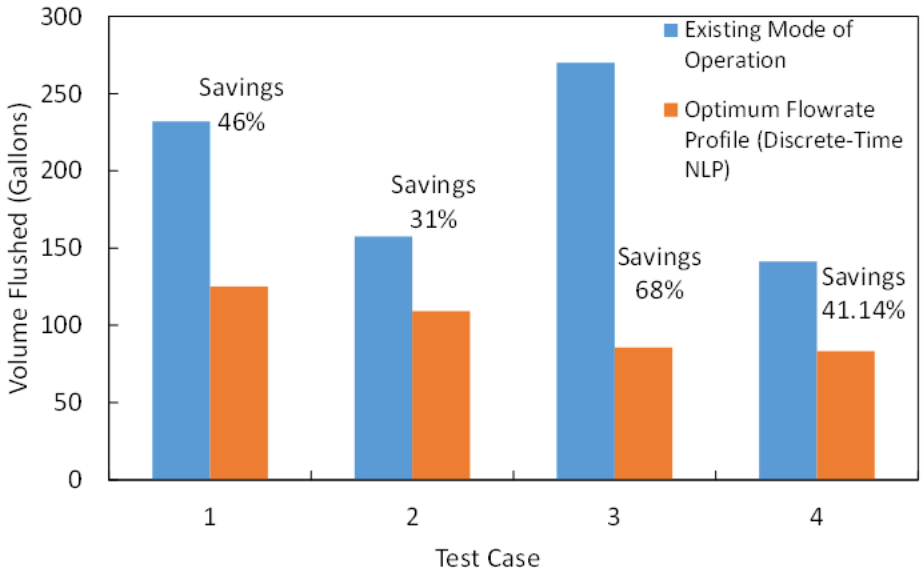

Figure 50. Comparison of Necessary Flushing Volume in Existing Mode of Operation and Discrete-Time NLP Solution Approach

Thus, we believe that this approach has great potentials to improve the resource conservation and the environmental footprint of these operations. Life cycle assessment (LCA) is a scientific method for systematically analyzing the environmental impact and the sustainability of various processes and products [128]–[131]. We studied the life cycle assessment of the optimized operation with the existing operation using SimaPro software.

We focus our calculations on the end-point assessment category considering human health (DALY), Ecosystem Quality (PDF*m^2*y), Climate Change (MT CO_2-eq), and resource (MJ primary). The obtained results are illustrated in Figure 51.

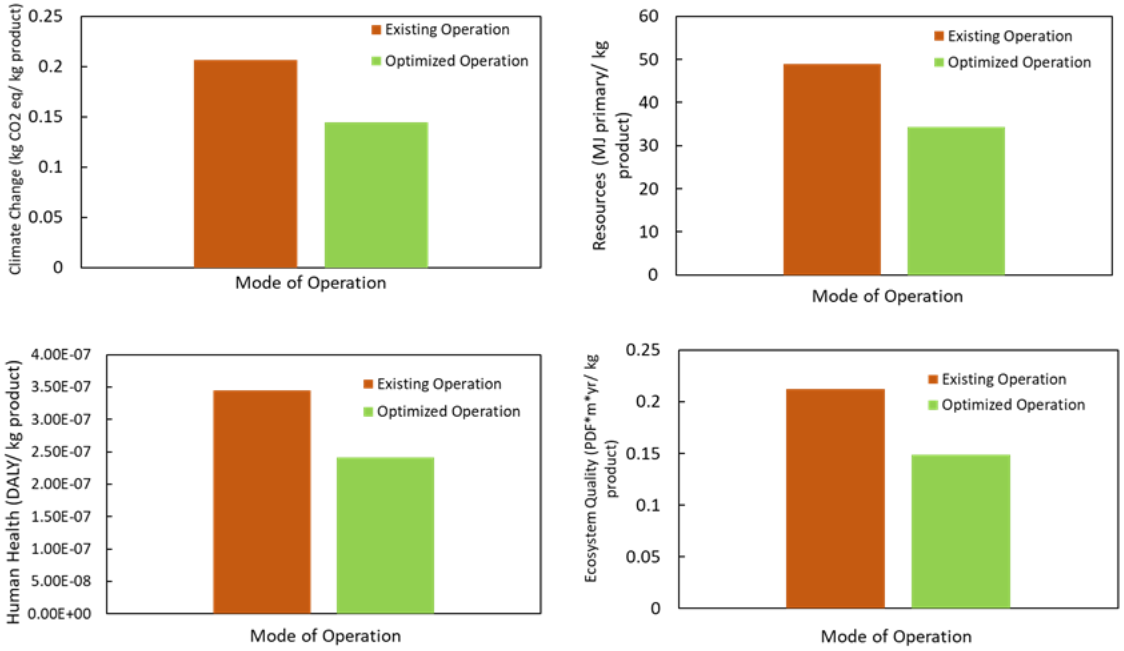

Figure 51. Life Cycle Assessment for Exiting Mode of Operation and Optimized Operation at Customized Flowrate

7.6 Conclusion

In this chapter, we confirmed the applicability of API – TDB recommended viscosity blending correlations for lubricant mixtures by gathering experimental data from known compositions of lube oil blends. In the recommended blending correlations by API-TDB, the viscosity of the mixture was calculated as the cubic average viscosity of the individual components of the mixture and correlated to their mole fractions. However, in this work we replaced the mole fractions with the mass fractions as both were

approximately the same for lube oil mixtures. The correlations demonstrated close agreement with experimental results, staying within a 5% margin of error. Additionally, we developed mathematical models based on first principles to represent the flushing operations. These models were validated using experimental data obtained from a collaborative lubricant blending plant, with the validation showing an agreement within a 7% error margin. For the optimization of the flushing operation, we approached it as an optimal control problem and employed two solution methods: Pontryagin's Maximum Principle and Discrete-Time Non-Linear Programming. While the Maximum Principle method had a considerably longer execution time, exceeding 70,000 seconds, and yielded unrealistic flushing time predictions, the discrete-time NLP solution approach completed in under 10 seconds and provided results that closely aligned with experimental data. Therefore, the discrete-time NLP solution approach holds significant potential for optimizing the trial-and-error-based flushing operation by minimizing the required flushing volume to meet the desired specifications. Our research presents a valuable strategy for applying optimal control theory and developing customized flowrate profiles for conducting an efficient flushing operation. This approach enables operators to make well-informed decisions, reducing operational downtime, and enhancing the economic, resource management, and environmental aspects of these processes.

To this end, in the subsequent chapter, Chapter 8, we delve into our third solution approach, which constitutes the data-driven method or machine learning approach, completing the three-pronged solution strategy.

Chapter 8

Data-Driven Approach

8.1 Fundamentals of Machine Learning

This chapter is committed to applying machine learning methodologies to analyze data from current operations and enhance the strategy for optimizing flushing operations. In this section, we discuss the foundational principles of ML systems, beginning with an examination of the diverse machine learning strategies that are widely adopted in the PSE domain.

8.1.1 Types of Machine Learning Algorithms

Supervised learning is a type of machine learning algorithm that uses labeled data in its training process [132], [133]. In this approach, both input data (features) and corresponding output data (target labels) are utilized to train a model. The model learns to map inputs to outputs and, once sufficiently trained, can use this mapping to predict the output for new, unseen inputs [134]. It is generally used in tasks such as regression, where continuous outputs are predicted, and classification, where outputs are discrete labels [135]. Common algorithms in supervised learning include linear regression, decision trees, random forests, support vector machines (SVM), and neural networks [136]–[141]

Conversely, unsupervised learning refers to a category of machine learning wherein the model is trained using datasets that lack labeled responses [142]. This implies that the training data is composed of input vectors devoid of associated target values. The primary objective of unsupervised learning is to unearth concealed patterns and intrinsic structures in the data [135]. Algorithms utilized in unsupervised learning predominantly engage in

clustering or grouping data points into separate clusters or working to reduce the data's dimensionality to identify critical attributes [143]. Typical techniques in unsupervised learning encompass K-means clustering, hierarchical clustering, and principal component analysis (PCA) [144]. This approach is largely adopted when there is an abundance of data and the aim is to decode hidden patterns without being directed towards a specific predictive task [145].

Reinforcement Learning (RL) represents another class within the machine learning spectrum where an agent learns to take decisions in a specific environment predicated on feedback, manifested through rewards or penalties [146]. The principal objective for RL algorithms is to refine the actions undertaken by the agent to sequentially augment the cumulative rewards over a period [147]. RL holds substantial merit in contexts where finding the optimal solution demands a significant extent of exploratory efforts and a trial-and-error approach [148]. Prominent techniques in RL encompass Q-learning, deep Q-networks (DQN), and policy gradients [149].

8.1.2 Feature Selection and Dimensionality Reduction

Feature selection plays a pivotal role in boosting the precision of predictive models by pinpointing the most appropriate variables and refining the dataset. Filter methods, one such strategy, examine features individually through measures like correlation and mutual information [150]. These criteria determine the relationship of each feature to the outcome variable, facilitating the choice of features with the strongest correlation. There are also iterative methods that assess sets of features based on the performance of a specified model. Familiar iterative strategies encompass forward selection, backward elimination, and recursive feature elimination.

Dimensionality reduction methods optimize expansive datasets, supporting the efficiency of predictive models and optimizing computational efficiency. Principal Component Analysis (PCA) [151] stands out as a commonly utilized linear technique that determines main components or chief directions that capture the most significant data variation. While reducing the data dimensions, PCA preserves a substantial portion of the original data's variation [152]. In addition to the above, techniques such as feature agglomeration and manifold learning are employed to group features based on their similarities, while maintaining complex relationships within the data [135].

8.1.3 Model Validation and Evaluation

Model validation involves verifying how well a trained machine learning model performs on unseen data. The primary aim here is to detect and prevent issues such as overfitting or underfitting [153]. It generally involves using a separate dataset (validation set) not seen by the model during training. Strategies for model validation include:

Train-Validation-Test Split: Splitting the data into training, validation, and testing sets to fine-tune the model parameters and assess its performance.

Cross-Validation: Utilizing techniques such as k-fold cross-validation and stratified K-fold cross validation to use different subsets of the data for training and validation, helping to ensure the robustness of the model [154].

In K-fold cross-validation, the dataset is randomly partitioned into 'k' equal-sized subsets. Of the 'k' subsets, a single subset is retained as the validation data for testing the model, and the remaining 'k-1' subsets are used as training data. The cross-validation process is then repeated 'k' times, with each of the 'k' subsets used exactly once as the validation data. The 'k' results can then be averaged to produce a single estimation. K-fold

cross validation is used when the distribution of target variable classes is roughly equal. However, a drawback is that K-fold cross validation does not guarantee that the distribution of the target variable is maintained across all the folds.

In stratified K-fold cross-validation, like k-fold, the data is divided into 'k' folds. However, stratified k-fold cross-validation ensures that each fold has the same distribution of the target variable as the entire dataset. This is achieved by splitting the data such that each fold has roughly the same percentage of samples of each target class as the complete dataset. Hence, it is specifically useful when we have imbalanced classes in our dataset. stratified K-fold cross-validation ensures that each fold is a good representative of the overall dataset.

Model evaluation is the process of assessing the predictive performance of a model using specific metrics [155]. It's carried out after model validation, using a testing dataset that wasn't involved in the training or validation processes. Key aspects include:

Performance Metrics: Depending on the type of problem (classification, regression, etc.), different metrics are used, including accuracy, precision, recall, F1-score for classification problems, and Mean Absolute Error (MAE), Mean Squared Error (MSE) for regression problems [156].

Confusion Matrix: In classification problems, a confusion matrix is often used to understand the performance of the algorithm, mainly for binary classification problems [157]. A confusion matrix is typically a 2x2 matrix for binary classification problems. It consists of four entries:

True Positive (TP): The cases where the model predicted the positive class correctly.

True Negative (TN): The cases where the model predicted the negative class correctly.

False Positive (FP): The cases where the model predicted the positive class incorrectly (i.e., it was actually the negative class).

False Negative (FN): The cases where the model predicted the negative class incorrectly (i.e., it was actually the positive class).

From the confusion matrix, several important metrics that give insight into the performance of the classifier can be derived. These include:

1. Accuracy: (TP + TN) / (TP + TN + FP + FN)

This metric gives us a general idea of how often the model is correct in its predictions. It is calculated as the number of correct predictions divided by the total number of predictions. It is essential to get a high-level view of the model performance but sometimes can be misleading, especially when the classes are imbalanced.

2. Precision: TP / (TP + FP)

Precision focuses on the positive predictions made by the model, calculated as the number of true positives divided by the total number of true positives and false positives. It essentially quantifies the correctness of the model in predicting positive cases. High precision indicates a low rate of false-positive errors.

3. Recall: TP / (TP + FN)

Also known as sensitivity or true positive rate, recall is computed as the number of true positives divided by the total number of true positives and false negatives. This metric tells us how well the model is identifying positive cases. A high recall value indicates that the model catches most of the positive cases, but it might also have a high number of false positives.

4. F1 score: 2 *(Precision * Recall) / (Precision + Recall)

The F1 score is the harmonic mean of precision and recall, and it gives a balance between the two metrics. It is particularly useful when dealing with imbalanced datasets as it considers both false positives and false negatives. A higher F1 score indicates a more robust model.

8.2 Data Acquisition and Preprocessing

In collaboration with our partnered facility, we undertook a rigorous and systematic approach to data acquisition with the primary objective of developing a machine learning classification model. This model was based on a dataset inclusive of 14 distinctive features — variables that capture the necessary information for predictive analysis. To adopt predictive accuracy, the dataset was separated into features and labels. 'Features' refer to the independent variables, which consisted of the crucial data points helpful in making predictions. Concurrently, 'labels' denote the dependent variables that we intended to predict, essentially representing the categorical outcomes we aimed to accurately forecast through the model. In the development phase, we utilized both the feature data and label data in a learning process whereby the model established the correlations and underlying patterns that gave the relationship between the features and labels. This learning phase was important as it enabled the model to accurately classify new, unseen data, relying on the understanding it had cultivated during the training process. Our objective was to fine-tune this classification model to a state of optimal precision, wherein it can reliably analyze and categorize new data based on the foundational learning from the existing dataset. Our dataset initially contained 14 features with 1426 datapoints. These features included, production number, production line, date of production, time of production, the

name of the product, source tank number, product family classification, the system type, the code for bulk items, the documented volume of the flush, the outcome of the flush noted as either 'pass' or 'fail', kinematic viscosity measured at both 40°C and 100°C, and the average ambient temperature at the time.

In our endeavor to focus on the most crucial factors, we decided to exclude certain features that did not significantly affect the model's performance. Consequently, we narrowed down our dataset to encompass just the kinematic viscosity values recorded at 40°C and 100°C, the ambient temperature, the specific production line in use, the system type, and the ultimate outcome of the flush, distinguished as a 'pass' or 'fail'. This decision to include kinematic viscosity was grounded in the fundamental role that kinematic viscosity plays in determining lube oil quality, with the specific temperatures of 40°C and 100°C being chosen in adherence to ISO and ASTM guidelines to accurately represent the viscosity-temperature behavior of the oil across a broad temperature spectrum.

The inclusion of the average ambient temperature as a significant feature was motivated by our interest in examining how seasonal variations could potentially influence the outcomes of 'pass' or 'fail'. Similarly, the distinct production lines were identified as crucial given the existence of diverse family categories, each facilitated by its unique filter setup. These lines, characterized by varying lengths, eventually converge at a juncture to form a unified line leading to the drum filling station. This integrated segment is termed as the drum filling line, whereas the individual pathways feeding into it are referred to as family lines, a structural layout detailed in Figure 52.

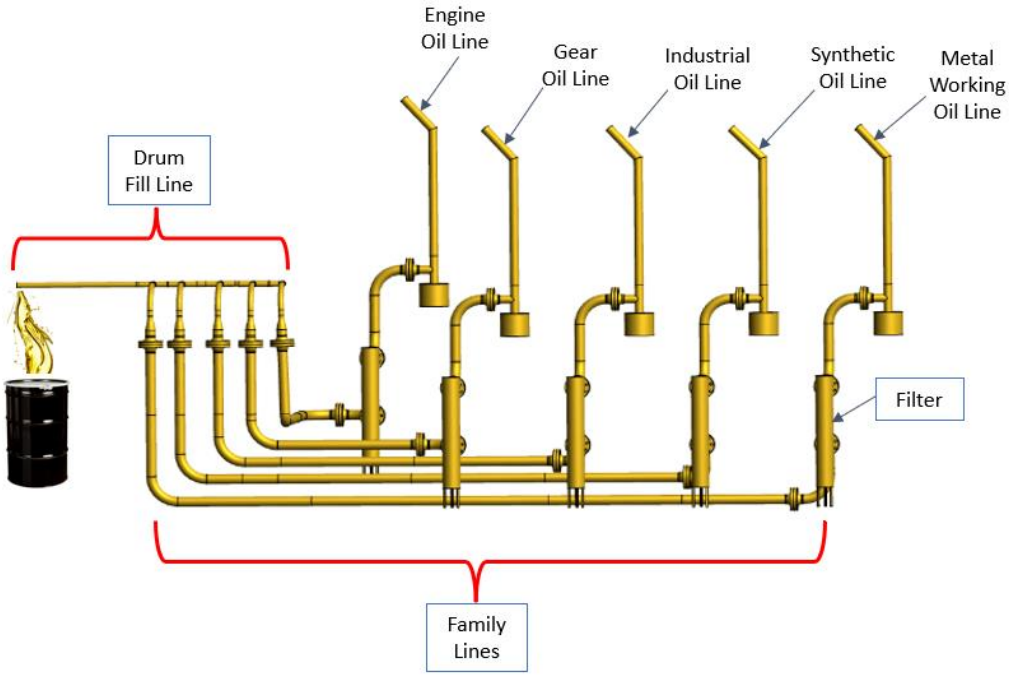

Figure 52. The Drum Filling Station Depicting the Different Family Lines, Filters and the Common Drum Filling Line

Continuing with the description of our system, we noted that different pipe lengths correspond to varying system volumes. This insisted us to delve deeper to understand the effects of these system volumes on the successful execution of the flushing process. Alongside, we integrated a feature termed ‘system type’ in our analysis to denote the nature of the mixture produced during the flushing operation; it could be a mixture involving two or three different oils. This is determined based on two potential scenarios that arise during changeovers. In the first scenario, both the residual and the upcoming products belong to the same family, resulting in a two-oil system. Contrastingly, the second scenario involves products from different families, leading to a three-oil system as the upcoming batch mixes with residues from both the family and drum fill lines. Our analysis is designed to

accommodate these complexities, offering a robust mechanism to predict the 'pass' or 'fail' outcomes precisely.

In the subsequent phase, we implemented feature scaling, a pivotal preprocessing procedure in machine learning. This step was essential to standardize the range of independent variables or features of the data. By scaling the features, we ensured that each one contributes equally to the performance of the model, fostering better convergence during training and a balanced influence on the output predictions. Feature scaling is particularly critical in algorithms that involve distance computations and gradient descent optimization as it helps in accelerating the learning process and finding a more precise optimum. Moreover, it aids in mitigating the challenges posed by features that are measured in different units or scales, thereby facilitating a harmonious and more effective modeling environment.

Following that, we undertook the process of feature encoding, an essential preparatory step in the refinement of our dataset tailored for the requisites of classification models in machine learning. This process is helpful in transforming categorical data, which is often in text format, into a numerical format that can be more readily analyzed and processed by machine learning algorithms. Given that machine learning models predicate their functioning on mathematical equations and numerical computations, having data in a numerical format becomes a prerequisite to train the model effectively. By converting these categorical values into a numerical format, we facilitate the model's understanding of the different categories within a feature, hence empowering it to find potential patterns and correlations that are fundamentally vital in making accurate predictions. Moreover, feature encoding aids in the optimal utilization of computational resources by presenting data in a

manner that is streamlined for processing, raising efficiency and precision in the predictive analytics of the classification model.

8.3 Model Development

We developed a random forest classification model, splitting the data into 80% training set 20% testing set. Notably, our dataset contains a substantially higher number of 'pass' instances compared to 'fail' ones. To circumvent any potential bias stemming from this imbalance, we adopted ‘stratified splitting’ during the partitioning process. This approach ensures a proportionate representation of both 'pass' and 'fail' categories in each subset, thus avoiding the risk of developing a model skewed towards predicting the 'pass' outcome predominantly.

To substantiate the accuracy of our model, we implemented stratified K-fold cross-validation, a procedure pivotal in the fine-tuning of classification models. In this context, 'K' explains the number of groups that the training dataset is divided into, a number we established as 10 for our model. The stratified nature of this cross-validation means that each fold is a good representative of the overall distribution of 'pass' and 'fail' instances, safeguarding the reliability and integrity of our predictive model by minimizing bias and variance. Moreover, it enables a more comprehensive exploration of the data space, since each data point gets to be in the testing set exactly once and in the training set K-1 times, thus facilitating a more robust assessment of the model's performance. The choice of K holds substantial significance; a higher value of K entails a more exhaustive evaluation but at the cost of increased computational resources and time. Therefore, setting K to 10 strikes a balanced chord between computational efficiency and obtaining a well-rounded insight into the model’s predictive prowess.

Following the cross-validation process, we undertook a feature importance analysis, a critical step to comprehend how individual features influence the predictive capacity of our classification model. Analyzing feature importance is integral in improving the precision of classification models as it outlines the distinct impact each feature exerts on the predictive outcomes. By examining the weightage accorded to each feature, we can pinpoint the variables that are paramount in determining the 'pass' or 'fail' outcomes, thereby enhancing our understanding of the underlying patterns and relationships within the data.

8.4 Model Results and Discussion

8.4.1 Confusion Matrix

To evaluate our model results, we applied a confusion matrix (illustrated in Figure 52) methodology for estimating the reported success and failure scenarios. This approach is pivotal in developing a deeper comprehension of the performance of the classification model, as it facilitates a comprehensive view of the different classes of outcomes – namely true positives (TP), true negatives (TN), false positives (FP), and false negatives (FN).

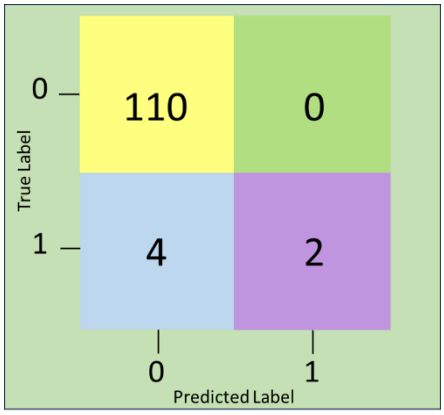

Figure 53. Confusion Matrix of the Formulated Random Forest Classification Model (‘0’ represents successful flushes while ‘1’ represents failed scenarios)

Table 13

Performance of the Random Forest Classification Model

Model Performance	**Value**
Total Test Records	116
Correctly Predicted	110
Model Accuracy	0.94
Recall Value	1.0
Precision	0.94
F1 score	0.97

In this context, we defined a 'true positive' as a scenario where the model correctly identified a successful flush operation, symbolized by a '0'. Conversely, a 'true negative,' represented by a '1,' would imply a correctly identified failure of the flushing operation.

Our analysis also takes into account false negatives and false positives, which denote incorrect predictions of pass and fail scenarios, respectively. On exploring the findings, it was observed that the model projected 110 true positives, a more than satisfactory outcome demonstrating the high number of successful predictions of pass scenarios, mirroring the actual recorded data of 110 successful flush operations. Furthermore, the true negative cases were zero, denoting the absence of correctly identified fail instances. This is mirrored in the false negative predictions also standing at zero, showcasing that no successful operation was mistakenly categorized as a failure. However, there were 6 false positive predictions, indicating a slight tendency of the model to mistakenly identify successful operations as failures. The real data affirms the occurrence of 6 complete failure instances in the flushing operations. Drawing comparisons with the real data shows a high recall value of 1, signifying that all the positive instances were accurately identified, a praiseworthy achievement spotlighting the model's sensitivity in correctly identifying all successful flush operations. Moving forward to precision and accuracy values, both stood at 0.94. The precision value explains that the model had a high accuracy in predicting the pass scenarios; however, it still registered a minor fraction as false positives, explaining a room for refinement to mitigate such errors. The accuracy value of 0.94 indicates a strong concurrence between the predictions and the actual data, confirming the reliability of the model in predicting the outcomes correctly for a significant majority of the cases.

8.4.2 K-fold Cross Validation

The stability observed in the outcomes generated from our random forest classification model is largely due to the implementation of stratified K-fold cross-validation. This technique is central in strengthening the model's reliability and precision.

In this setting, 'K' signifies the number of subsets that the data sample is partitioned into; our model utilized a 10-fold cross-validation, implying the data was divided into 10 groups. This structured approach permits the model to be trained across diverse segments of the data, thereby enhancing its proficiency in accurately predicting unseen data. Consequently, it achieved a mean accuracy score of 0.93 through this validation process, a figure nearly identical to the 0.94 score recorded using the test dataset. Utilizing this method not only promotes an optimized use of the data at hand but also provides a trustworthy assessment of the model's operational efficacy, a fact corroborated by the close agreement between the cross-validation and test accuracies in our evaluation. In conclusion, the harmonized accuracy scores of 0.93 and 0.94 not only validate the effective deployment of stratified K-fold cross-validation but also highlight its indispensable role in enhancing the robustness and predictive accuracy of our random forest classification model.

8.4.3 Feature Importance

In the context of random forest classification, understanding feature importance is pivotal as it helps in identifying which variables are most consequential in predicting the output. Essentially, it offers insights into the relative contribution of each feature in the decision-making process of the model. Each feature in the dataset is assigned a score on this scale, derived from the model’s learning on how crucial that specific feature is in predicting the target variable accurately. These scores are computed based on how much the prediction error increases when the feature's values are permuted. The more error increases, the more important the feature is considered to be, as it indicates that the model relies heavily on that feature to make accurate predictions.

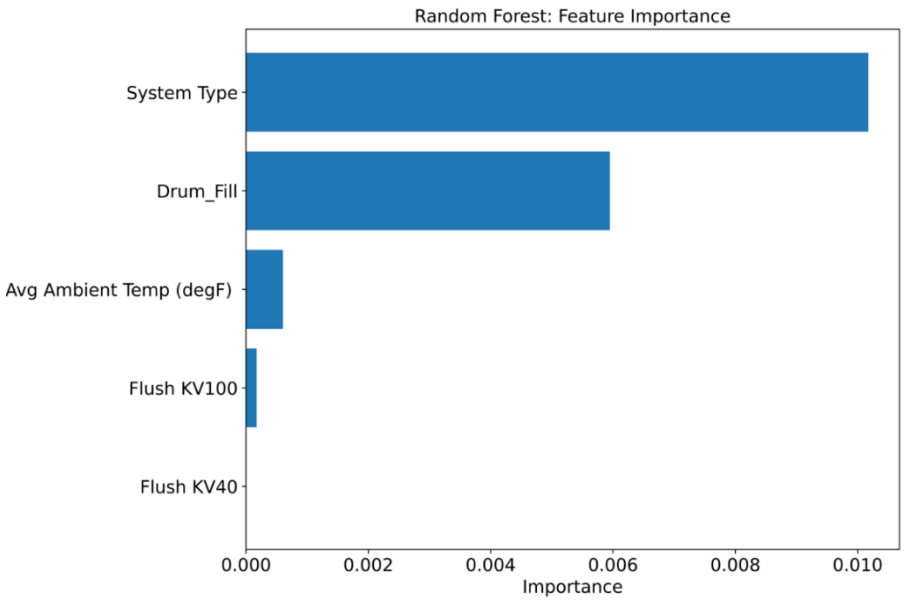

Figure 54. Feature Importance of the Developed Classifier Model

The analysis of feature importance revealed that the 'system type' exerted the most substantial influence on the model, followed sequentially by the 'drum fill' variable and the 'average ambient temperature.Understanding the hierarchy of feature importance not only equips us with the knowledge to refine the model for better accuracy but also fosters a deeper understanding of the underlying patterns and relationships within the data, offering a robust pathway to the development of more intuitive and efficient predictive tools.

8.5 Conclusions

We developed a random forest classification model aimed at accurately determining the success or failure outcomes of the flushing operations. The notable accuracy achieved through the application of stratified K-fold cross-validation underscores the model's substantial reliability.

However, the model exhibits a significant area for enhancement, evidenced by the null results for both true and false negatives. This reflects the model's current shortfall in effectively identifying failure cases, pinpointing a critical area where the sensitivity of the model needs amplification. Addressing this will pave the way for a more comprehensive understanding and prediction of both success and failure events, fostering a more detailed approach to predicting different outcomes.

In conclusion, the incorporation of a confusion matrix in our analysis has proven vital in explaining the specific performance metrics of our classification model. This tool has enabled a deep dive into the true dynamics of the predictions made, laying down a path for further refining the model. Enhancing both its sensitivity and precision will indeed be a significant step towards achieving a well-rounded predictive accuracy in subsequent analyses.

Chapter 9

Summary and Future Work

This dissertation unfolds a new perspective of implementing a comprehensive strategy that integrates experimental characterization, the principles of process systems engineering, and data-driven machine learning methodologies for enhancing the process efficiency and thereby implementing sustainable manufacturing practices.

9.1 Effective Synthesis Approaches for Renewable Energy Resources: Perovskite Solar Cells

We have introduced a strategy facilitated by computer-aided synthesis for the discovery of innovative material alternatives suitable for the fabrication of perovskite solar cells, aiming for improved stability, higher efficiency, and controlled costs. This work addresses the challenges of formulating PSCs with reduced costs and toxicity, and enhanced power conversion efficiency, longevity, and environmental sustainability. Central to our approach is the optimized synthesis problem that guides the identification of new organic-inorganic substitutes for perovskite crystals through advanced computer-aided molecular design.

The research unfolds a computer-aided design synthesis route, enabling the selection of novel candidates for the positions A, B, and X in the ABX_3 chemical structure of the perovskite crystal. This framework provides the flexibility to opt for individual materials for sites A, B, and C, predicated on stability and cost-efficiency considerations, thus laying a solid groundwork for further explorations. Based on this foundation, the

strategy can be expanded to find the integration of varied material combinations at each site, potentially encompassing mixed cation and mixed anion perovskites.

Moreover, this approach is adaptive to encompass additional evaluative parameters including efficiency metrics, safety protocols, and environmental impacts, thereby facilitating a comprehensive multi-objective function analysis. Consequently, this defines a path not only for the optimized selection of materials but also towards a broader understanding and fulfillment of overarching objectives such as safety and sustainability.

9.2 Efficient Packaging Operations for Downstream Petroleum Processes – Lube Oil Blending Plants

This research investigates the long-standing and economically significant issue of cross-contamination during production changeovers in multiproduct plants — a challenge that has persistently hindered operational efficiency for extended periods. Given the limited body of existing literature in this area, we developed a comprehensive methodology that combines process systems engineering with experimental characterization and data-driven approaches.

During our investigation, we studied a variety of innovative and general improvement methods, including the introduction of pipeline coatings, gel pigs, modern filter designs, fluid blasting, and vibration cleaning strategies. These alternatives have the potential of minimizing oil hold-up in the system and reducing both cross-contamination and product downgrading, thus enabling improved operational efficiency.

Building on this, through strategic data analysis and partnership with industry, we studied the drawbacks of traditional techniques. This analysis facilitated the development

of a pilot plant, essentially replicating a commercial facility, which enabled the performance of well-structured experiments. Within this framework, we examine improved operational procedures and formulate strategies for raising enhancements to a commercial level, aiming to guide transformative changes in industry practices.

This work also studies a process systems engineering approach of formulating the flushing operation as an optimal control problem and developing methodologies for conducting the operations at a customized flowrate. Thereby enhancing efficiency and reducing product downgrading.

Our work presents a methodical roadmap to assist industries in making informed decisions. Thereby enabling a significant improvement in operational efficiency coupled with enhanced resource management and a reduced environmental footprint. This work, therefore, stands as a pioneering initiative, guiding industries towards a horizon defined by informed decisions and sustainable operations.

Looking ahead, we plan to enhance our developed models by incorporating additional factors such as viscosity, diffusion coefficients, and frictional losses, which are pivotal in fluid hydrodynamics. Additionally, we aim to explore the transferability of our solution approach to other sectors with similar operational procedures, including the specialty chemical industry, food production, personal care product manufacturing, and the pharmaceutical industry.

References

[1] W. Qi, Z. Huang, H. Dinçer, R. Korsakienė, and S. Yüksel, "Corporate Governance-Based Strategic Approach to Sustainability in Energy Industry of Emerging Economies with a Novel Interval-Valued Intuitionistic Fuzzy Hybrid Decision Making Model," *Sustainability*, vol. 12, no. 8, Art. no. 8, Jan. 2020, doi: 10.3390/su12083307.

[2] T. C. Ng and M. Ghobakhloo, "Energy sustainability and industry 4.0," *IOP Conf. Ser. Earth Environ. Sci.*, vol. 463, no. 1, p. 012090, Mar. 2020, doi: 10.1088/1755-1315/463/1/012090.

[3] A. Wilkinson, M. Hill, and P. Gollan, "The sustainability debate," *Int. J. Oper. Prod. Manag.*, vol. 21, no. 12, pp. 1492–1502, Jan. 2001, doi: 10.1108/01443570110410865.

[4] H. Afshari, S. Agnihotri, C. Searcy, and M. Y. Jaber, "Social sustainability indicators: A comprehensive review with application in the energy sector," *Sustain. Prod. Consum.*, vol. 31, pp. 263–286, May 2022, doi: 10.1016/j.spc.2022.02.018.

[5] P. Sicard, E. Agathokleous, S. C. Anenberg, A. De Marco, E. Paoletti, and V. Calatayud, "Trends in urban air pollution over the last two decades: A global perspective," *Sci. Total Environ.*, vol. 858, p. 160064, Feb. 2023, doi: 10.1016/j.scitotenv.2022.160064.

[6] R. Thompson *et al.*, "Air pollution and human cognition: A systematic review and meta-analysis," *Sci. Total Environ.*, vol. 859, p. 160234, Feb. 2023, doi: 10.1016/j.scitotenv.2022.160234.

[7] S. Madhav *et al.*, "Water Pollutants: Sources and Impact on the Environment and Human Health," in *Sensors in Water Pollutants Monitoring: Role of Material*, D. Pooja, P. Kumar, P. Singh, and S. Patil, Eds., in Advanced Functional Materials and Sensors. , Singapore: Springer, 2020, pp. 43–62. doi: 10.1007/978-981-15-0671-0_4.

[8] Y. Li, L. Ni, Y. Guo, X. Zhao, Y. Dong, and Y. Cheng, "Challenges and Opportunities to Treat Water Pollution," in *Paths to Clean Water Under Rapid Changing Environment in China*, Y. Li, L. Ni, Y. Guo, X. Zhao, Y. Dong, and Y. Cheng, Eds., in SpringerBriefs in Water Science and Technology. , Singapore: Springer Nature, 2022, pp. 13–42. doi: 10.1007/978-981-19-0091-4_2.

[9] A. Zakari, I. Khan, D. Tan, R. Alvarado, and V. Dagar, "Energy efficiency and sustainable development goals (SDGs)," *Energy*, vol. 239, p. 122365, Jan. 2022, doi: 10.1016/j.energy.2021.122365.

[10] M. F. Hordeski, *New Technologies for Energy Efficiency*. CRC Press, 2021.

[11] A. Talaei, A. O. Oni, M. Ahiduzzaman, P. S. Roychaudhuri, J. Rutherford, and A. Kumar, “Assessment of the impacts of process-level energy efficiency improvement on greenhouse gas mitigation potential in the petroleum refining sector,” *Energy*, vol. 191, p. 116243, Jan. 2020, doi: 10.1016/j.energy.2019.116243.

[12] Y. Meng, Y. Yang, H. Chung, P.-H. Lee, and C. Shao, “Enhancing Sustainability and Energy Efficiency in Smart Factories: A Review,” *Sustainability*, vol. 10, no. 12, Art. no. 12, Dec. 2018, doi: 10.3390/su10124779.

[13] E. Kabir, P. Kumar, S. Kumar, A. A. Adelodun, and K.-H. Kim, “Solar energy: Potential and future prospects,” *Renew. Sustain. Energy Rev.*, vol. 82, pp. 894–900, Feb. 2018, doi: 10.1016/j.rser.2017.09.094.

[14] A. Palacios, C. Barreneche, M. E. Navarro, and Y. Ding, “Thermal energy storage technologies for concentrated solar power – A review from a materials perspective,” *Renew. Energy*, Nov. 2019, doi: 10.1016/j.renene.2019.10.127.

[15] M. Imtiaz Hussain, C. Ménézo, and J.-T. Kim, “Advances in solar thermal harvesting technology based on surface solar absorption collectors: A review,” *Sol. Energy Mater. Sol. Cells*, vol. 187, pp. 123–139, Dec. 2018, doi: 10.1016/j.solmat.2018.07.027.

[16] X. Peng, T. W. Root, and C. T. Maravelias, “Storing solar energy with chemistry: the role of thermochemical storage in concentrating solar power,” *Green Chem.*, vol. 19, no. 10, pp. 2427–2438, 2017, doi: 10.1039/C7GC00023E.

[17] A. Louwen, W. G. J. H. M. van Sark, A. P. C. Faaij, and R. E. I. Schropp, “Re-assessment of net energy production and greenhouse gas emissions avoidance after 40 years of photovoltaics development,” *Nat. Commun.*, vol. 7, no. 1, pp. 1–9, Dec. 2016, doi: 10.1038/ncomms13728.

[18] A. K. Pandey, V. V. Tyagi, J. A. Selvaraj, N. A. Rahim, and S. K. Tyagi, “Recent advances in solar photovoltaic systems for emerging trends and advanced applications,” *Renew. Sustain. Energy Rev.*, vol. 53, pp. 859–884, Jan. 2016, doi: 10.1016/j.rser.2015.09.043.

[19] L. El Chaar, L. A. lamont, and N. El Zein, “Review of photovoltaic technologies,” *Renew. Sustain. Energy Rev.*, vol. 15, no. 5, pp. 2165–2175, Jun. 2011, doi: 10.1016/j.rser.2011.01.004.

[20] Q. Tai, K.-C. Tang, and F. Yan, “Recent progress of inorganic perovskite solar cells,” *Energy Environ. Sci.*, vol. 12, no. 8, pp. 2375–2405, Aug. 2019, doi: 10.1039/C9EE01479A.

[21] S. J. C. Irvine, V. Barrioz, D. Lamb, E. W. Jones, and R. L. Rowlands-Jones, “MOCVD of thin film photovoltaic solar cells—Next-generation production technology?,” *J. Cryst. Growth*, vol. 310, no. 23, pp. 5198–5203, Nov. 2008, doi: 10.1016/j.jcrysgro.2008.07.121.

[22] A. Le Donne, V. Trifiletti, and S. Binetti, “New Earth-Abundant Thin Film Solar Cells Based on Chalcogenides,” *Front. Chem.*, vol. 7, 2019, doi: 10.3389/fchem.2019.00297.

[23] J. Cui *et al.*, “Recent progress in efficient hybrid lead halide perovskite solar cells,” *Sci. Technol. Adv. Mater.*, vol. 16, no. 3, p. 036004, Jun. 2015, doi: 10.1088/1468-6996/16/3/036004.

[24] B. V. Lotsch, “New Light on an Old Story: Perovskites Go Solar,” *Angew. Chem. Int. Ed.*, vol. 53, no. 3, pp. 635–637, 2014, doi: 10.1002/anie.201309368.

[25] National Renewable Energy Laboratory (NREL), “Best Research-Cell Efficiency Chart.” Accessed: Nov. 20, 2023. [Online]. Available: https://www.nrel.gov/pv/cell-efficiency.html

[26] A. Kojima, K. Teshima, T. Miyasaka, and Y. Shirai, “Novel Photoelectrochemical Cell with Mesoscopic Electrodes Sensitized by Lead-Halide Compounds (2),” *Meet. Abstr.*, vol. MA2006-02, no. 7, pp. 397–397, Jun. 2006, Accessed: Oct. 17, 2019. [Online]. Available: http://ma.ecsdl.org/content/MA2006-02/7/397

[27] A. Kojima, K. Teshima, Y. Shirai, and T. Miyasaka, “Organometal Halide Perovskites as Visible-Light Sensitizers for Photovoltaic Cells,” *J. Am. Chem. Soc.*, vol. 131, no. 17, pp. 6050–6051, May 2009, doi: 10.1021/ja809598r.

[28] H.-S. Kim *et al.*, “Lead Iodide Perovskite Sensitized All-Solid-State Submicron Thin Film Mesoscopic Solar Cell with Efficiency Exceeding 9%,” *Sci. Rep.*, vol. 2, p. 591, Aug. 2012, doi: 10.1038/srep00591.

[29] M. M. Lee, J. Teuscher, T. Miyasaka, T. N. Murakami, and H. J. Snaith, “Efficient Hybrid Solar Cells Based on Meso-Superstructured Organometal Halide Perovskites,” *Science*, vol. 338, no. 6107, pp. 643–647, Nov. 2012, doi: 10.1126/science.1228604.

[30] H. J. Snaith, “Present status and future prospects of perovskite photovoltaics,” *Nat. Mater.*, vol. 17, no. 5, pp. 372–376, May 2018, doi: 10.1038/s41563-018-0071-z.

[31] S. Yang, W. Fu, Z. Zhang, H. Chen, and C.-Z. Li, “Recent advances in perovskite solar cells: efficiency, stability and lead-free perovskite,” *J. Mater. Chem. A*, vol. 5, no. 23, pp. 11462–11482, 2017, doi: 10.1039/C7TA00366H.

[32] S. Dastidar *et al.*, “High Chloride Doping Levels Stabilize the Perovskite Phase of Cesium Lead Iodide,” *Nano Lett.*, vol. 16, no. 6, pp. 3563–3570, Jun. 2016, doi: 10.1021/acs.nanolett.6b00635.

[33] M. Saliba *et al.*, “Cesium-containing triple cation perovskite solar cells: improved stability, reproducibility and high efficiency,” *Energy Environ. Sci.*, vol. 9, no. 6, pp. 1989–1997, 2016, doi: 10.1039/C5EE03874J.

[34] S. Gholipour and M. Saliba, “From Exceptional Properties to Stability Challenges of Perovskite Solar Cells,” *Small*, vol. 14, no. 46, p. 1802385, 2018, doi: 10.1002/smll.201802385.

[35] M. Kulbak *et al.*, “Cesium Enhances Long-Term Stability of Lead Bromide Perovskite-Based Solar Cells,” *J. Phys. Chem. Lett.*, vol. 7, no. 1, pp. 167–172, Jan. 2016, doi: 10.1021/acs.jpclett.5b02597.

[36] A. K. Jena, A. Kulkarni, and T. Miyasaka, “Halide Perovskite Photovoltaics: Background, Status, and Future Prospects,” *Chem. Rev.*, vol. 119, no. 5, pp. 3036–3103, Mar. 2019, doi: 10.1021/acs.chemrev.8b00539.

[37] G. E. Eperon *et al.*, “Inorganic caesium lead iodide perovskite solar cells,” *J. Mater. Chem. A*, vol. 3, no. 39, pp. 19688–19695, Sep. 2015, doi: 10.1039/C5TA06398A.

[38] J. Rauch, *Multiproduct Plants*, 1., Edition. Weinheim: Wiley-VCH Verlag & Co, 2003.

[39] H. E. Salomone, J. M. Montagna, and O. A. Iribarren, “A Simulation Approach to the Design and Operation of Multiproduct Batch Plants,” *Chem. Eng. Res. Des.*, vol. 75, no. 4, pp. 427–437, May 1997, doi: 10.1205/026387697523895.

[40] M. Zlokarnik, *Stirring: Theory and Practice*, 1st ed. Wiley, 2001. doi: 10.1002/9783527612703.

[41] C.-J. Yu, “Advances in modelling and simulation of halide perovskites for solar cell applications,” *J. Phys. Energy*, vol. 1, no. 2, p. 022001, Jan. 2019, doi: 10.1088/2515-7655/aaf143.

[42] J. M. Ball *et al.*, “Supplementary Information for ‘Optical Properties and Limiting Photocurrent of Thin-Film Perovskite Solar Cells,’” p. 15.

[43] P. M. Kaminski, P. J. M. Isherwood, G. Womack, and J. M. Walls, “Optical Optimization of Perovskite Solar Cell Structure for Maximum Current Collection,” *Energy Procedia*, vol. 102, pp. 11–18, Dec. 2016, doi: 10.1016/j.egypro.2016.11.312.

[44] X. Sun, R. Asadpour, W. Nie, A. D. Mohite, and M. A. Alam, “A Physics-Based Analytical Model for Perovskite Solar Cells,” *IEEE J. Photovolt.*, vol. 5, no. 5, pp. 1389–1394, Sep. 2015, doi: 10.1109/JPHOTOV.2015.2451000.

[45] S. Lu, Q. Zhou, Y. Ouyang, Y. Guo, Q. Li, and J. Wang, “Accelerated discovery of stable lead-free hybrid organic-inorganic perovskites via machine learning,” *Nat. Commun.*, vol. 9, no. 1, p. 3405, Dec. 2018, doi: 10.1038/s41467-018-05761-w.

[46] Y. G. Yoo *et al.*, “Evaluating the environmental impact of the lead species in perovskite solar cells via environmental-fate modeling,” *J. Ind. Eng. Chem.*, vol. 70, pp. 453–461, Feb. 2019, doi: 10.1016/j.jiec.2018.11.008.

[47] L. Qiu, L. K. Ono, and Y. Qi, “Advances and challenges to the commercialization of organic–inorganic halide perovskite solar cell technology,” *Mater. Today Energy*, vol. 7, pp. 169–189, Mar. 2018, doi: 10.1016/j.mtener.2017.09.008.

[48] Y. Da, Y. Xuan, and Q. Li, “Quantifying energy losses in planar perovskite solar cells,” *Sol. Energy Mater. Sol. Cells*, vol. 174, pp. 206–213, Jan. 2018, doi: 10.1016/j.solmat.2017.09.002.

[49] M. H. Futscher and B. Ehrler, “Modeling the Performance Limitations and Prospects of Perovskite/Si Tandem Solar Cells under Realistic Operating Conditions,” *ACS Energy Lett.*, vol. 2, no. 9, pp. 2089–2095, Sep. 2017, doi: 10.1021/acsenergylett.7b00596.

[50] K. J. Albrecht, G. S. Jackson, and R. J. Braun, “Thermodynamically consistent modeling of redox-stable perovskite oxides for thermochemical energy conversion and storage,” *Appl. Energy*, vol. 165, pp. 285–296, Mar. 2016, doi: 10.1016/j.apenergy.2015.11.098.

[51] B. Liu *et al.*, “Optical Properties and Modeling of 2D Perovskite Solar Cells,” *Sol. RRL*, vol. 1, no. 8, p. 1700062, 2017, doi: 10.1002/solr.201700062.

[52] A. Raj *et al.*, “A computational approach to investigate the suitable ETL for lead-free CsGeI3 based perovskite solar cell,” *Mater. Today Proc.*, vol. 47, pp. 1564–1569, Jan. 2021, doi: 10.1016/j.matpr.2021.03.610.

[53] C. Tiwari, G. K. Gupta, and V. Mishra, “Computational analysis of lead free and highly efficient intrinsic Ch3NH3SnI3 based solar cell with suitable transport layers,” *Results Opt.*, vol. 13, p. 100517, Dec. 2023, doi: 10.1016/j.rio.2023.100517.

[54] U. Rani *et al.*, “Computational investigation of inverse perovskite SbPX3 (X = Mg, Ca, and Sr) structured materials with applicability in green energy resources,” *Comput. Condens. Matter*, vol. 36, p. e00835, Sep. 2023, doi: 10.1016/j.cocom.2023.e00835.

[55] “U.S. energy facts explained - consumption and production - U.S. Energy Information Administration (EIA).” Accessed: Sep. 09, 2020. [Online]. Available: https://www.eia.gov/energyexplained/us-energy-facts/

[56] J. G. Speight, *Handbook of Petroleum Product Analysis*. John Wiley & Sons, 2015.

[57] E. Wari, W. Zhu, and G. Lim, “Maintenance in the downstream petroleum industry: A review on methodology and implementation,” *Comput. Chem. Eng.*, vol. 172, p. 108177, Apr. 2023, doi: 10.1016/j.compchemeng.2023.108177.

[58] “Use of oil - U.S. Energy Information Administration (EIA).” Accessed: Aug. 26, 2023. [Online]. Available: https://www.eia.gov/energyexplained/oil-and-petroleum-products/use-of-oil.php

[59] “Lubricants market volume by country 2020,” Statista. Accessed: Aug. 26, 2023. [Online]. Available: https://www.statista.com/statistics/821076/lubricants-global-market-volume-by-country/

[60] C.-H. Kuo, *Tribology - Lubricants and Lubrication*. IntechOpen, 2011. doi: 10.5772/873.

[61] M. Torbacke, Å. K. Rudolphi, and E. Kassfeldt, *Lubricants: Introduction to Properties and Performance*. John Wiley & Sons, 2014.

[62] R. M. Mortier, M. F. Fox, and S. T. Orszulik, Eds., *Chemistry and Technology of Lubricants*. Dordrecht: Springer Netherlands, 2010. doi: 10.1007/978-1-4020-8662-5.

[63] A. J. Caines, R. F. Haycock, and J. E. Hillier, *Automotive Lubricants Reference Book*. John Wiley & Sons, 2004.

[64] A. Sequeira, *Lubricant Base Oil and Wax Processing*. CRC Press, 1994.

[65] B. E. Beasley, “Conventional Lube Basestock Manufacturing,” in *Practical Advances in Petroleum Processing*, C. S. Hsu and P. R. Robinson, Eds., New York, NY: Springer, 2006, pp. 449–526. doi: 10.1007/978-0-387-25789-1_15.

[66] S. Parkash, *Petroleum Fuels Manufacturing Handbook: including Specialty Products and Sustainable Manufacturing Techniques*, 1 edition. New York: McGraw-Hill Education, 2009.

[67] S. F. Brown, “Base Oil Groups: Manufacture, Properties and Performance,” presented at the Webinar, Tribology and Lubrication Technology, Apr. 2015. [Online]. Available: www.stle.org

[68] W. R. Herguth and T. M. Warne, *Turbine Lubrication in the 21st Century*. ASTM International, 2001.

[69] S. K. Lee, J. M. Rosenbaum, Y. Hao, and G.-D. Lei, “Premium Lubricant Base Stocks by Hydroprocessing,” in *Springer Handbook of Petroleum Technology*, C. S. Hsu and P. R. Robinson, Eds., in Springer Handbooks. , Cham: Springer International Publishing, 2017, pp. 1015–1042. doi: 10.1007/978-3-319-49347-3_34.

[70] L. R. Rudnick, Ed., *Lubricant Additives: Chemistry and Applications, Second Edition*, 2nd ed. Boca Raton: CRC Press, 2009. doi: 10.1201/9781420059656.

[71] E. V. Zaretsky, “Liquid lubrication in space,” *Tribol. Int.*, vol. 23, no. 2, pp. 75–93, Apr. 1990, doi: 10.1016/0301-679X(90)90041-M.

[72] A. Singh, N. Verma, T. G. Mamatha, A. Kumar, S. Singh, and K. Kumar, “Properties, functions and applications of commonly used lubricant additives: A review,” *Mater. Today Proc.*, vol. 44, pp. 5018–5022, Jan. 2021, doi: 10.1016/j.matpr.2021.01.029.

[73] I. Madanhire and C. Mbohwa, *Mitigating Environmental Impact of Petroleum Lubricants*. Cham: Springer International Publishing, 2016. doi: 10.1007/978-3-319-31358-0.

[74] V. Subramani, "Design of pipeline flush operations," presented at the 8th AIChE Southwest Process Technology Conference, 2016. doi: 2016.

[75] G. I. Taylor, "Diffusion by Continuous Movements," *Proc. Lond. Math. Soc.*, vol. s2-20, no. 1, pp. 196–212, 1922, doi: 10.1112/plms/s2-20.1.196.

[76] Taylor, G.I., "Dispersion of soluble matter in solvent flowing slowly through a tube," *Proc. R. Soc. Lond. Ser. Math. Phys. Sci.*, vol. 219, no. 1137, pp. 186–203, Aug. 1953, doi: 10.1098/rspa.1953.0139.

[77] G. I. Taylor, "Dispersion of soluble matter in solvent flowing slowly through a tube," *Proc. R. Soc. Lond. Ser. Math. Phys. Sci.*, vol. 219, no. 1137, pp. 186–203, Aug. 1954, doi: 10.1098/rspa.1953.0139.

[78] A. Ramanujan, "Deterministic models to explain the phenomenon of interfacial mixing in refined products pipelines," p. 177, 2008.

[79] G. He, M. Lin, B. Wang, Y. Liang, and Q. Huang, "Experimental and numerical research on the axial and radial concentration distribution feature of miscible fluid interfacial mixing process in products pipeline for industrial applications," *Int. J. Heat Mass Transf.*, vol. 127, pp. 728–745, Dec. 2018, doi: 10.1016/j.ijheatmasstransfer.2018.08.080.

[80] A. R. Patrachari and A. H. Johannes, "A conceptual framework to model interfacial contamination in multiproduct petroleum pipelines," *Int. J. Heat Mass Transf.*, vol. 55, no. 17, pp. 4613–4620, Aug. 2012, doi: 10.1016/j.ijheatmasstransfer.2012.04.017.

[81] S. Blažič, G. Geiger, and D. Matko, "Application of a heterogenous multiscale method to multi-batch driven pipeline," *Appl. Math. Model.*, vol. 38, no. 3, pp. 864–877, Feb. 2014, doi: 10.1016/j.apm.2013.07.001.

[82] "www.nrel.gov." Accessed: Nov. 14, 2019. [Online]. Available: https://www.nrel.gov/pv/cell-efficiency.html

[83] T. Sato, S. Takagi, S. Deledda, B. C. Hauback, and S. Orimo, "Extending the applicability of the Goldschmidt tolerance factor to arbitrary ionic compounds," *Sci. Rep.*, vol. 6, p. 23592, Apr. 2016, doi: 10.1038/srep23592.

[84] M. A. Green, A. Ho-Baillie, and H. J. Snaith, "The emergence of perovskite solar cells," *Nat. Photonics*, vol. 8, no. 7, pp. 506–514, Jul. 2014, doi: 10.1038/nphoton.2014.134.

[85] C. Li, X. Lu, W. Ding, L. Feng, Y. Gao, and Z. Guo, "Formability of ABX3 (X = F, Cl, Br, I) halide perovskites," *Acta Crystallogr. B*, vol. 64, no. 6, pp. 702–707, Dec. 2008, doi: 10.1107/S0108768108032734.

[86] T. T. Ava, A. Al Mamun, S. Marsillac, and G. Namkoong, "A Review: Thermal Stability of Methylammonium Lead Halide Based Perovskite Solar Cells," *Appl. Sci.*, vol. 9, no. 1, Art. no. 1, Jan. 2019, doi: 10.3390/app9010188.

[87] G. Kieslich, S. Sun, and A. K. Cheetham, "An extended Tolerance Factor approach for organic–inorganic perovskites," *Chem. Sci.*, vol. 6, no. 6, pp. 3430–3433, 2015, doi: 10.1039/C5SC00961H.

[88] G. Kieslich, S. Sun, and A. K. Cheetham, "Solid-state principles applied to organic–inorganic perovskites: new tricks for an old dog," *Chem. Sci.*, vol. 5, no. 12, pp. 4712–4715, 2014, doi: 10.1039/C4SC02211D.

[89] M. Cai, Y. Wu, H. Chen, X. Yang, Y. Qiang, and L. Han, "Cost-Performance Analysis of Perovskite Solar Modules," *Adv. Sci.*, vol. 4, no. 1, p. 1600269, Jan. 2017, doi: 10.1002/advs.201600269.

[90] N. L. Chang, A. W. Yi Ho-Baillie, P. A. Basore, T. L. Young, R. Evans, and R. J. Egan, "A manufacturing cost estimation method with uncertainty analysis and its application to perovskite on glass photovoltaic modules: A manufacturing cost estimation method," *Prog. Photovolt. Res. Appl.*, vol. 25, no. 5, pp. 390–405, May 2017, doi: 10.1002/pip.2871.

[91] Z. Song *et al.*, "A technoeconomic analysis of perovskite solar module manufacturing with low-cost materials and techniques," *Energy Environ. Sci.*, vol. 10, no. 6, pp. 1297–1305, Jun. 2017, doi: 10.1039/C7EE00757D.

[92] Z. Li *et al.*, "Cost Analysis of Perovskite Tandem Photovoltaics," *Joule*, vol. 2, no. 8, pp. 1559–1572, Aug. 2018, doi: 10.1016/j.joule.2018.05.001.

[93] G. Hiltscher, W. Mühlthaler, and J. Smits, *Industrial Pigging Technology: Fundamentals, Components, Applications*. John Wiley & Sons, 2006.

[94] "Pipeline Cleaning Pigs - Pipeline Pig Manufacturers," Inline Services. Accessed: Sep. 11, 2019. [Online]. Available: https://www.inlineservices.com/product-category/pipeline-pigs/

[95] M. Stewart, "Pipeline pigging," in *Surface Production Operations*, Elsevier, 2016, pp. 897–960. doi: 10.1016/B978-1-85617-808-2.00013-4.

[96] J. Quarini and S. Shire, "A Review of Fluid-Driven Pipeline Pigs and their Applications," *Proc. Inst. Mech. Eng. Part E J. Process Mech. Eng.*, vol. 221, no. 1, pp. 1–10, Feb. 2007, doi: 10.1243/0954408JPME108.

[97] K. S. Sutherland and G. Chase, *Filters and Filtration Handbook*. Elsevier, 2011.

[98] “LUBE OIL BLENDING PLANT | LINUS PROJECTS,” lubricant. Accessed: Sep. 15, 2023. [Online]. Available: https://www.linusprojects.com/copy-of-lube-oil-blending-plant

[99] J. Bai, X. Jin, and J.-T. Wu, “Multifunctional anti-wax coatings for paraffin control in oil pipelines,” *Pet. Sci.*, vol. 16, no. 3, pp. 619–631, Jun. 2019, doi: 10.1007/s12182-019-0309-7.

[100] Nakatsuka and Matthew A, “In-Situ Applied Omniphobic Coatings for Water Pipeline Repair and Retrofitting,” 2018. Accessed: Jan. 07, 2020. [Online]. Available: https://cfpub.epa.gov/ncer_abstracts/index.cfm/fuseaction/display.abstractDetail/abstract/10824/report/F

[101] R. V. Lakshmi, T. Bharathidasan, P. Bera, and B. J. Basu, “Fabrication of superhydrophobic and oleophobic sol–gel nanocomposite coating,” *Surf. Coat. Technol.*, vol. 206, no. 19, pp. 3888–3894, May 2012, doi: 10.1016/j.surfcoat.2012.03.044.

[102] Y. Li, T. Hu, B. Li, J. Wei, and J. Zhang, “Totally Waterborne and Highly Durable Superamphiphobic Coatings for Anti-Icing and Anticorrosion,” *Adv. Mater. Interfaces*, vol. 6, no. 23, p. 1901255, 2019, doi: 10.1002/admi.201901255.

[103] S. H. Robinson, “Vehicle mounted apparatus for high-pressure fluid blasting,” US9127419B2, Sep. 08, 2015 Accessed: Apr. 23, 2020. [Online]. Available: https://patents.google.com/patent/US9127419B2/en

[104] B. Avvaru, N. Venkateswaran, P. Uppara, S. B. Iyengar, and S. S. Katti, “Current knowledge and potential applications of cavitation technologies for the petroleum industry,” *Ultrason. Sonochem.*, vol. 42, pp. 493–507, Apr. 2018, doi: 10.1016/j.ultsonch.2017.12.010.

[105] Z. Qu *et al.*, “Methodology for removing fouling within liquid-filled pipelines based on ultrasonic guided waves cavitation effect,” *Appl. Acoust.*, vol. 157, p. 107018, Jan. 2020, doi: 10.1016/j.apacoust.2019.107018.

[106] T. Bakker and V. Ivannikov, *Cavitation for Effective Well Cleaning*. 2002. doi: 10.2523/75352-MS.

[107] “Tee-Type Filters | Particulate Filters | Filters | All Products | Swagelok.” Accessed: Sep. 15, 2023. [Online]. Available: https://products.swagelok.com/en/all-products/filters/particulate-filters/tee-type-filters/p/filter-0004

[108] “Stainless Steel In-Line Particulate Filter, 1/8 in. Swagelok Tube Fitting, 2 Micron Pore Size | Particulate Filters | Filters | All Products | Swagelok.” Accessed: Sep. 15, 2023. [Online]. Available: https://products.swagelok.com/en/c/inline-filters/p/SS-2F-2

[109] D02 Committee, “Test Method for Kinematic Viscosity of Transparent and Opaque Liquids (and Calculation of Dynamic Viscosity),” ASTM International. doi: 10.1520/D0445-12.

[110] D. R. Brouwer and J.-D. Jansen, “Dynamic Optimization of Waterflooding With Smart Wells Using Optimal Control Theory,” *SPE J.*, vol. 9, no. 04, pp. 391–402, Dec. 2004, doi: 10.2118/78278-PA.

[111] C. Völcker, J. B. Jørgensen, and E. H. Stenby, “Oil reservoir production optimization using optimal control,” in *2011 50th IEEE Conference on Decision and Control and European Control Conference*, Dec. 2011, pp. 7937–7943. doi: 10.1109/CDC.2011.6161271.

[112] S. S. Vembadi, R. G. Patel, J. J. Trivedi, and V. Prasad, “Real-time feedback control of SAGD wells using model predictive control to optimize steam chamber development under uncertainty,” *Can. J. Chem. Eng.*, vol. 96, no. 6, pp. 1290–1305, 2018, doi: 10.1002/cjce.23096.

[113] F. B. Morari Alberto Bemporad,Manfred, *Predictive Control for Linear and Hybrid Systems : Francesco Borrelli,Alberto Bemporad,Manfred Morari*. Accessed: Sep. 14, 2023. [Online]. Available: https://www.book2look.com/book/KL2k5IHDOe

[114] D. E. Kirk, *Optimal Control Theory: An Introduction*, Illustrated edition. Mineola, N.Y: Dover Publications, 2004.

[115] R. F. Stengel, *Optimal Control and Estimation*, Revised ed. edition. New York: Dover Publications, 1994.

[116] G. M. Bakan and V. M. Kuntsevich, “Synthesis of an optimal control system for a primary oil refining process,” *Automatica*, vol. 9, no. 2, pp. 233–242, Mar. 1973, doi: 10.1016/0005-1098(73)90077-0.

[117] X. Wang, Y. Ding, D. Li, and Y. He, “Optimal Control Method of Oil Well Production Based on Cropped Well Group Samples and Machine Learning,” *Energies*, vol. 16, no. 12, Art. no. 12, Jan. 2023, doi: 10.3390/en16124735.

[118] J. P. Maree and L. Imsland, “Optimal control strategies for oil production under gas coning conditions,” in *2014 IEEE Conference on Control Applications (CCA)*, Oct. 2014, pp. 572–578. doi: 10.1109/CCA.2014.6981401.

[119] F. L. V. Vianna, H. R. B. Orlande, and G. S. Dulikravich, “Pipeline Heating Method Based on Optimal Control and State Estimation,” *Heat Transf. Eng.*, vol. 34, no. 5–6, pp. 511–519, Jan. 2013, doi: 10.1080/01457632.2012.723536.

[120] K. M. Yenkie and U. Diwekar, “Stochastic Optimal Control of Seeded Batch Crystallizer Applying the Ito Process,” *Ind. Eng. Chem. Res.*, p. 120604103933002, Jun. 2012, doi: 10.1021/ie300491v.

[121] F. D. Fagundez, J. L. D. Facó, and A. E. Xavier, “A Nonlinear Optimal Control Approach to Process Scheduling,” in *Optimization and Optimal Control: Theory and Applications*, A. Chinchuluun, P. M. Pardalos, R. Enkhbat, and I. Tseveendorj, Eds., in Springer Optimization and Its Applications. , New York, NY: Springer, 2010, pp. 409–421. doi: 10.1007/978-0-387-89496-6_19.

[122] R. Vinter, *Optimal Control*. Boston: Birkhäuser Boston, 2010. doi: 10.1007/978-0-8176-8086-2.

[123] K. M. Yenkie and U. Diwekar, “Stochastic Optimal Control of Seeded Batch Crystallizer Applying the Ito Process,” *Ind. Eng. Chem. Res.*, p. 120604103933002, Jun. 2012, doi: 10.1021/ie300491v.

[124] P. T. Benavides and U. Diwekar, “Studying various optimal control problems in biodiesel production in a batch reactor under uncertainty,” *Fuel*, vol. 103, pp. 585–592, Jan. 2013, doi: 10.1016/j.fuel.2012.06.089.

[125] U. Diwekar, *Introduction to Applied Optimization*. Springer, 2008.

[126] M. R. Riazi, *Characterization and properties of petroleum fractions*. W. Conshohocken, PA: ASTM International, 2005.

[127] M. Roegiers and B. Zhmud, “Property blending relationships for binary mixtures of mineral oil and elektrionised vegetable oil: viscosity, solvent power, and seal compatibility index,” *Lubr. Sci.*, vol. 23, no. 6, pp. 263–278, 2011, doi: https://doi.org/10.1002/ls.154.

[128] M. Wang *et al.*, “Summary of Expansions and Updates in GREET® 2021,” Argonne National Lab.(ANL), Argonne, IL (United States), 2021.

[129] G. J. Ruiz-Mercado, M. A. Gonzalez, and R. L. Smith, “Expanding GREENSCOPE beyond the gate: a green chemistry and life cycle perspective,” *Clean Technol. Environ. Policy*, vol. 16, no. 4, pp. 703–717, Apr. 2014, doi: 10.1007/s10098-012-0533-y.

[130] K. Shahzad, R. Kollmann, S. Maier, and M. Narodoslawsky, “SPIonWEB – Ecological Process Evaluation with the Sustainable Process Index (SPI),” in *Computer Aided Chemical Engineering*, vol. 33, J. J. Klemeš, P. S. Varbanov, and P. Y. Liew, Eds., in 24 European Symposium on Computer Aided Process Engineering, vol. 33. , Elsevier, 2014, pp. 487–492. doi: 10.1016/B978-0-444-63456-6.50082-X.

[131] I. T. Herrmann and A. Moltesen, “Does it matter which Life Cycle Assessment (LCA) tool you choose? – a comparative assessment of SimaPro and GaBi,” *J. Clean. Prod.*, vol. 86, pp. 163–169, Jan. 2015, doi: 10.1016/j.jclepro.2014.08.004.

[132] S. Shalev-Shwartz and S. Ben-David, *Understanding Machine Learning: From Theory to Algorithms*. Cambridge University Press, 2014.

[133] C. M. Bishop, *Pattern Recognition and Machine Learning*. Springer, 2006.

[134] K. P. Murphy, *Machine Learning: A Probabilistic Perspective*. MIT Press, 2012.

[135] T. Hastie, R. Tibshirani, and J. Friedman, *The Elements of Statistical Learning: Data Mining, Inference, and Prediction*. Springer Science & Business Media, 2013.

[136] D. C. Montgomery, E. A. Peck, and G. G. Vining, *Introduction to Linear Regression Analysis*. John Wiley & Sons, 2021.

[137] W.-Y. Loh, "Classification and regression trees," *WIREs Data Min. Knowl. Discov.*, vol. 1, no. 1, pp. 14–23, 2011, doi: 10.1002/widm.8.

[138] F. Esposito, D. Malerba, G. Semeraro, and J. Kay, "A comparative analysis of methods for pruning decision trees," *IEEE Trans. Pattern Anal. Mach. Intell.*, vol. 19, no. 5, pp. 476–491, May 1997, doi: 10.1109/34.589207.

[139] L. Breiman, "Random Forests," *Mach. Learn.*, vol. 45, no. 1, pp. 5–32, Oct. 2001, doi: 10.1023/A:1010933404324.

[140] S. Abe, *Support Vector Machines for Pattern Classification*. in Advances in Pattern Recognition. London: Springer, 2010. doi: 10.1007/978-1-84996-098-4.

[141] C. C. Aggarwal, *Neural Networks and Deep Learning: A Textbook*. Cham: Springer International Publishing, 2018. doi: 10.1007/978-3-319-94463-0.

[142] A. A. Patel, *Hands-On Unsupervised Learning Using Python: How to Build Applied Machine Learning Solutions from Unlabeled Data*. O'Reilly Media, Inc., 2019.

[143] I. Vasilev, D. Slater, G. Spacagna, P. Roelants, and V. Zocca, *Python Deep Learning: Exploring deep learning techniques and neural network architectures with PyTorch, Keras, and TensorFlow, 2nd Edition*. Packt Publishing Ltd, 2019.

[144] B. S. Everitt, S. Landau, M. Leese, and D. Stahl, *Cluster Analysis*. John Wiley & Sons, 2011.

[145] V. Cherkassky and F. M. Mulier, *Learning from Data: Concepts, Theory, and Methods*. John Wiley & Sons, 2007.

[146] R. S. Sutton and A. G. Barto, *Reinforcement Learning, second edition: An Introduction*. MIT Press, 2018.

[147] C. Szepesvári, *Algorithms for Reinforcement Learning*. Springer Nature, 2022.

[148] M. A. Wiering and H. van Hasselt, "Ensemble Algorithms in Reinforcement Learning," *IEEE Trans. Syst. Man Cybern. Part B Cybern.*, vol. 38, no. 4, pp. 930–936, Aug. 2008, doi: 10.1109/TSMCB.2008.920231.

[149] D. E. Moriarty, A. C. Schultz, and J. J. Grefenstette, “Evolutionary Algorithms for Reinforcement Learning,” *J. Artif. Intell. Res.*, vol. 11, pp. 241–276, Sep. 1999, doi: 10.1613/jair.613.

[150] Y. Sun, X. Wang, N. Ren, Y. Liu, and S. You, “Improved Machine Learning Models by Data Processing for Predicting Life-Cycle Environmental Impacts of Chemicals,” *Environ. Sci. Technol.*, vol. 57, no. 8, pp. 3434–3444, Feb. 2023, doi: 10.1021/acs.est.2c04945.

[151] R. Bro and A. K. Smilde, “Principal component analysis,” *Anal. Methods*, vol. 6, no. 9, pp. 2812–2831, 2014, doi: 10.1039/C3AY41907J.

[152] B. Schölkopf, A. Smola, and K.-R. Müller, “Kernel principal component analysis,” in *Artificial Neural Networks — ICANN’97*, vol. 1327, W. Gerstner, A. Germond, M. Hasler, and J.-D. Nicoud, Eds., in Lecture Notes in Computer Science, vol. 1327, Berlin, Heidelberg: Springer Berlin Heidelberg, 1997, pp. 583–588. doi: 10.1007/BFb0020217.

[153] S. Suthaharan, *Machine Learning Models and Algorithms for Big Data Classification: Thinking with Examples for Effective Learning*. Springer, 2015.

[154] S. Raschka, *Python Machine Learning*. Packt Publishing Ltd, 2015.

[155] C. Molnar, *Interpretable Machine Learning*. Lulu.com, 2020.

[156] J. Brownlee, *Machine Learning Algorithms From Scratch with Python*. Machine Learning Mastery, 2016.

[157] C. C. Aggarwal, *Data Classification: Algorithms and Applications*. CRC Press, 2014.

Appendix A

Supporting Materials for Procedural Enhancements

The following graphs illustrate the analysis of the enhanced operational procedure implemented at the collaborative facility.

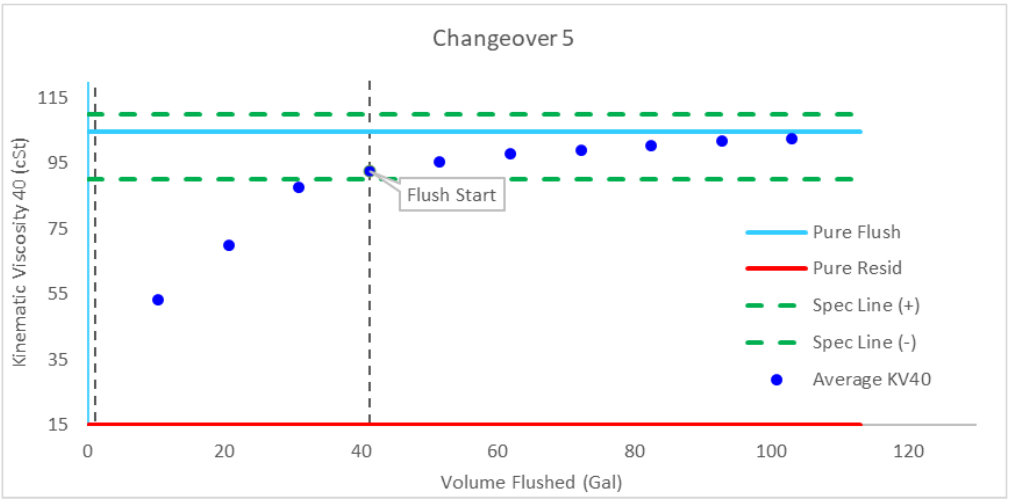

Figure A1. Analysis of Implemented Procedural Enhancement for Changeover 5

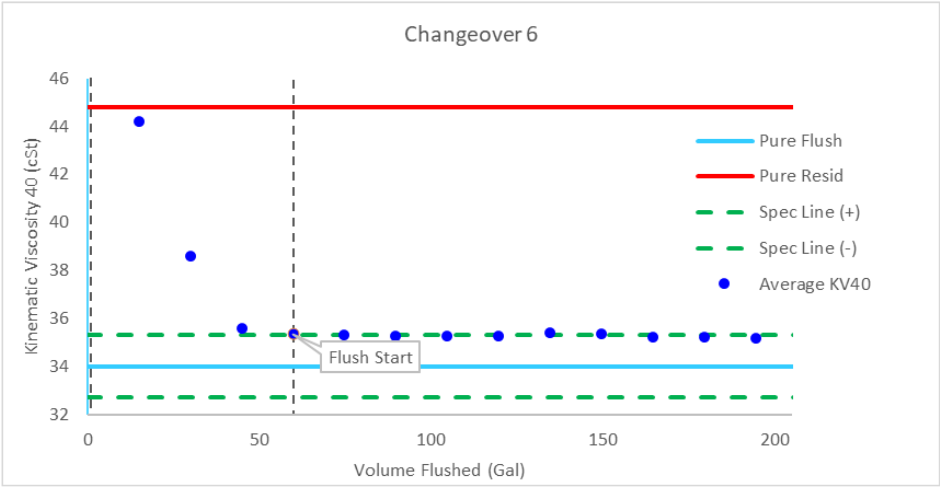

Figure A2. Analysis of Implemented Procedural Enhancement for Changeover 6

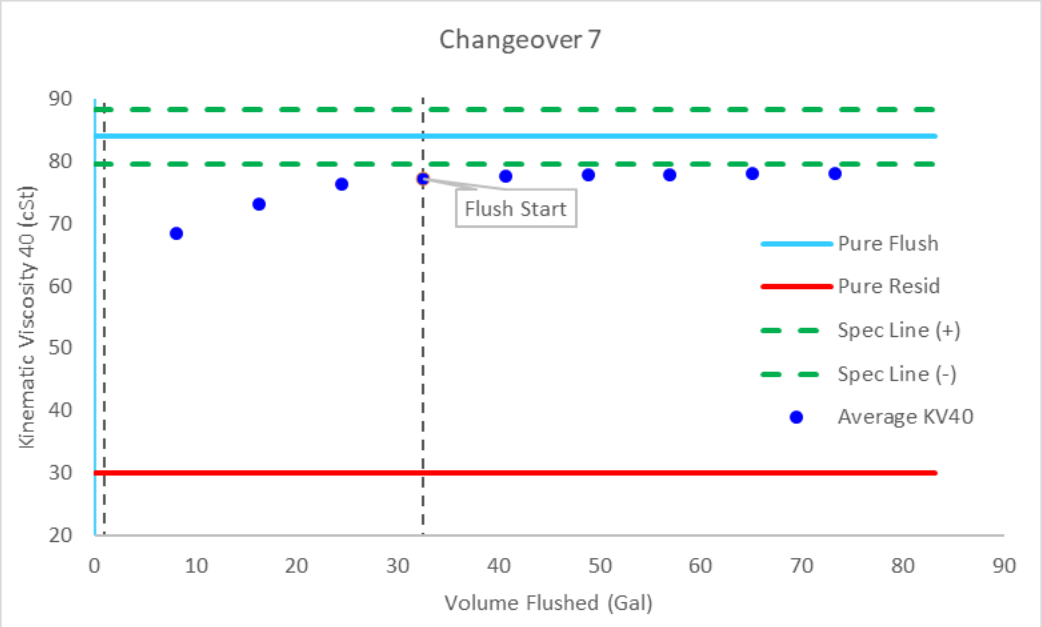

Figure A3. Analysis of Implemented Procedural Enhancement for Changeover 7

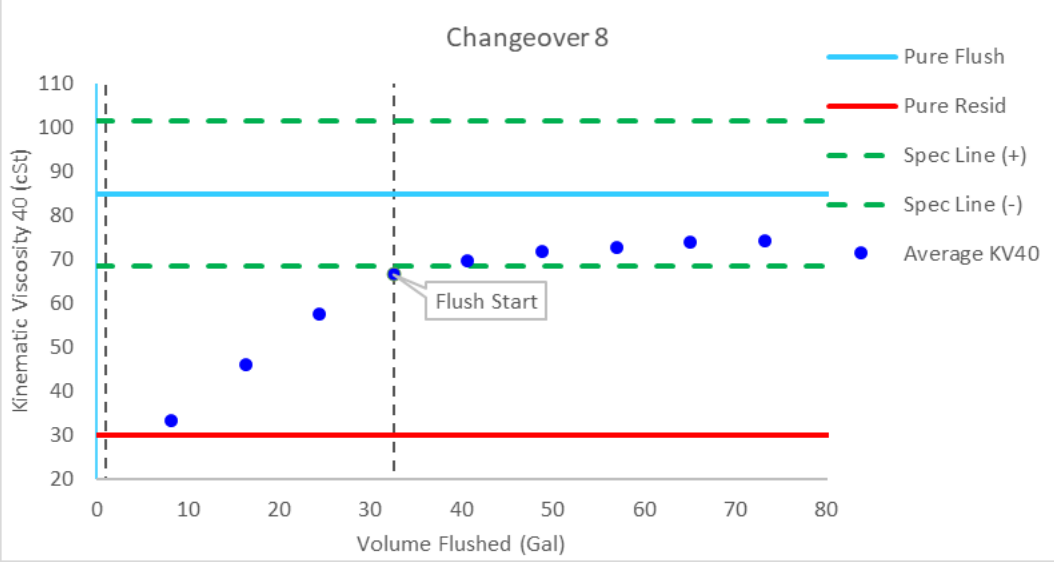

Figure A4. Analysis of Implemented Procedural Enhancement for Changeover 8

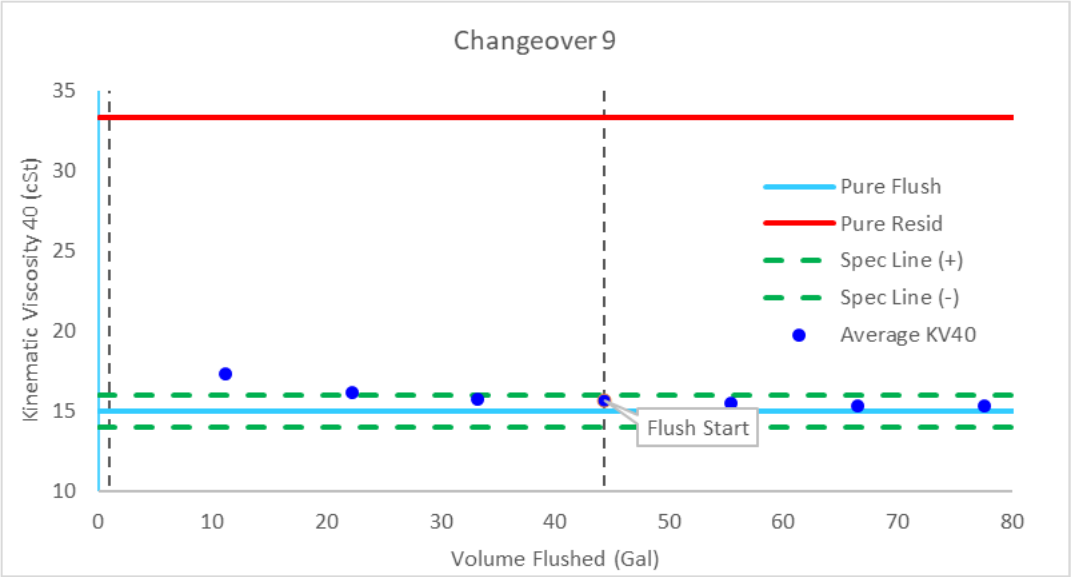

Figure A5. Analysis of Implemented Procedural Enhancement for Changeover 9

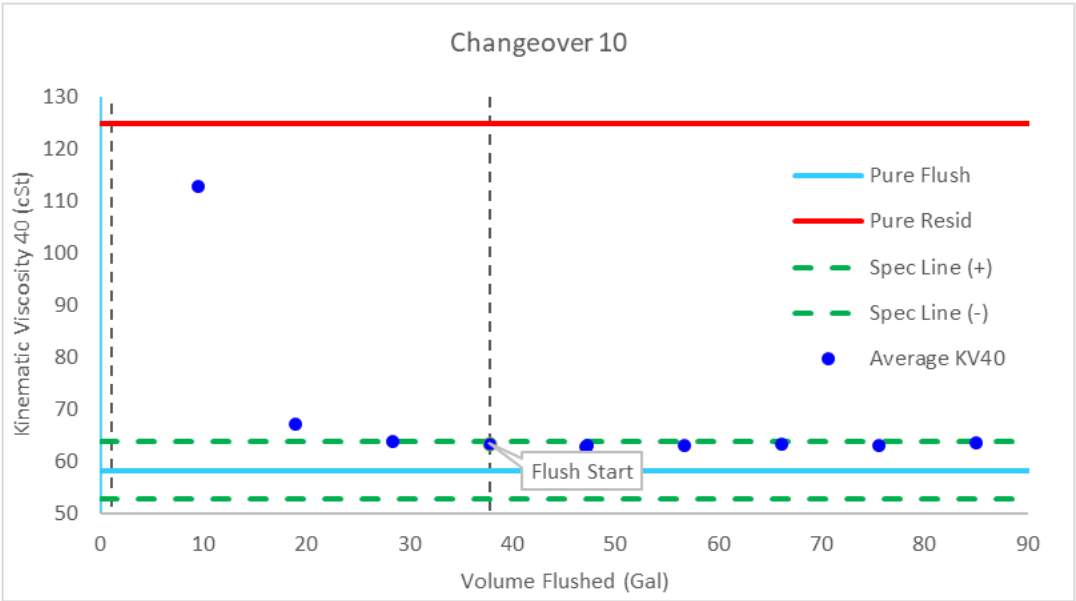

Figure A6. Analysis of Implemented Procedural Enhancement for Changeover 10

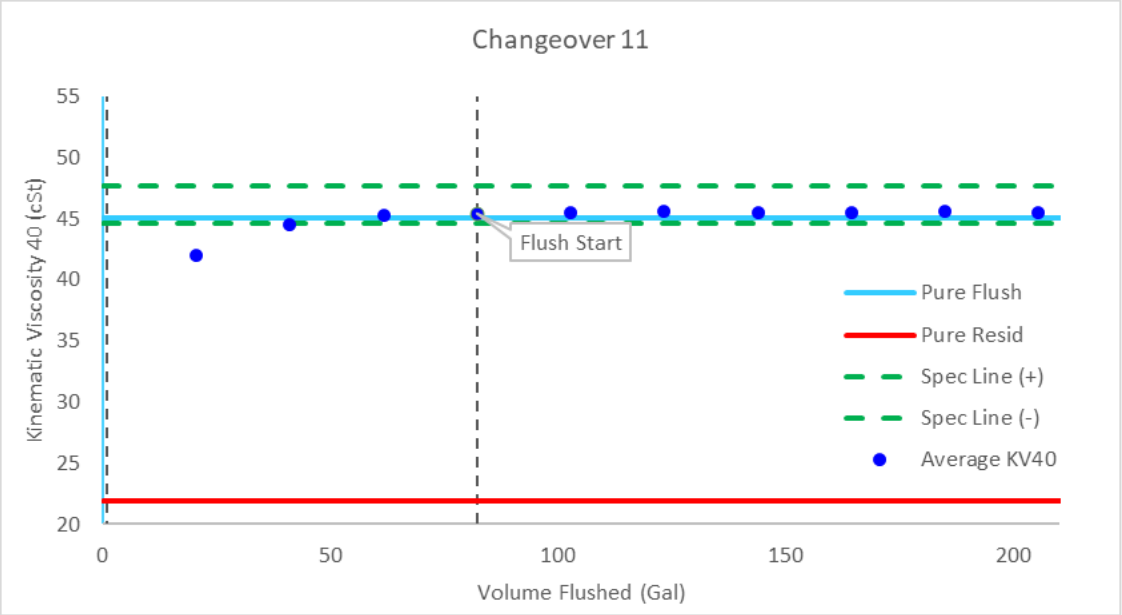

Figure A7. Analysis of Implemented Procedural Enhancement for Changeover 11

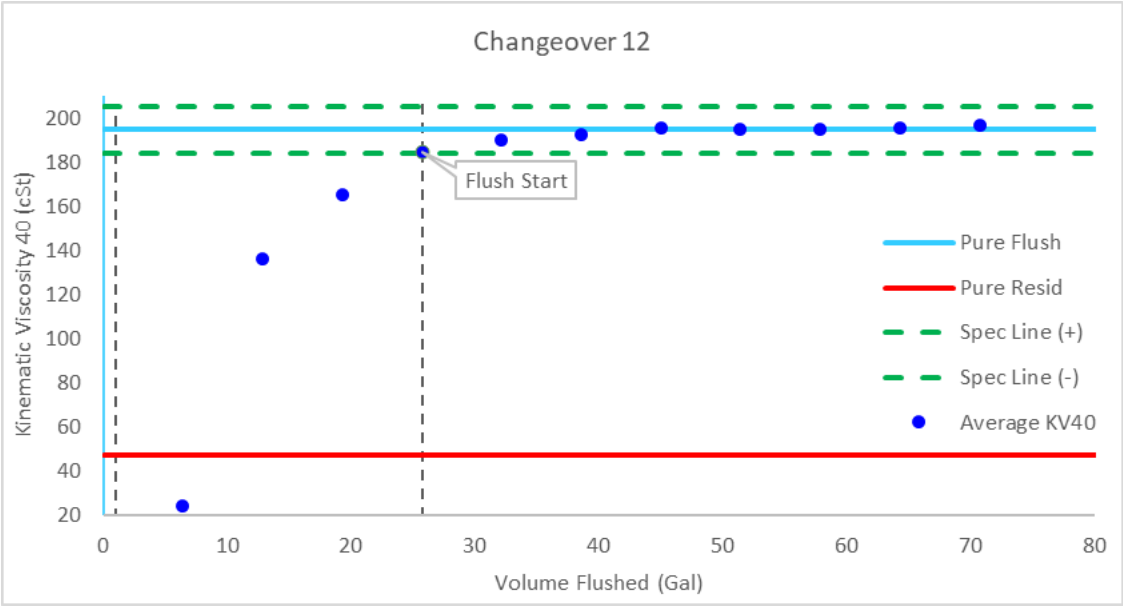

Figure A8. Analysis of Implemented Procedural Enhancement for Changeover 12

Appendix B

ASTM D445 Guidelines for Kinematic Viscosity Testing

Kinematic viscosity is the ratio between momentum transport and momentum storage. Such ratios are called diffusivities with dimensions of length squared divided by time and the SI unit is metre squared divided by second (m^2/s). Among the transport properties for heat, mass, and momentum transfer, kinematic viscosity is the momentum diffusivity. Formerly, kinematic viscosity was defined specifically for viscometers covered by this test method as the resistance to flow under gravity. More generally, it is the ratio between momentum transport and momentum storage. For gravity-driven flow under a given hydrostatic head, the pressure head of a liquid is proportional to its density, ρ, if the density of air is negligible compared to that of the liquid. For any particular viscometer covered by this test method, the time of flow of a fixed volume of liquid is directly proportional to its kinematic viscosity, ν, where $\nu = \eta / \rho$, and η is the dynamic viscosity.

1. Summary of Test Method

The time is measured for a fixed volume of liquid to flow under gravity through the capillary of a calibrated viscometer under a reproducible driving head and at a closely controlled and known temperature. The kinematic viscosity (determined value) is the product of the measured flow time and the calibration constant of the viscometer. Two such determinations are needed from which to calculate a kinematic viscosity result that is the average of two acceptable determined values.

2. Apparatus

Viscometers - Use only calibrated viscometers of the glass capillary type, capable of being used to determine kinematic viscosity within the limits of the precision given in the precision section.

Viscometer Holders - Use viscometer holders to enable all viscometers which have the upper meniscus directly above the lower meniscus to be suspended vertically within 1° in all directions. Those viscometers whose upper meniscus is offset from directly above the lower meniscus shall be suspended vertically within 0.3° in all directions (see Specifications ASTM D446 and ISO 3105). Viscometers shall be mounted in the constant temperature bath in the same manner as when calibrated and stated on the certificate of calibration.

Temperature-Controlled Bath - Use a transparent liquid bath of sufficient depth such, that at no time during the measurement of flow time, any portion of the sample in the viscometer is less than 20 mm below the surface of the bath liquid or less than 20 mm above the bottom of the bath.

Temperature Control - For each series of flow time measurements, the temperature control of the bath liquid shall be such that within the range from 15 °C to 100 °C, the temperature of the bath medium does not vary by more than 60.02 °C of the selected temperature over the length of the viscometer, or between the position of each viscometer, or at the location of the thermometer. For temperatures outside this range, the deviation from the desired temperature must not exceed ± 0.05 °C.

Cleaning Solution – a completely miscibile volatile solvent such as Heptane is suitable.

3. General Procedure for Kinematic Viscosity Measurement

- Adjust and maintain the viscometer bath at the required test temperature
- Thermometers shall be held in an upright position under the same conditions of immersion as when calibrated
- In order to obtain the most reliable temperature measurement, it is recommended that two thermometers with valid calibration certificates be used
- They should be viewed with a lens assembly giving approximately five times magnification and be arranged to eliminate parallax errors
- Select a clean, dry, calibrated viscometer having a range covering the estimated kinematic viscosity (that is, a wide capillary for a very viscous liquid and a narrower capillary for a more fluid liquid). The flow time for manual viscometers shall not be less than 200 s or the longer time noted in Specifications D446
- When the test temperature is below the dew point, fill the viscometer in the normal manner as required. It is recommended to charge the viscometer outside the bath.
- To ensure that moisture does not condense or freeze on the walls of the capillary, draw the test portion into the working capillary and timing bulb, place rubber stoppers into the tubes to hold the test portion in place, and insert the viscometer into the bath
- After insertion, allow the viscometer to reach bath temperature, and then remove the stoppers. When performing manual viscosity determinations, do not use those viscometers which cannot be removed from the constant temperature bath for charging the sample portion.

Appendix C

Supporting Materials for Optimal Control Studies

The Pontryagin's maximum principle solution approach involves the use of the adjoint equations and the Hamiltonian equations illustrated below:

Adjoint equations corresponding to the state equations

$$\frac{dz_i}{dt} = -\sum_{j=1}^{n} z_j \frac{\partial f_j}{\partial x_i} \tag{C.1}$$

$$\frac{dz_1}{dt} = z_1 \frac{Q_t}{A_C L} - z_2 \frac{Q_t}{A_C L} - z_3 \left[\left(9{x_{A_t}}^2 \mu_A^{\frac{2}{3}} \frac{Q_t}{A_C L} \left(\mu_B^{\frac{1}{3}} - \mu_A^{\frac{1}{3}} \right) \right) + \left(12x_{A_t} - 18{x_1}^2 \right) \frac{Q_t}{A_C L} \left(\mu_A^{\frac{1}{3}} \mu_B^{\frac{2}{3}} - \mu_A^{\frac{2}{3}} \mu_B^{\frac{1}{3}} \right) + \left(3{x_{A_t}}^2 - 4x_{A_t} + 1 \right) \frac{3Q}{A_C L} \left(\mu_B - \mu_A^{\frac{1}{3}} \mu_B^{\frac{2}{3}} \right) \right] \tag{C.2}$$

$$\frac{dz_2}{dt} = -z_1 \frac{Q_t}{A_C L} + z_2 \frac{Q_t}{A_C L} - z_3 \left[\left([3\mu_A^{\frac{2}{3}} \left(-3{x_{B_t}}^2 + 6x_{B_t} - 3 \right) \frac{Q_t}{A_C L} \left(\mu_B^{\frac{1}{3}} - \mu_A^{\frac{1}{3}} \right) + 6(1 - 4x_{B_t} + 3\,{x_{B_t}}^2) \frac{Q_t}{A_C L} \left(\mu_A^{\frac{1}{3}} \mu_B^{\frac{2}{3}} - \mu_A^{\frac{2}{3}} \mu_B^{\frac{1}{3}} \right) + 3\mu_B^{\frac{2}{3}} (2x_{B_t} - 3{x_{B_t}}^2) \frac{Q_t}{A_C L} \left(\mu_B^{\frac{1}{3}} - \mu_A^{\frac{1}{3}} \right)] \right) \right] \tag{C.3}$$

The maximum principle involves the maximization of Hamiltonian over the control variable, the optimality condition is [|dH/dQ_t |] < tolerance. The Hamiltonian is a function of several variables such as x, t, z, and Q_t, hence, its derivative can be expressed as a sum of partial derivatives, with respect to each of these variables t, x, y. The complete derivative with respect to one variable (t), is given by equation (C.1)

$$\frac{dH}{dQ_t} = \sum_{i=1}^{3}\left(\frac{dH}{dx_i}\right)\left(\frac{dx_i}{dQ_t}\right) + \sum_{i=1}^{3}\left(\frac{dH}{dz_i}\right)\left(\frac{dz_i}{dQ_t}\right) \quad \text{(C.4)}$$

$$where: \theta_i = \frac{dx_i}{dQ} \;\&\; \Phi_i = \frac{dz_i}{dQ_t} \quad \text{(C.5)}$$

The following differential equations are to evaluate θ_i and Φ_i

$$\frac{d\left(\frac{dx_i}{dt}\right)}{dQ_t} = \frac{d\left(\frac{dx_i}{dQ_t}\right)}{dt} = \frac{d\theta_i}{dt} \quad \text{(C.6)}$$

$$\frac{d\left(\frac{dz_i}{dt}\right)}{dQ_t} = \frac{d\left(\frac{dz_i}{dQ_t}\right)}{dt} = \frac{d\Phi_i}{dt} \quad \text{(C.7)}$$

Thus, the general form of these two equations, in terms of the associated variables, can be written as

$$\frac{d\theta_i}{dt} = \text{f}\,(x_i, Q_t, t) \quad \text{(C.8)}$$

$$\frac{d\Phi_i}{dt} = \text{f}\,(x_i, z_i, Q_t, t) \quad \text{(C.9)}$$

For example, if we consider the first state equation for state variable x_A

$$\frac{d\theta_1}{dt} = \frac{-x_A}{A_C L} \quad \text{(C.10)}$$

$$\frac{d\Phi_1}{dt} = \frac{-z_1 x_A}{A_C L} \quad \text{(C.11)}$$

Equation (C.8) is integrated in the forward direction, using a numerical method with the initial conditions of $\theta_i(t_0)$ = [0,0,0], while equation (C.9) is integrated in the backward direction, with the final boundary conditions of $\Phi_i(t_f)$ = [0,0,0,0]

The computational codes for the work can be accessed through the following Github link: https://github.com/kmygroup/PhD-Contributions_SSJ.git

Appendix D

Educational Contributions

1. American Society for Engineering Education (ASEE) Annual Conference 2022

Hands-on Experience in Solving Real-World Problems via a Unique Student-Faculty-Industry Collaboration Program

1. Introduction

Modern engineering education should have an inclusive teaching curriculum that combines traditional lecture-based learning with new methods that can bridge the gap between what students learn and what they need in their future workplace. To meet the demands of ever-evolving technological advancements and emerge as outstanding future engineers, changes in the way we educate students are required. As per a World Economic Forum report (Gray 2016), the top 5 skills essential to being a great engineer for the job market of Industry 4.0 includes Complex Problem Solving, Critical Thinking, Creativity, People Management, and Coordinating with others. To address these educational needs, we introduce our unique student-faculty-industry collaboration program, a hallmark that makes our curriculum exclusive. The program is a problem-based learning approach that uses complex real-world problems as a driving force to promote student learning of concepts and fundamental principles (Warnock et al. Aragh 2016; Guo et al. 2020; Chen et al. 2019). Incorporating a problem-based learning approach in the curriculum helps students to understand that the concepts they are learning are useful beyond the class and the university (Ocon 2012; Beier et al. 2019). The program increases student engagement and curiosity by empowering self-initiated learning. The students are encouraged to take an interest in the specific field by reviewing ongoing practices and operations, they are taught to identify the problem or limitations in these processes, and they develop the curiosity that motivates them to actively seek ways to solve the problem. By connecting them to a bigger picture, we set the students up for success at university and beyond.

2. Formulation of the Project

The Chemical Engineering department at our university has been actively involved in research and partnerships with diverse industries, federal/state agencies, and foundations. Our collaborations with Nestle, Campbells, Domino Sugar, Pfizer, AstraZeneca, ExxonMobil,

This research was used to enhance the engineering learning experience through the "Engineering Clinic Program – A Hallmark of Rowan University". The program is a problem-based learning approach that uses complex real-world problems as a driving force to promote student learning of concepts and fundamental principles and provide a graduate level research experience to the undergraduate students. The learning outcomes for the students are: An ability to demonstrate skills relevant to research and engineering, Ability to identify, formulate, and solve multidisciplinary chemical engineering problems, Proficiency in conducting standard tests and measurements, designing and conducting systematic experiments, developing a pilot plant, and collecting and interpreting the

experimental data to improve the processes, An ability to perform data analysis to extract meaningful insights, An ability to apply technical writing, presentation, and effective communication skills in a broadly defined technical and non-technical audience, An ability to apply modern tools of engineering, science, and technology to solve broad categories of Chemical Engineering problems, Proficiency to work as an excellent team member as well as an excellent leader.

2. American Society for Engineering Education (ASEE) Annual Conference 2021

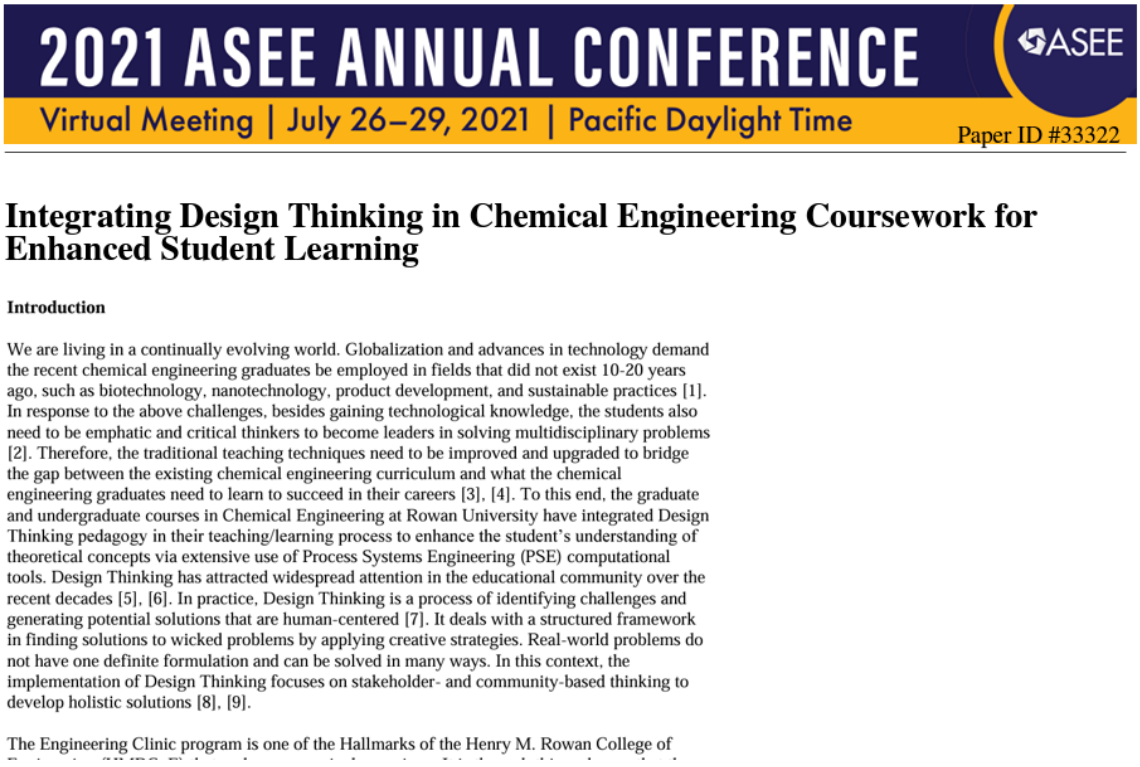

2021 ASEE ANNUAL CONFERENCE

Virtual Meeting | July 26–29, 2021 | Pacific Daylight Time

ASEE

Paper ID #33322

Integrating Design Thinking in Chemical Engineering Coursework for Enhanced Student Learning

Introduction

We are living in a continually evolving world. Globalization and advances in technology demand the recent chemical engineering graduates be employed in fields that did not exist 10-20 years ago, such as biotechnology, nanotechnology, product development, and sustainable practices [1]. In response to the above challenges, besides gaining technological knowledge, the students also need to be emphatic and critical thinkers to become leaders in solving multidisciplinary problems [2]. Therefore, the traditional teaching techniques need to be improved and upgraded to bridge the gap between the existing chemical engineering curriculum and what the chemical engineering graduates need to learn to succeed in their careers [3], [4]. To this end, the graduate and undergraduate courses in Chemical Engineering at Rowan University have integrated Design Thinking pedagogy in their teaching/learning process to enhance the student's understanding of theoretical concepts via extensive use of Process Systems Engineering (PSE) computational tools. Design Thinking has attracted widespread attention in the educational community over the recent decades [5], [6]. In practice, Design Thinking is a process of identifying challenges and generating potential solutions that are human-centered [7]. It deals with a structured framework in finding solutions to wicked problems by applying creative strategies. Real-world problems do not have one definite formulation and can be solved in many ways. In this context, the implementation of Design Thinking focuses on stakeholder- and community-based thinking to develop holistic solutions [8], [9].

The Engineering Clinic program is one of the Hallmarks of the Henry M. Rowan College of

This research was used as a tool for integrating Design Thinking in Chemical Engineering for Enhanced student learning. The work was published and presented in the 2021 ASEE annual conference proceedings.

Appendix D

Journal Publications

Clean Technologies and Environmental Policy (2020) 22:1187–1198
https://doi.org/10.1007/s10098-020-01861-8

ORIGINAL PAPER

Computer-aided synthesis of cost-effective perovskite crystals: an emerging alternative to silicon solar cells

Swapana S. Jerpoth[1] · Joseph Iannello[2] · Emmanuel A. Aboagye[1] · Kirti M. Yenkie[1]

Received: 23 March 2020 / Accepted: 9 May 2020 / Published online: 22 May 2020

Abstract

One of the ways that scientists and engineers have come up to harness solar power is by inventing photovoltaics. Perovskite, which is one of the most promising materials for solar cell fabrication, has gained much attention in recent years due to its exceptional increase in performance. However, the most challenging issue that has been prevalent is the stability of perovskite solar cells. Perovskite crystal has a general formula of ABX_3, where A and B are cations, and X is an anion. The Goldschmidt's tolerance factor and the octahedral tolerance factor are the stability criteria that have to be satisfied by a crystal, for it to be considered a perovskite. Also, there are different combinations of site-A cations, site-B cations, and site-X anions that can give rise to a perovskite crystal. There is, therefore, the need to synthesize perovskite crystals which satisfy these tolerance factors to guarantee stability at a minimum bearable cost. In this paper, we present an optimization problem, where we formulate an objective function to determine site-A cation, site-B cation, and site-X anion that minimize the cost of perovskite crystal synthesis subject to the octahedral and Goldschmidt's tolerance factors to assure stability. We further present three case studies based on this optimization approach. The results indicate that the optimal perovskite crystal structure is ammonium–magnesium–formate with a cost of 0.1784 ($/g), while the percentage variation in cost from the first-best combination to the second-best is 19.24%.

ACS OMEGA

Open Access

http://pubs.acs.org/journal/acsodf

Article

Strategic Optimization of the Flushing Operations in Lubricant Manufacturing and Packaging Facilities

Swapana S. Jerpoth, Robert Hesketh, C. Stewart Slater, Mariano J. Savelski, and Kirti M. Yenkie*

Cite This: *ACS Omega* 2023, 8, 38288−38300

Read Online

ACCESS | Metrics & More | Article Recommendations | Supporting Information

ABSTRACT: Commercial lubricant industries use a complex pipeline network for the sequential processing of thousands of unique products annually. Flushing is conducted between changeovers to ensure the integrity of each production batch. An upcoming product is used for cleaning the residues of the previous batch, resulting in the formation of a commingled/mixed oil that does not match the specifications of either of the two batches. The existing operations are based on the operator's experience and trial and error. After a selected flush time, the samples are tested for their viscosity to determine the success of a flush. The approach results in long downtime, the generation of large commingled oil volumes, and huge economic losses. Hence, to overcome the drawback, our work introduces a solution strategy for systematically optimizing flushing operations and making more informed decisions to improve the resource-management footprint of these industries. We use the American Petroleum Institute-Technical Data Book (API-TDB) blending correlations for calculating the mixture viscosities in real-time. The blending correlations are combined with our first-principles models and validated against well-designed experimental data from the partnered lubricant facility. Next, we formulate an optimal control problem for predicting the optimum flushing times. We solve the problem using two solution techniques viz. Pontryagin's maximum principle and discrete-time nonlinear programming. The results from both approaches are compared with well-designed experimental data, and the economic and environmental significance are discussed. The results illustrate that with the application of a discrete-time nonlinear programming solution approach, the flushing can be conducted at a customized flow rate, and the necessary flushing volume can be reduced to over 30% as compared to the trial-and-error mode of operation.

1. INTRODUCTION

In lubricant industries, a multiproduct pipeline system is used to process over a thousand unique products throughout the year. Different types and grades of products are manufactured and consecutively processed and packaged through sequential batch operations. The multiproduct pipelines pose many difficulties due to the high level of operational complexities.[1,2] flush the residues of the product from a previous batch. The flushing operation generates a commingled (mixed) oil that does not match the desired specifications of either of the two batches and is therefore classified as downgraded oil with a low economic value. The existing economic losses due to these drawbacks at a typical large-scale commercial facility exceed over $1M/year. Hence, this has been a long-standing and

Appendix E

Copyright Permissions

SPRINGER NATURE LICENSE
TERMS AND CONDITIONS

Sep 13, 2023

This Agreement between Rowan University -- Swapana Jerpoth ("You") and Springer Nature ("Springer Nature") consists of your license details and the terms and conditions provided by Springer Nature and Copyright Clearance Center.

License Number	5627281290692
License date	Sep 13, 2023
Licensed Content Publisher	Springer Nature
Licensed Content Publication	Clean Technologies and Environmental Policy
Licensed Content Title	Computer-aided synthesis of cost-effective perovskite crystals: an emerging alternative to silicon solar cells
Licensed Content Author	Swapana S. Jerpoth et al
Licensed Content Date	May 22, 2020
Type of Use	Thesis/Dissertation
Requestor type	academic/university or research institute
Format	print and electronic
Portion	full article/chapter
Will you be translating?	no